Early Science with the Murchison Widefield Array: From the Moon to the Nearest Radio Galaxies

Benjamin William McKinley

A thesis submitted for the degree of

Doctor of Philosophy

of the Australian National University

Research School of Astronomy & Astrophysics

Submitted 2nd May 2014

To my wife, Julia, for letting me do crazy stuff like this…

Disclaimer

I hereby declare that the work in this thesis is that of the candidate alone, except where indicated below or in the text of the thesis. The work was undertaken between February 2011 and April 2014 at the Australian National University (ANU), Canberra. It has not been submitted in whole or in part for any other degree at this or any other university.

This thesis has been submitted as a 'thesis by publication' in accordance with the relevant ANU policies. Each of the three main chapters is therefore a completely self-contained article, which has been published in, or submitted to, a peer-reviewed journal. The thesis has been excellent preparation for post-doctoral research, as the candidate has experienced the full scientific process from planning observations and reducing raw data, through to scientific analysis and producing peer-reviewed publications.

The three papers presented in this thesis use data from the Murchison Widefield Array (MWA) telescope and are therefore bound by the MWA publication policy[1]. The policy mandates the inclusion of a required list of authors on each paper, depending upon the data used, and as a result each paper has a large number of co-authors. Despite this long list of co-authors, the papers have been written predominantly by the candidate. For the articles on the Moon and Centaurus A, the candidate has written the entire papers, incorporating suggestions and feedback from the co-authors and the referees. For the Fornax A paper, approximately 10% of the work has been contributed by the first two co-authors. Specifically, Section 4.4.2 'Microwave-band data reduction' was contributed by Marcos López-Caniego and Section 4.4.3 '*Fermi*-LAT data reduction' was contributed by Ruizhi Yang. The spectral energy distribution fitting in Section 4.5.2 was also conducted by Ruizhi Yang, although the text describing the fitting and the subsequent discussion in Section 4.6 were written predominantly by the candidate.

Benjamin William McKinley

2nd May 2014

---

[1] http://www.mwatelescope.org/images/documents/2013.07.23_MWA_publication_policy_approved.pdf

Acknowledgments

Completing this PhD thesis would not have been possible without the help and support of a range of people, who I would like to acknowledge and sincerely thank for all they have done over the past three and a half years.

First and foremost I would like to thank my wife Julia for supporting me in undertaking this new adventure and for the many sacrifices that she made along the way. Neither of us knew quite what we were getting in to, but I know it was worth it. Also to my daughter Sofia, who put up with me doing so much 'boring computer work', and to my newborn daughter Bridget who came along right at the very end and had to put up with us all being a little stressed.

Many thanks go to my thesis supervisory board members; Frank Briggs, Randall Wayth and Brian Schmidt, who were always there for me, providing honest advice and support. Special thanks also to Denise Sturgess, who made all the administration run so smoothly, and through her friendly nature, made work feel like a second family.

I am greatly indebted to the whole MWA project team, including all the engineers, scientists and management team members. Many thanks go to the science commissioning team and in particular; André Offringa, Natasha Hurley-Walker and Gianni Bernardi who have helped me a great deal.

I would also like to particularly thank Steven Tingay and Bryan Gaensler for being excellent mentors to me throughout my PhD. Through them I have learned so much about what it means to be a world-class scientist.

As a CAASTRO student I have enjoyed many opportunities that have greatly enriched my experience as a PhD student, including the ability to travel and participate in meetings and conferences throughout the world. So I would like to sincerely thank all the CAASTRO staff that have made this possible.

Thanks also go to my non-MWA collaborators Ruizhi Yang and Marcos López-Caniego, who made major contributions to the work on Fornax A.

This scientific work makes use of the Murchison Radio-astronomy Observatory, operated by CSIRO. I acknowledge the Wajarri Yamatji people as the traditional owners of the Observatory site. Support for the MWA comes from the U.S. National Science Foundation (grants AST-0457585, PHY-0835713, CAREER-0847753, and AST-0908884), the Australian Research Council (LIEF grants LE0775621 and LE0882938), the U.S. Air Force Office of

Scientific Research (grant FA9550-0510247), and the Centre for All-sky Astrophysics (an Australian Research Council Centre of Excellence funded by grant CE110001020). Support is also provided by the Smithsonian Astrophysical Observatory, the MIT School of Science, the Raman Research Institute, the Australian National University, and the Victoria University of Wellington (via grant MED-E1799 from the New Zealand Ministry of Economic Development and an IBM Shared University Research Grant). The Australian Federal government provides additional support via the Commonwealth Scientific and Industrial Research Organisation (CSIRO), National Collaborative Research Infrastructure Strategy, Education Investment Fund, and the Australia India Strategic Research Fund, and Astronomy Australia Limited, under contract to Curtin University. I acknowledge the iVEC Petabyte Data Store, the Initiative in Innovative Computing and the CUDA Center for Excellence sponsored by NVIDIA at Harvard University, and the International Centre for Radio Astronomy Research (ICRAR), a Joint Venture of Curtin University and The University of Western Australia, funded by the Western Australian State government. I also acknowledge the support of the projects Spanish MINECO AYA2012-39475-C02-01 and CSD2010-00064.

Abstract

This thesis reports on new scientific results gleaned from test observations of well-known astronomical sources with the Murchison Widefield Array (MWA) telescope. Presented are three self-contained papers that demonstrate the capabilities of this recently commissioned radio interferometer array and provide new insights into the astrophysics of the Moon, Centaurus A and Fornax A at low frequencies.

One of the main scientific goals of the MWA is the detection of the redshifted 21-cm line of neutral hydrogen from the epoch of reionization (EoR). To investigate the possibility of using the Moon as a calibration source for EoR detection and to test novel observing modes for the MWA, the Moon was observed over a frequency range of 80 – 170 MHz with the MWA 32-tile prototype. The observations show that the Moon's radio emission is as expected for a cool thermally emitting body, but that the spectrum is corrupted by reflected transmissions from Earth. In particular, the observed flux density of the Moon abruptly increases in the internationally recognized frequency modulated (FM) radio band. The implications for EoR detection using the Moon as a spectrally smooth reference source are discussed and the flux density of the Moon in the FM radio band is used to estimate the Earth's radio leakage and its potential for detection by an extraterrestrial race.

Observations of our closest neighbouring radio galaxy, Centaurus A, were made at 118 MHz with the MWA 32-tile prototype. The resulting images demonstrated the widefield imaging capabilities of the MWA and provided the first evidence in total intensity for a southern counterpart to the well-known northern middle lobe of Centaurus A. A detailed spectral analysis of the radio lobes between 118 MHz and 1.4 GHz reveals significant spatial variation of the spectral index across the lobes, supporting a scenario of multiple outbursts of central activity being responsible for the large-scale morphology.

Another nearby radio galaxy, Fornax A, was observed with the complete 128-tile MWA at 154 MHz. The MWA data were used in combination with radio, microwave, X-ray and γ-ray data to model the spectral energy distribution of Fornax A and investigate, for the first time, the origin of the γ-ray emission. It was found that the multi-wavelength data are poorly fit by a purely leptonic, inverse-Compton scattering model and that hadronic processes may account for the γ-ray emission from Fornax A.

Contents

List of Figures ix

List of Tables xv

1 Introduction **1**

1.1 The Murchison Widefield Array 1

1.2 Observations and Science 3

2 Low-Frequency Observations of the Moon with the Murchison Widefield Array **5**

2.1 Abstract 5

2.2 Introduction 6

2.3 Observations 8

2.4 Calibration and Imaging 11

2.5 Analysis 18

2.6 Conclusions 23

3 The giant lobes of Centaurus A observed at 118 MHz with the Murchison Widefield Array **25**

3.1 Abstract 25

3.2 Introduction 26

3.3 Previous observations and analyses of the giant lobes 28

3.4 Observations and Data Reduction 29
3.5 Results and Analysis 33
3.6 Discussion 48
3.7 Conclusion 51

4 Modelling of the Spectral Energy Distribution of Fornax A: Leptonic and Hadronic Production of High Energy Emission from the Radio Lobes 53

4.1 Abstract 53
4.2 Introduction 54
4.3 Previous radio observations and analyses of For A 55
4.4 Multi-wavelength Data 57
4.5 Spectral Energy Distribution Analysis 66
4.6 Discussion 72
4.7 Conclusion 74

5 Conclusion 75

Bibliography 79

List of Figures

2.1 Theoretical difference between Moon and sky flux density at J2000 coordinates $0^{\mathrm{h}}51^{\mathrm{m}}6^{\mathrm{s}}$, 11°24′40″, for observations at 0030-0132 LST on UTC dates 2010 September 24 and 25, respectively. 8

2.2 Positions of MWA 32T tiles relative to the array center. 9

2.3 MWA 32T instantaneous UV coverage for a pointing at the Moon at azimuth 357°, elevation 52° and frequency 80 MHz (wavelength 3.75 m). 10

2.4 Moon field images on 10 MHz bandwidth, centered at 94 MHz, for 2010 September 24 (left panel) and 2010 September 25 (right panel). The flux scale is arbitrary at this stage of the calibration process and no primary beam correction has been applied. Darker gray scale indicates higher flux density. 13

2.5 Moon spectrum at 1.28 MHz resolution on 2010 September 24 with an arbitrary flux density scale. The vertical lines denote the FM radio band of 87.5 – 108 MHz. 13

2.6 Image slice from the Moon-sky difference cube centered at 99.835 MHz and covering 0.92 MHz of bandwidth (since 28% of the sub-band is flagged). The flux scale of the image is arbitrary at this stage of the calibration process. Darker gray scale indicates higher (positive) flux density. 15

2.7 Integrated flux density of the “Moon” pixels in the Moon−sky difference image on Day 1 when the Moon was at the center of the beam and Day 2 when the Moon had drifted to approximately the half-power point of the beam. The flux density scale has been set using 3C33 as a reference, but no primary beam correction has been applied to the Moon spectra. 17

2.8 Comparison between the observed Moon−sky flux density difference on September 24 and the difference predicted for a model of the Moon that includes thermal emission and reflection of galactic background only. The excess flux density in the observations is attributed to the reflection of the Earth’s radio leakage. 18

2.9 Disk average brightness temperature of the Moon calculated from MWA 32T measurements, combined with a model of the sky temperature derived from Rogers & Bowman (2008) and de Oliveira-Costa et al (2008). 19

2.10 Disk average brightness temperature of the Moon calculated from MWA 32T measurements, combined with a model of the sky temperature derived from Rogers & Bowman (2008) and de Oliveira-Costa et al (2008). This is the same as Figure 2.9 but plotted on a different scale and with error bars based on the rms noise of the MWA 32T difference image. The dotted line is the thermal brightness temperature of the Moon of 230K from Heiles & Drake (1963) plus the expected reflection of galactic emission. 20

2.11 Equivalent isotropic power (EIP) of radio emissions from Earth as measured from MWA 32T observations of the Moon. The plot is a histogram with 5 MHz bins. 21

3.1 Combined uv-coverage for all snapshots centred on 118 MHz with a bandwidth of 20 MHz, in units of wavelength. The plot does not include the three shortest baselines, which were excluded from calibration and imaging. . . . 31

3.2 Average tile primary beam from an analytic model. The centre frequency is 118 MHz. Contours are from 10 to 90 per cent of the peak gain (normalized to 1), incrementing in steps of 10 per cent. 32

3.3 Cen A and surrounding field at 118 MHz with the MWA 32-Tile prototype. The image is shown on a linear scale between −15 and +40 Jy/beam. It has an angular resolution of 25 arcmin and an rms noise of approximately 0.5 Jy/beam in ‘empty’ regions of the map. 35

3.4 Profile through the centre of the MWA 118 MHz image of Cen A (see Fig. 3.3) along a constant declination of (J2000) $-43°01'9''$, showing the negative bowl surrounding the core of Cen A in the image. 36

3.5 Comparison between the MWA 118 MHz image (left) and Haslam et al. (1982) 408 MHz image (right), both smoothed to the same angular resolution of $0\overset{\circ}{.}85$. A linear brightness gradient has been subtracted from the Haslam et al. (1982) map to make the smaller-scale structures clearer. The faint diffuse structure on scales less than 12° matches well by eye. Labels 1 to 3 indicate large-scale foreground features clearly present in both maps. 36

3.6 Cen A at 118 MHz (gray scale and red contours) overlaid with Parkes 1.4 GHz contours in blue, smoothed to the same angular resolution of 25 arcmin. Positive contours are bold and start at 2.5 Jy/beam for 118 MHz and 0.50 Jy/beam for 1.4 GHz, incrementing in a geometric progression of $\sqrt{2}$. Negative contours (thinner and lighter shade) start at -2.5 Jy/beam for 118 MHz and -0.50 Jy/beam for 1.4 GHz and decrement in a geometric progression of $\sqrt{2}$. 38

3.7 Regions from Hardcastle et al. (2009) used for constructing T-T plots, overlaid on the MWA 118 MHz image resampled to 1 pixel per beam. Contours are of the full resolution 118 MHz image, incrementing in a geometric progression of $\sqrt{2}$ from 2.5 Jy/beam. 40

3.8 T-T plots for the five regions of the giant lobes of Cen A and the computed spectral indices between 118 and 1400 MHz, including the χ^2_{red} values for each region as defined in Fig. 3.7. The centre row contains two plots for region 3; on the left all pixels have been included, and on the right the bright central pixel has been excluded to remove the influence of the inner lobes. The uncertainties in the spectral indices displayed are derived from the uncertainty in the slope of the line of best fit and represent random errors only. See text for the inclusion of systematic errors due to global flux scale uncertainties. 41

3.9 A subset of the spectral tomography images of the northern lobe between 118 MHz and 1.4 GHz with trial spectral indices as indicated in the top-left corner of each sub-image. Gray scale is from -10 to 10 Jy/beam. Overlaid are contours from the 118 MHz image at 2.5, 5, 10, 20, 28.3 and 113 Jy/beam. The feature labelled A has a significantly flatter spectral index than that labelled B. Similarly, there is a change in spectral index between the flatter region labelled D and the steeper feature labelled C. 45

3.10 As for Fig. 3.9, but for the southern lobe with contours from the 118 MHz image at 2.5, 5, 10, 20, 28.3 and 56.5 Jy/beam. The feature labelled E has a significantly steeper spectral index than that labelled F. 46

3.11 High resolution 1.4 GHz Parkes+ATCA map (Feain et al. 2011) in gray scale, overlaid with the 1.4 GHz Parkes contours (O'Sullivan et al. 2013) in blue and the MWA 118 MHz contours in red. Positive 118 MHz MWA contours are from 3 Jy/beam incrementing in steps of 5 Jy/beam and 1.4 GHz Parkes contours are from 1 Jy/beam incrementing in steps of 1 Jy/beam. There is one negative contour visible, which is the −3 Jy/beam level of the 118 MHz map, shown as a thinner, lighter red line. There is a peak at 13^h23^m, $-43°51'$ in the 118 MHz map that is not visible in the 1.4 GHz images and does not coincide with any background sources visible at 1.4 GHz. The bright background source MRC 1318-434B, at $13^h21^m18^s$, $-43°41'15''$, extends approximately 20 arcmin and is coincidentally aligned with the position angle of the inner lobes of Cen A. 47

4.1 Fornax A and surrounding field at 154 MHz with the Murchison Widefield Array. The image is shown on a linear scale between −0.05 and +2 Jy/beam. It has an angular resolution of 185 arcsec and an rms noise of approximately 15 mJy/beam in 'empty' regions of the image more than 1° away from Fornax A. The red circles mark the positions of the Culgoora sources (Slee 1977, 1995) used to set the flux-density scale. 59

4.2 As for Fig. 4.1, but zoomed in on Fornax A. The image is shown on a linear scale between −1 and +15 Jy/beam. 60

4.3 γ-ray counts image (left panel) and residual image (right panel) above 100 MeV in the ROI. The sources in the 2FGL catalogue are marked as red circles. . . 62

4.4 The SED of Fornax A above 100 MeV derived from *Fermi*-LAT observations. 63

4.5 Fornax A at 154 MHz (gray scale and red contours) overlaid with the VLA 1.5 GHz (Fomalont et al. 1989) contours, after smoothing to the MWA resolution, in blue. Positive contours are solid and increment in a geometric progression of $\sqrt{2}$, starting at 0.1 Jy/beam for the 154 MHz image and 0.05 Jy/beam for the 1.5 GHz image. The broken red contour is at -0.1 Jy/beam and the broken blue contour is at -0.05 Jy/beam. 67

4.6 Slices from the spectral tomography cube, with trial spectral indices indicated in the top left corner of each panel panel. The white arrow shows the position of the compact core which has a steeper spectrum than the lobes. The gray scale is linear and from -1.5 to 1.5 Jy/beam. 68

4.7 T-T plots for east (left panel) and west (right panel) lobes of Fornax A. 69

4.8 The broadband SED of Fornax A for Model I, where both the X-rays and γ-rays are produced by IC scattering by the synchrotron-emitting electrons. The IC scattering contribution from the EBL and the CMB photon fields are both shown in the figure. The model parameters are described in Table 4.2. 71

4.9 The broadband SED of Fornax A for Model II, where both the X-rays and γ-rays are produced by IC scattering by the synchrotron-emitting electrons, which are described by an electron energy distribution with a low-energy cut-off. The model parameters are described in Table 4.2. 71

4.10 The broadband SED of Fornax A for Model III, where the X-ray emission is the result of IC scattering by the synchrotron-emitting electrons and the γ-rays are produce by p-p collisions with pion decay. The model parameters are described in Table 4.2. 72

5.1 A mosaic of 60 snapshot images at 150 MHz, taken over the course of one night with the MWA during science commissioning. The telescope was operated in drift-scan mode, with a fixed pointing at -55 declination along the meridian. The bright object at the top of the image is Centaurus A and the thick band of emission running through the centre of the image is the Galactic plane. 77

List of Tables

3.1 Sources Used to Set Flux Density Scale 33

4.1 Fornax A SED Data. 64
4.2 Summary of Fornax A SED best-fit model parameters 72

CHAPTER 1

Introduction

> We have a habit in writing articles published in scientific journals to make the work as finished as possible, to cover up all the tracks, to not worry about the blind alleys or describe how you had the wrong idea first, and so on. So there isn't any place to publish, in a dignified manner, what you actually did in order to get to do the work.
>
> – Richard Phillips Feynman (1918-1988)[1]

1.1. The Murchison Widefield Array

We are at the beginning of an exciting new era in astronomy, when the next generation of radio telescopes will open up a new parameter space, allowing us to probe deeper into the early universe than ever before. Technological advances, particularly in the areas of computing and digital signal processing, have made possible innovative new ways of doing radio interferometry, particularly at low frequencies. Several new instruments currently in development and operation are based on the principle of combining the signals from a very large number of inexpensive dipole antennas. These new instruments include the Low Frequency Array (LOFAR; van Haarlem et al. 2013), the Precision Array for Probing the Epoch of Reionization (PAPER; Parsons et al. 2010) and the Murchison Widefield Array (MWA; Tingay et al. 2013; Lonsdale et al 2009). This PhD thesis is focussed on observations with the MWA, which operates at frequencies between 80 and 300 MHz and is located at the Murchison Radio Observatory (MRO) in outback Western Australia; the site selected for the low-frequency component of the Square Kilometre Array (SKA; Dewdney et al. 2009).

---

[1] *Nobel Lecture, 1965 December 11*

The MWA has four main science drivers (Bowman et al. 2013):

1. Detection of the redshifted HI signal from the epoch of reionization (EoR).
2. Galactic and extragalactic surveys.
3. Time-domain astrophysics (searching for transient and variable radio sources).
4. Solar, heliospheric and ionospheric science.

The MWA design is based on a large number of inexpensive, crossed-dipole antennas, grouped into 'tiles' that are steered electronically without the need for moving parts. The signals from these antenna tiles are combined and processed to produce widefield radio images. A prototype instrument consisting of 32 antenna tiles (MWA 32T) was constructed and operated over the period September 2007 to September 2011 in order to verify concepts and conduct engineering tests for development of the final instrument. During a number of site visits, science data were also obtained for a number of radio sources, using various modes of operation.

Construction of the final 128-tile MWA began in 2012 February and science commissioning of the instrument began with the completion of the first 32 tiles. I was appointed to the MWA science commissioning team in 2012 and over a twelve-month period from 2012 June to 2013 June, I worked with the rest of the science commissioning team and the engineering team to verify that each subsystem of the instrument was working as required and that the instrument could produce science-quality data. My tasks during science commissioning included examining the raw data soon after it was collected during each two-week site trip and calibrating and imaging data from observed bright sources to test system performance. Science commissioning was successfully completed in 2013 July at which point the MWA made the transition to scientific operations. The skills I obtained through this science commissioning work have enabled me to conduct the low-frequency science of this PhD thesis.

The approach taken to completing this PhD thesis was in line with the philosophy of the MWA science commissioning process and had two main goals:

1. To contribute to our understanding of the MWA instrument by calibrating, imaging and analysing MWA data to conduct new scientific research, and providing feedback to the rest of the project team on any lessons learned during this process.
2. To contribute to our understanding of the astrophysics of nearby radio galaxies, through analysis of their morphological and spectral properties at low frequencies.

The three papers presented in this PhD thesis are the culmination of my 3.5 year journey with the MWA from its early prototype stage through to full scientific operations. Many challenges in calibration, imaging and data analysis have been overcome to produce this science, which paves the way for future work with this exciting new instrument.

1.2. Observations and Science

When this PhD was commenced in 2011 February, the MWA was in a highly developmental phase and there were no standard techniques or procedures laid out for dealing with MWA data. In this developmental stage, observations of well-known radio sources were observed in order to verify system performance and conduct engineering tests. One such set of test observations was a series of scans of the Moon, taken in a novel 'picket fence' mode of operation, where the 30 MHz of bandwidth available was split up into chunks and spread evenly between 80 and 200 MHz. Processing this data was my first experience with MWA data reduction and analysis, and laid the foundation for my future work. The results of the observations proved to be interesting and resulted in the publication: 'Low-frequency observations of the Moon with the Murchison Widefield Array' (McKinley et al. 2013a), which is contained in Chapter 2 of this thesis.

Centaurus A is our nearest neighbouring radio galaxy and has the largest angular size ($4^\circ \times 8^\circ$) of any radio galaxy in the sky. This made it an ideal target to test the widefield imaging capabilities of the MWA, and a set of observations were taken during a MWA 32T site trip in 2011 April. Centaurus A is also one of the brightest radio sources in the southern sky and has been studied extensively across a wide range of frequencies. Its large angular size and very bright compact core, however, have hampered efforts to image the entire source at reasonable angular resolution. The MWA observations allowed us to study the morphology of the source at low radio frequencies and to study the spatial variation of the spectral index of the radio lobes by comparing the MWA data to 1.4 GHz data from Feain et al. (2011). This work resulted in the publication: 'The giant lobes of Centaurus A observed at 118 MHz with the Murchison Widefield Array' (McKinley et al. 2013b), which is contained in Chapter 3 of this thesis.

Another well-known, bright nearby radio galaxy in the southern sky is Fornax A. This radio galaxy is of particular interest to the MWA community as it is located in one of the sky regions being observed for the detection of the EoR. Hence, this source was one of the first to be observed with the full 128-tile MWA. The scientific motivation behind my work on Fornax A, however, extends beyond the realm of the MWA. It has been shown that the lobes of Fornax A emit X-rays due to the inverse Compton scattering of CMB photons by the relativistic electrons that produce the observed synchrotron emission in the lobes (Feigelson et al. 1995). Modelling this process and fitting the radio and X-ray data allows researchers to determine the physical properties of the lobes without the need for relying on assumptions such as energy equipartition. Several studies have already done this for Fornax A, however they relied on assumptions about the low-frequency properties of the lobes. Also, new data in the form of γ-ray observations from *Fermi*-LAT and microwave data from *Planck* have become available, allowing better constraints on the spectral energy distribution. The paper 'A multi-wavelength analysis of Fornax A' combines MWA data, for the first time, with multi-wavelength data across a wide range of energies, to investigate the high-energy processes in the Fornax A lobes. This paper is contained in Chapter 4 of this thesis.

CHAPTER 2

Low-Frequency Observations of the Moon with the Murchison Widefield Array

This chapter has been previously published as 'Low-frequency observations of the Moon with the Murchison Widefield Array', McKinley, B., Briggs, F., Kaplan, D. L., et al., 2013, AJ, 145, 23.

2.1. Abstract

A new generation of low-frequency radio telescopes is seeking to observe the redshifted 21 cm signal from the epoch of reionization, requiring innovative methods of calibration and imaging to overcome the difficulties of widefield low frequency radio interferometry. Precise calibration will be required to separate the small expected EoR signal from the strong foreground emission at the frequencies of interest between 80 and 300 MHz. The Moon may be useful as a calibration source for detection of the EoR signature, as it should have a smooth and predictable thermal spectrum across the frequency band of interest. Initial observations of the Moon with the Murchison Widefield Array 32 tile prototype show that the Moon does exhibit a similar trend to that expected for a cool thermally emitting body in the observed frequency range, but that the spectrum is corrupted by reflected radio emission from Earth. In particular, there is an abrupt increase in the observed flux density of the Moon within the internationally recognized frequency modulated (FM) radio band. The observations have implications for future low frequency surveys and EoR detection

experiments that will need to take this reflected emission from the Moon into account. The results also allow us to estimate the equivalent isotropic power emitted by the Earth in the FM band and to determine how bright the Earth might appear at meter wavelengths to an observer beyond our own solar system.

2.2. Introduction

The astrophysics of the intergalactic medium over the redshift interval $z \approx 200-8$ is expected to give rise to observable phenomena in the redshifted 21 cm line of neutral hydrogen (see e.g. Pritchard & Loeb 2011; Morales & Wyithe 2010; Furlanetto et al 2006 for detailed reviews). The 21 cm line from this period, which extends from the dark ages through the epoch of reionization (EoR), redshifts to radio frequencies of between 30 and 200 MHz, making it a suitable target for the next generation of low frequency radio telescopes. Use of the redshifted 21cm line of neutral hydrogen to study the EoR will require exquisite calibration in order to achieve milli-Kelvin level spectral line sensitivity in the presence of Galactic and extragalactic foregrounds that are brighter than the expected signal by at least 2 – 3 orders of magnitude (Shaver et al 1999; Rogers & Bowman 2008; Bernardi et al 2009). One suggestion (Shaver et al 1999) for instrumental calibration for observation of the global EoR signature (Bowman & Rogers 2010) would be to use the smooth, thermal spectrum of the Moon for comparison with the sky brightness.

The goals of the work reported here are to assess the suitability of the Moon as a comparison source for EoR detection and to test novel observing modes for the Murchison Widefield Array (MWA; Tingay et al. 2013; Lonsdale et al 2009) that would span the full range of the uncertainty in redshift that surrounds the reionization phase change.

A concern at the outset has been that the lunar spectrum could be corrupted by reflected communications and navigation transmissions from the Earth. It has been known since the US Army Signal Corps' Project Diana (DeWitt & Stodola 1949) that radio signals could be reflected by the Moon and received on Earth. Indeed, it is now common practice for amateur radio enthusiasts to bounce communications signals off the Moon (Katz & Franco 2011) to be received by listeners on the other side of the planet. Radio leakage from the Earth has been modeled theoretically (Sullivan et al 1978) and measured by observing the reflected signals off the Moon using the Arecibo telescope (Sullivan & Knowles 1985). However, the use of radio communications on Earth has changed since these studies were undertaken and the EoR waveband of 80 – 200 MHz covered by the MWA deserves an updated study and continued monitoring. A strength of the present observations with the MWA 32 tile prototype (MWA 32T) is that the gain of the synthesized beam isolates the lunar reflections from any ambient signals that may enter weakly into the radio quiet zone of the Murchison Radio Observatory (MRO) on more direct paths from local transmitters.

At the frequencies of interest the radio sky is bright and dominated by synchrotron radiation from the Milky Way. The sky background varies as a power law function of frequency (Rogers & Bowman 2008; de Oliveira-Costa et al 2008) and the sky brightness temperature is given by

$$T_{\mathrm{sky}} = T_{150}\left(\frac{\nu}{150\ \mathrm{MHz}}\right)^{-\beta}\ \mathrm{K}, \tag{2.1}$$

where the spectral index β at high galactic latitudes has been measured (Rogers & Bowman 2008) to be 2.5 and at the sky position of these observations (J2000 coordinates $0^{\mathrm{h}}51^{\mathrm{m}}6^{\mathrm{s}}$, $11°24'40''$) the sky temperature T_{150} is 248 K (Landecker & Wielebinski 1970).

The brightness temperature of the Moon can be modeled by a combination of three factors: thermal emission, assuming a Moon brightness temperature of 230 K (Heiles & Drake 1963); reflected radio sky background emission, assuming a Moon reflectivity of 7% (Evans 1969) and sky temperature given by Equation (2.1); and reflected emission from the Earth. Reflected emission from the Sun, even at Full Moon, is expected to contribute less than 1K for a quiet Sun (Hagfors et al 1969). This reflected solar emission is not included since, based on the information available from the National Oceanic and Atmospheric Administration Space Weather Prediction Center (NOAA SWPC), the solar activity during our observing period was low. The thermal radio emission from the Moon, at the frequencies of interest in this paper, originates predominantly in the layers of regolith well below the surface, hence variations in reflectivity and scattering angle at the surface have no appreciable effect on the radio emission and there is no detectable variability of the lunar brightness temperature with lunar phase at these frequencies (Baldwin 1961). The contribution to the brightness temperature from reflected emission from the Earth is left as an unknown parameter in this model as it is not well understood at these frequencies and for recent times. These observations aim to contribute to the characterization of this reflected emission.

Brightness temperatures (T_b in K) are converted to flux densities (S in Jy) by

$$S = \frac{2kT_b\Omega}{\lambda^2 10^{-26}}, \tag{2.2}$$

where k is the Boltzmann constant in J K^{-1}, Ω is the solid angle subtended on the sky in steradians and λ is wavelength in m. The value of Ω used is 6.0×10^{-5} which corresponds to the Moon's angular diameter of 30.0 arcmin at the time of these observations. The expected

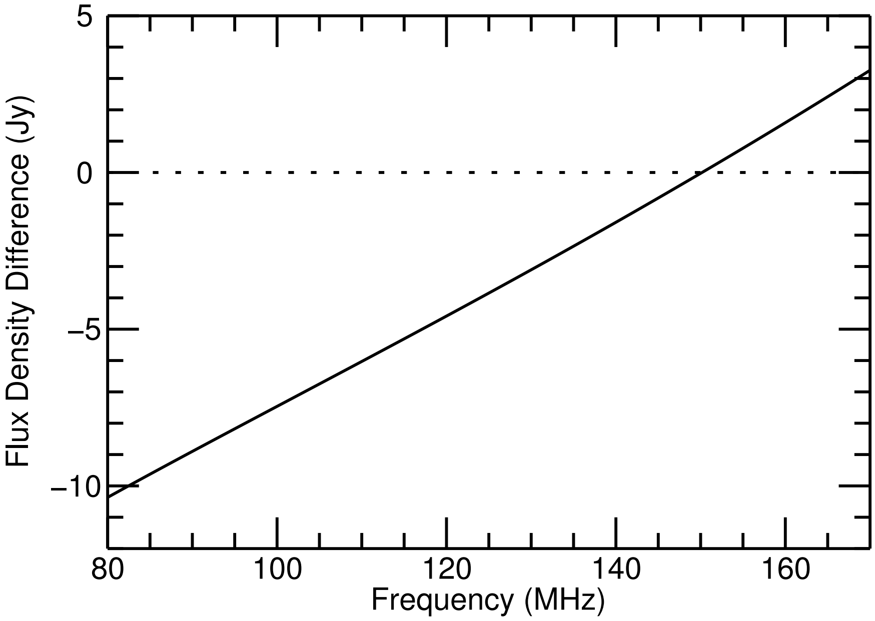

Figure 2.1 Theoretical difference between Moon and sky flux density at J2000 coordinates $0^h51^m6^s$, 11°24′40″, for observations at 0030-0132 LST on UTC dates 2010 September 24 and 25, respectively.

difference in flux density between the Moon and the sky, ignoring reflected emission from Earth, is plotted in Figure 2.1 and shows that at the lower end of the frequency band the Moon should appear as a 'hole in the sky', crossing over to being a positive source relative to the sky background at around 150 MHz. Recovering this Moon-sky difference signal was an important aim of the MWA observations described in this paper.

2.3. Observations

The MWA is a new type of radio interferometer array that is designed to observe the redshifted 21 cm signal at frequencies of between 80 and 300 MHz, corresponding to a redshift range of $z = 4 - 17$ (Tingay et al. 2013; Lonsdale et al 2009). It consists of a large number of small, crossed-dipole antennas grouped into "tiles" whose beams are electronically steered using analog beamformers. Each tile is made up of 16 dipole antennas arranged in a 4 by 4 grid above a conducting mesh ground plane. A 32 tile prototype instrument (MWA 32T) was operated over the period 2007 September to 2011 September within the radio-quiet MRO located in outback Western Australia. More detailed descriptions of the MWA 32T prototype configuration can be found in Oberoi et al (2011), Ord et al (2010) and Williams et al (2012).

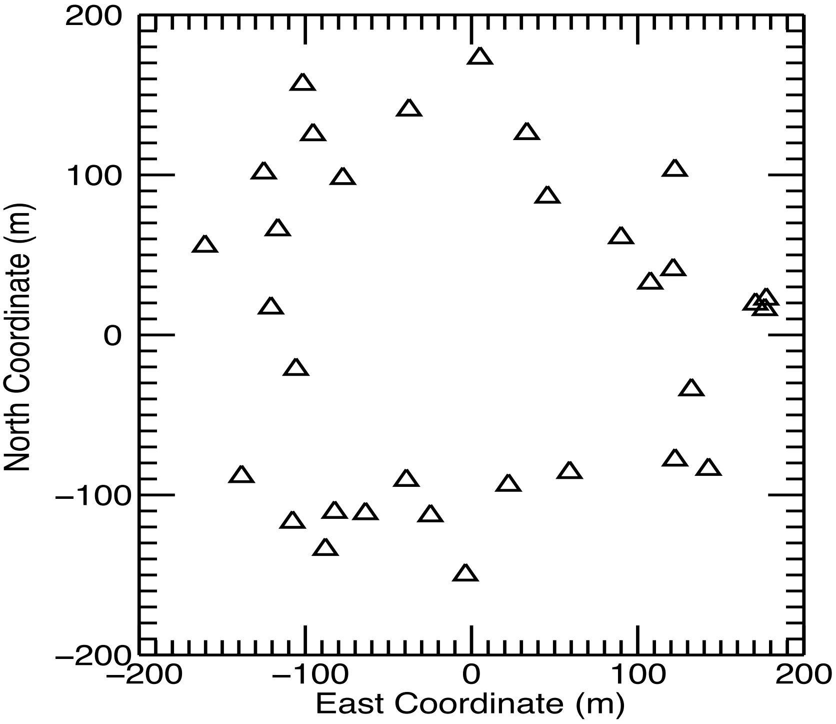

Figure 2.2 Positions of MWA 32T tiles relative to the array center.

The observations were conducted with the MWA 32T during Expedition 14 to the MWA site, which took place in 2010 September. The 32 tiles of the prototype system were arranged as shown in Figure 2.2. The positions are relative to the array center. This tile configuration gives an instantaneous UV coverage as shown in Figure 2.3 for a pointing at the Moon at azimuth 357°, elevation 52°, and frequency 80 MHz. Multi-frequency and Earth-rotation synthesis were used to maximize UV coverage for imaging. With this tile configuration the maximum baseline is approximately 350 m, giving a spatial resolution of approximately 30 arcmin at 100 MHz.

The Moon observations were made in a novel "picket fence mode" which reallocated the 30.72 MHz of signal processing capacity to sample the frequency range from 80 to 200 MHz with 24 evenly spaced 1.28 MHz wide sub-bands. Four different sub-band configurations were used to fill the whole spectrum across this frequency range. The 24 sub-bands of the MWA 32T are further divided into 32 fine channels, giving a spectral resolution of 40 kHz.

Observations of the Moon were made over the identical range of 0030 – 0132 LST on UTC dates 2010 September 24 and 25 (approximately 1630 – 1732 UTC). The resulting data set consisted of 32, 107 s integrations (eight scans for each channel configuration) on both days. The telescope was configured such that the beam center was aimed at the computed position of the Moon at 0100 LST on September 24 (J2000 coordinates $0^h51^m6^s$, 11°24′40″) and the

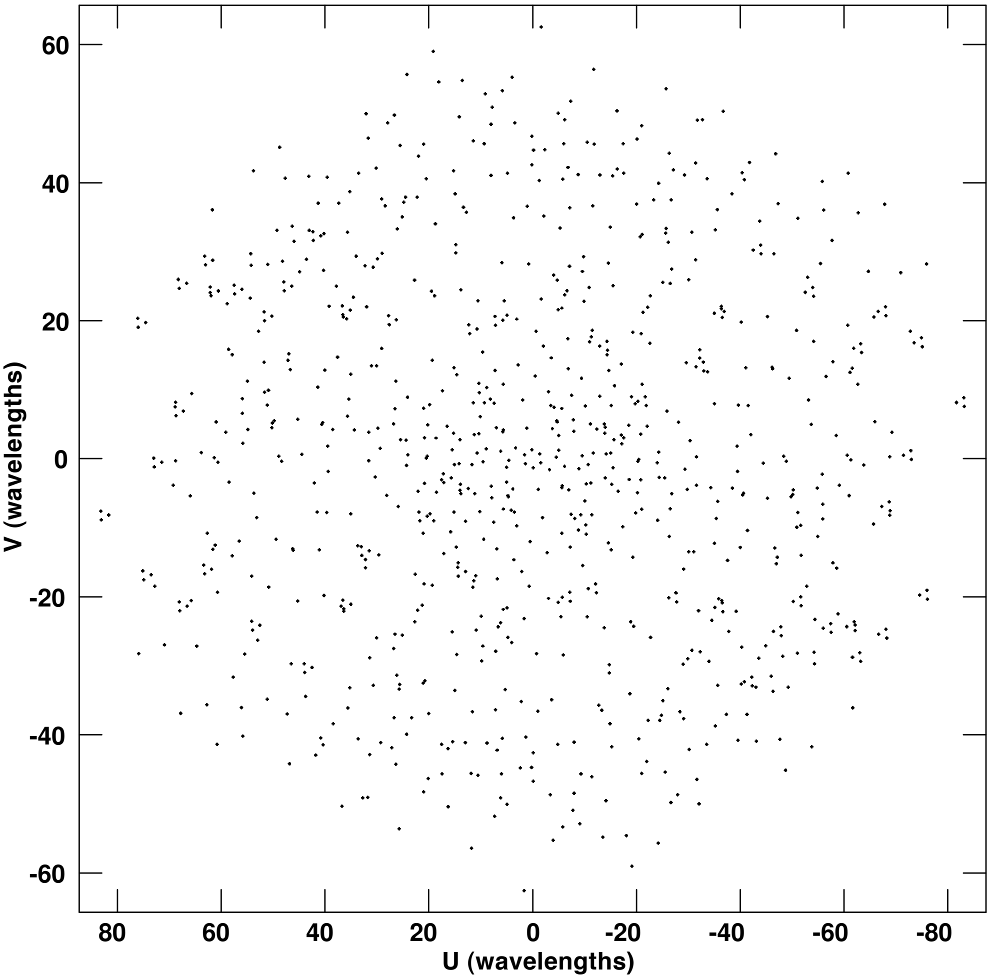

Figure 2.3 MWA 32T instantaneous UV coverage for a pointing at the Moon at azimuth 357°, elevation 52° and frequency 80 MHz (wavelength 3.75 m).

field allowed to drift across this fixed beam position on both days. Identical beamformer delay settings were used on both days. This was done to maximize the stability of the system as re-pointing the beam has complicated gain effects that are yet to be fully characterized.

A calibration data set, using a setup identical to the Moon scans, but with the fixed telescope pointing centered on Fornax A, was also taken in the hour following the Moon scans on each day. These data were used for obtaining initial phase calibration solutions in order to start the self-calibration process. Fornax A could not be used to set the overall flux density scale as it has been found (Ord et al 2010) that while phase solutions transfer well between tile pointings, the amplitudes of the complex tile gains cannot be applied to different tile pointings without being in error by several percent. Fortunately, the relatively bright source 3C33 lies in the main beam close to the Moon's position and this source was used to tie the

Moon measurements to an established flux density scale.

2.4. Calibration and Imaging

The raw correlator data were averaged in time by 6 s and converted to UVFITS format. The data set was then imported to the Astronomical Image Processing System (AIPS) for data reduction. The UV data were examined at the finest spectral resolution and bad channels flagged manually. Radio-frequency interference (RFI) was sparse and generally limited to a few discrete narrow bands. Four fine channels at the edge of each sub-band, as well as the central fine channel were also flagged as these were known to be corrupted by aliasing and rounding error, respectively. Tiles 2 and 6 were also flagged during the observations as they were not behaving as expected. In order to reduce the subsequent processing time, the UV data were then averaged in frequency to give 0.64 MHz sub-bands. The complete data set, including both days, was concatenated into one AIPS file to allow self-calibration of the data set using the same sky model for both days. This approach tied the tile gain solutions for both days to a common reference, which was important for the Moon−sky differencing experiment.

A subset of the Fornax A data were used as an input to the AIPS 'CALIB' task to get an initial set of complex tile gain solutions for calibration. A calibration was performed on these data, assuming a sky model of a point source located at the center. The UV range in the initial calibration was selected to exclude longer baselines so that Fornax A would not be resolved. An image was then made using the AIPS task 'IMAGR', implementing Clark's variation of the Högbom CLEAN algorithm (Clark 1980; Schwab 1984). Faceting was used to account for wide-field effects. The clean component list generated by this imaging process was then fed back into the calibration procedure as an improved sky model. This self-calibration process was repeated for several iterations using the full UV range and phase solutions only, until convergence was achieved. A final phase and amplitude self-calibration iteration was performed and the resulting image of Fornax A clearly showed a bright double source, with many fainter radio sources in the field of view.

The tile gain solutions from the final self-calibration iteration of Fornax A were then applied to the Moon data as a starting point for self-calibration. The same procedure as described above for Fornax A was used to generate an image cube using the combined set of Moon data from September 24 and 25. Imaging was performed in 10 MHz bands to maintain a high signal−to−noise ratio, resulting in an image cube with nine frequency slices, centered on the Moon's position at 0100 LST on September 24. After the final calibration iteration was complete, the tile gain solutions were applied and the data for both days were imaged separately, producing an image cube for each day. Using the same sky model to self-calibrate the data for both days at the beginning of the process effectively tied the tile gain solutions to a common reference, allowing a fair comparison of the two days when imaged separately at the end. The motion of the Moon during the hour of observations on each day is 19 arcmin, which is approximately the size of the synthesized beam at 150 MHz (taking the diameter of the synthesized beam as $\lambda/350$ m). So at the higher end of the observed spectrum we would expect some smearing of the Moon image due to this motion.

Examination of the cubes revealed that the Moon is present as a bright source in two of the image slices, corresponding to 94 MHz and 104 MHz, on both days. On September 24 (Figure 2.4, left panel), the bright source appears at the center of the field and on the September 25 (Figure 2.4, right panel), the bright source has moved approximately 13° across the sky as expected of the Moon. The result shown in Figure 2.4 where the Moon appears to be a bright radio source rather than a cool "hole in the sky" does not agree with the simple prediction from Figure 2.1, which neglects reflected emission from the Earth.

To investigate this spectral behavior in more detail, a higher spectral resolution image cube was generated for the entire 50° diameter field using 1.28 MHz channels. We refer to this data cube as the Intermediate Calibration Cube, since the relative flux densities for the sources at each frequency are well determined but the overall gain passband and flux density scale have not yet been imposed. The spectrum of the integrated flux density of the central "Moon" pixels in the Intermediate Calibration Cube was plotted and is shown in Figure 2.5. It is clear that the Moon's brightest disk averaged emission corresponds exactly with the internationally recognized frequency modulated (FM) radio transmission band (ACMA 2009) of 87.5 – 108 MHz.

The imaging described up until this point has used self-calibration with an arbitrary flux density scale. Setting the flux density scale for the MWA 32T is difficult due to the currently uncharacterized behavior of the overall gain of the system for different beamformer settings. This means that the traditional method of pointing at a known flux calibrator and then pointing at the target source cannot be used reliably and a known source within the field of view of the target is required. The relatively bright source 3C33, located approximately $4\overset{\circ}{.}7$ from the pointing center, was therefore used as a calibration reference to establish a flux density scale for the Moon. 3C33 exhibits a power-law spectrum with measured flux densities of 105.3 ± 0.4 Jy at 74 MHz (Kassim et al 2007) and 58.3 ± 2.9 Jy at 178 MHz (Kühr

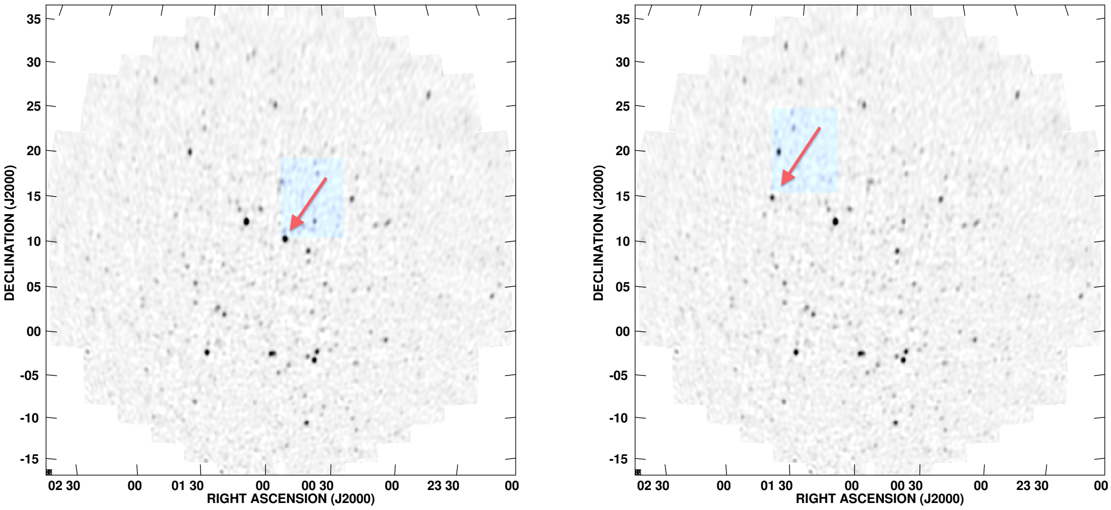

Figure 2.4 Moon field images on 10 MHz bandwidth, centered at 94 MHz, for 2010 September 24 (left panel) and 2010 September 25 (right panel). The flux scale is arbitrary at this stage of the calibration process and no primary beam correction has been applied. Darker gray scale indicates higher flux density.

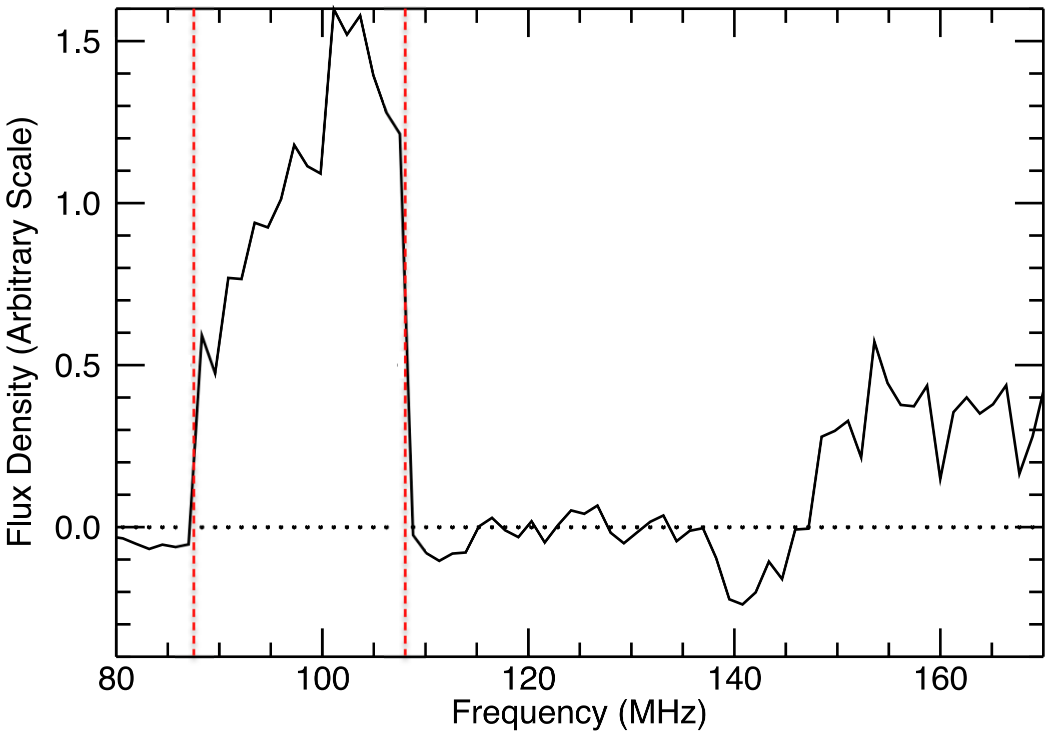

Figure 2.5 Moon spectrum at 1.28 MHz resolution on 2010 September 24 with an arbitrary flux density scale. The vertical lines denote the FM radio band of 87.5 – 108 MHz.

et al 1981). Interpolating these data using a power law with a single spectral index gives the following equation for the flux density of 3C33:

$$S_{\mathrm{calc}}(\nu) = S_{74}\left(\frac{\nu}{74\,\mathrm{MHz}}\right)^{-\alpha}\ \mathrm{Jy}, \tag{2.3}$$

where ν is the frequency in MHz, $S_{74} = 105.3 \pm 0.4$ and $\alpha = 0.67 \pm 0.06$.

The spectrum of 3C33 extracted from the Intermediate Calibration Cube was measured using the AIPS task "ISPEC". A correction was made to this measurement to account for the drop in gain of the primary beam as a function of frequency for the source which is approximately $4\overset{\circ}{.}7$ from the beam center. This rudimentary primary beam correction was based on a simple analytical model that did not take into account the different beam shape of the two dipole polarizations, but is accurate for positions close the pointing center. We refer to this corrected flux density of 3C33 as $S_{\mathrm{ICC}}(\nu)$.

Figure 2.5 does not show the smooth spectral shape expected for a thermal spectrum. Even outside the FM band there is considerable structure above the nominal noise level. The flux density calibration specified by Equation (2.3) is smooth on these scales and cannot cause this sort of structure.

Since the observations were made on two days with identical tracks as a function of sidereal time, certain classes of systematic imaging artifacts are expected to cancel when the *difference* between the two days data is examined. Specifically, the chromatic effects of residuals left from bright sources and integrated source confusion, observed with the incomplete UV coverage attained with the MWA 32T, can couple to spectral structure that will vary from beam to beam throughout the image cube. As a test of the presence of artefacts, an identical imaging and calibration process was used to produce an ICC for the September 25 data, and then a difference image cube was constructed by subtracting the September 25 cube from the September 24 cube. Figure 2.6 shows an image slice from the difference cube centered at 99.835 MHz.

For a perfect instrument and perfect calibration on both days of observation with identical conditions you would expect the rms noise in the difference image (Figure 2.6) to approach the thermal noise level, since all sources (including low level confused sources within the synthesized beam) would be perfectly subtracted.

The expected noise level in the Moon images, σ in Jy, is given by

$$\sigma = 10^{26}\left(\frac{2k_{\mathrm{B}}T}{A_{\mathrm{eff}}\epsilon_{\mathrm{c}}}\right)\sqrt{\frac{1}{N(N-1)Bn_{\mathrm{p}}\tau}}, \tag{2.4}$$

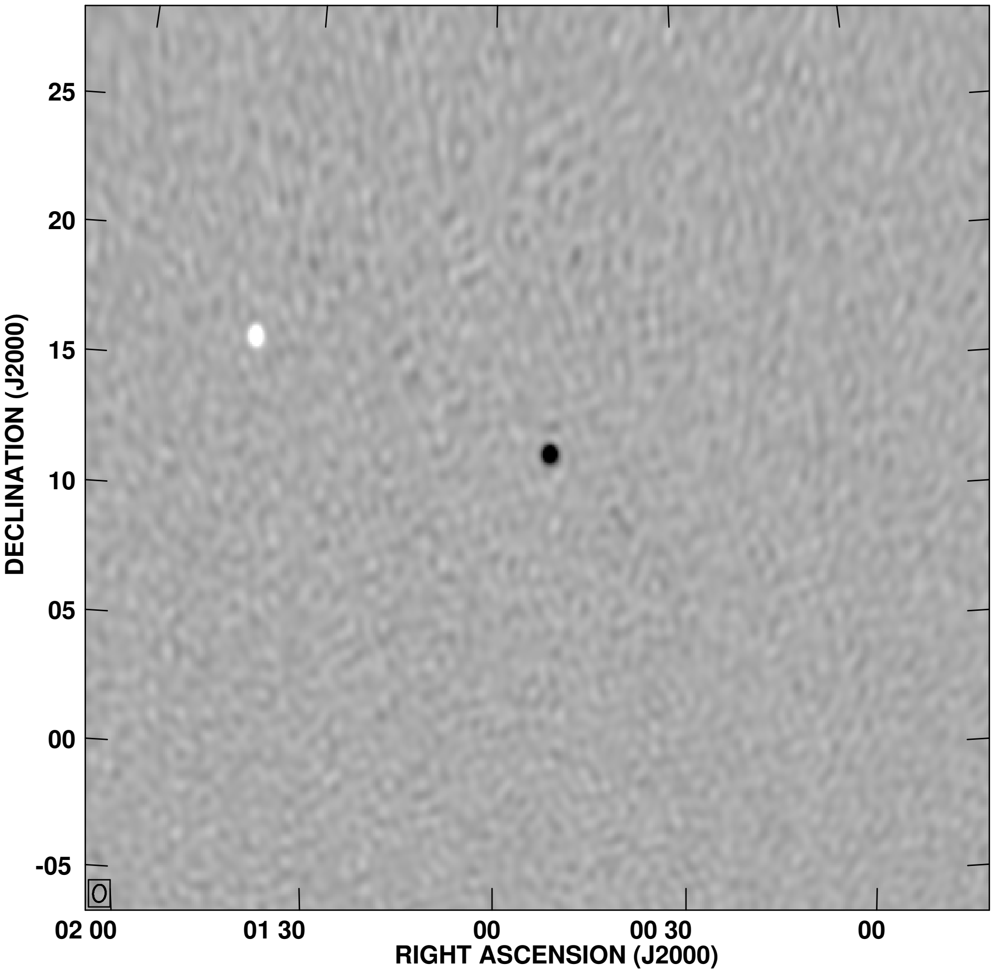

Figure 2.6 Image slice from the Moon-sky difference cube centered at 99.835 MHz and covering 0.92 MHz of bandwidth (since 28% of the sub-band is flagged). The flux scale of the image is arbitrary at this stage of the calibration process. Darker gray scale indicates higher (positive) flux density.

(adapted from Thompson et al 2001, Equation (6.62)), where k_B is the Boltzmann constant in J K^{-1}, $T = T_\mathrm{sky} + T_\mathrm{rcv} \approx 700$ K at 100 MHz, A_eff is the effective collecting area of a tile $\approx 21.5\ \mathrm{m}^2$ (Tingay et al. 2013), N is the number of tiles (N= 30 for these observations), ϵ_c is the correlator efficiency (assumed unity), B is the instantaneous bandwidth in Hz, n_p is the number of polarizations and τ is the integration time in s. Equation (2.4) assumes natural weighting of the visibilities and is a close approximation to the noise properties of the weighting scheme used by default in AIPS.

We find that the rms in the difference image cube is higher than the expected thermal noise given by Equation (2.4) by a factor of between four and seven across the frequency range and that the excess is highest in the FM band. For an imaging sub-band of 0.92 MHz (since 28% of fine channels are flagged) and an integration time of 7 minutes (the hour of observations was split into four channel configurations and half of the integration time was lost due to network bandwidth limitations) the rms in the difference image slice shown in Figure 2.6 is approximately 1.3 Jy, whereas the expected thermal noise given by Equation (2.4) is approximately 0.2 Jy (including an additional factor of $\sqrt{2}$ due to the differencing). The main factor causing this discrepancy is thought to be imperfect calibration on both days causing incomplete subtraction of sources in the difference image. The same sky model was used to calibrate the concatenated data from both days. However within the FM band, there is a 60 Jy source (the Moon) in two different positions 13° apart on subsequent days. This leads to a calibration solution that is slightly in error for both days and a higher than expected rms noise in the difference cube. Another factor could be differences in the ionosphere between the two days which would affect the positions of sources in the field, resulting in imperfect subtraction. The errors in the difference image are included as error bars in Figures 2.8 and 2.10.

The integrated flux density of the central pixels of the difference cube gives the difference between the Moon flux density on September 24 and the sky flux density on September 25. This Moon−sky difference spectrum was calibrated by application of the correction factor $S_{\mathrm{calc}}(\nu)/S_{\mathrm{ICC}}(\nu)$ to give the calibrated spectrum shown in Figure 2.7. These observations clearly show the Moon to be a source of approximately 60 Jy across the FM radio band from 87.5 to 108 MHz and many of the residual spectral features apparent in Figure 2.5 have indeed been removed by the differencing process. The uncertainty in the flux density of 3C33 leads to an uncertainty of less than 3% in the flux density calculated for the Moon. Following the same steps, we extracted a lower signal-to-noise ratio spectrum for the second day, when the Moon had moved approximately 13° from the center of the tile primary beam. Since the tile primary beam full width half-maximum varies as approximately $25^\circ/(\nu/150\mathrm{MHz})$, the Moon's position on the second day corresponds approximately to the half-power point of the tile primary beam at 150 MHz. This spectrum is consistent with the spectrum obtained while the Moon was at the center of the beam as shown in Figure 2.7.

Excluding the FM radio band, the measured Moon-sky difference has the negative to positive trend of Figure 2.1, however the slope of the measured difference plot is still not a good fit to the predictions which have neglected reflected emission from Earth as shown in Figure 2.8. The error bars in Figure 2.8 represent the rms noise in each image slice for a square region of the difference image in between the Moon's position on each of the subsequent days. It was considered whether incorrect modeling of the reflected galactic emission could account for the discrepancy between predicted and observed Moon temperatures, however the spectral index required to fit the data is approximately $\beta = 4$, which is unrealistically high.

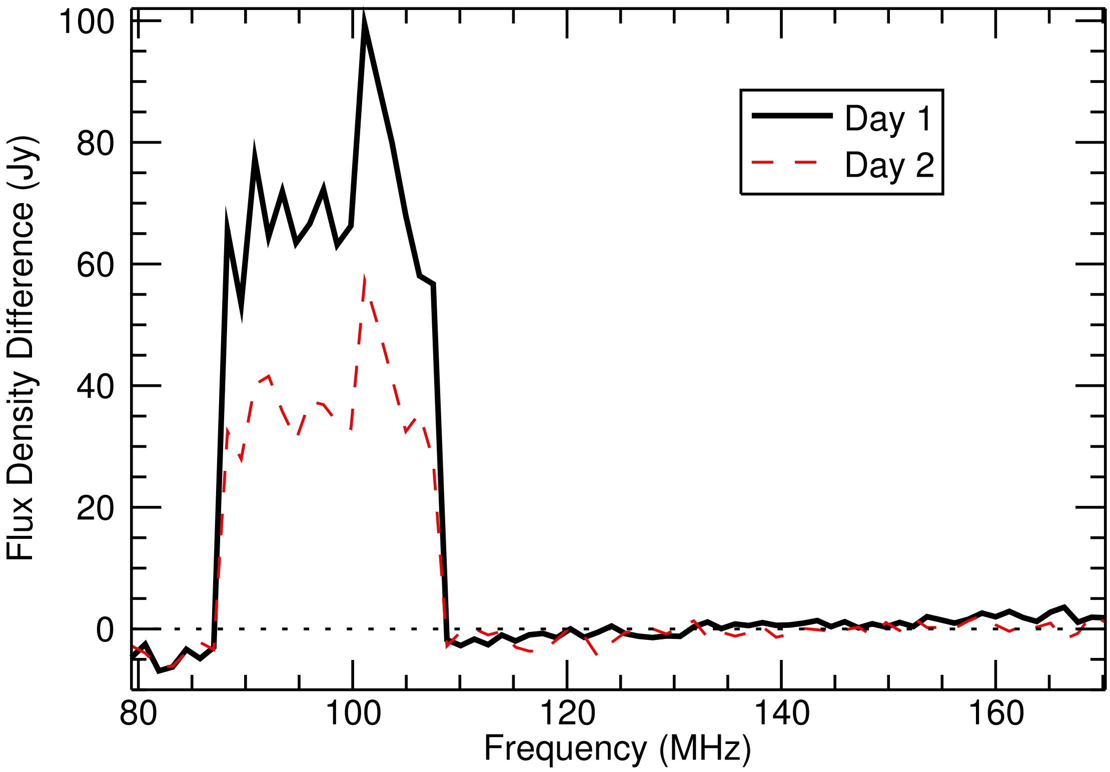

Figure 2.7 Integrated flux density of the "Moon" pixels in the Moon−sky difference image on Day 1 when the Moon was at the center of the beam and Day 2 when the Moon had drifted to approximately the half-power point of the beam. The flux density scale has been set using 3C33 as a reference, but no primary beam correction has been applied to the Moon spectra.

Similarly, an incorrect model for the spectrum of 3C33 would cause the bandpass calibration to be inaccurate, however we consider this an unlikely cause since 3C33 is such a bright, well-studied object, which has a very well-defined spectrum. Given the clear presence of reflected terrestrial FM radio transmissions from the Moon, it is likely that the discrepancy is due, at least in part, to additional reflected transmissions from Earth, outside of the FM radio band. However, we would expect such RFI to be more randomly distributed and not follow the smooth trend shown in Figure 2.8. One factor that was not considered in the bandpass calibration procedure was that of contaminating Galactic emission in the primary beam sidelobes, causing different, frequency-dependent variations in the measured flux-densities of the Moon and 3C33. Steep-spectrum Galactic emission entering thorough the frequency-dependent primary beam sidelobes, could result in large-scale, spatially-varying artifacts in the image cubes, and produce such an effect. Quantifying this effect, however, is difficult with the limited tools currently available, and we therefore leave this for future work.

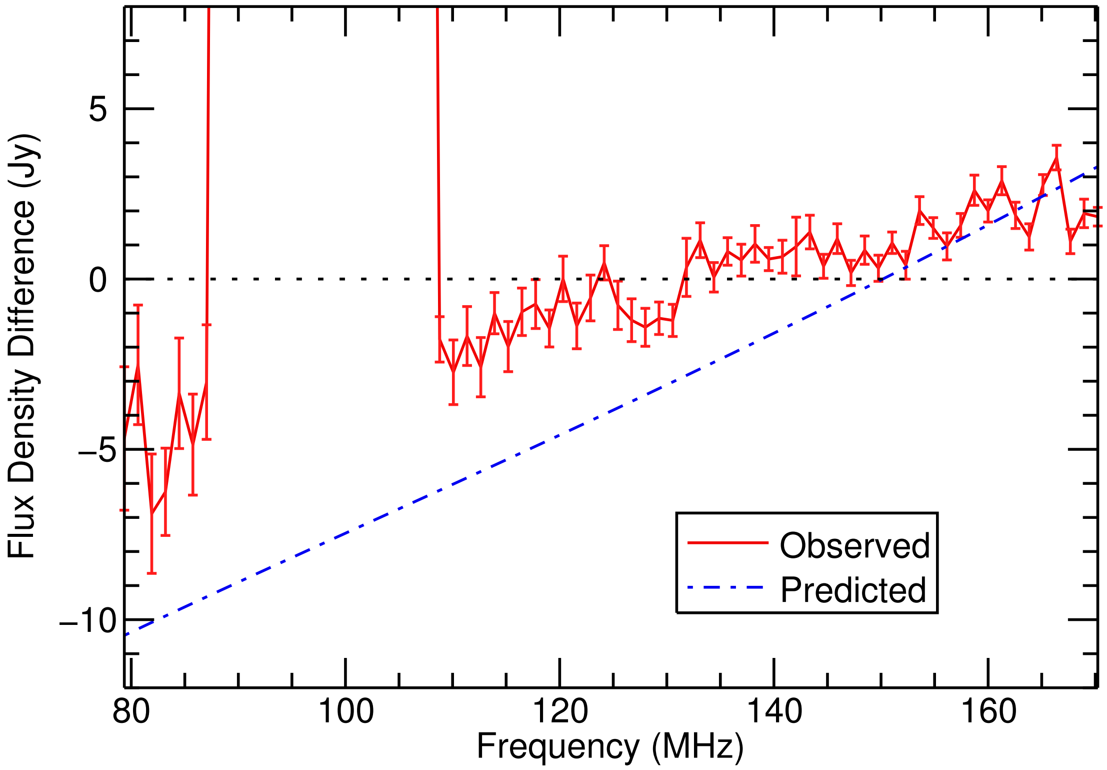

Figure 2.8 Comparison between the observed Moon−sky flux density difference on September 24 and the difference predicted for a model of the Moon that includes thermal emission and reflection of galactic background only. The excess flux density in the observations is attributed to the reflection of the Earth's radio leakage.

2.5. Analysis

The strength of Earth's radio leakage signal reflected by the Moon is of interest for several reasons.

1. Reflected radio emission presents an additional challenge for experiments aiming to use the Moon as a smooth spectrum calibration source for detection of the EoR signal.
2. The Moon will appear as a transient radio source that needs to be accounted for in current and future low frequency surveys and experiments.
3. The strength of the detected signal allows us to calculate how bright the Earth is as a radio source in this band and hence whether it might be detectable to technologically advanced extraterrestrial civilizations.

To address point (3) above, we can use these observations to calculate the equivalent isotropic power (EIP) of the Earth in the same way as Sullivan & Knowles (1985). However, because the MWA is an interferometer, our measurements only give us the difference between the background sky flux density and the Moon's flux density. The flux corresponding to

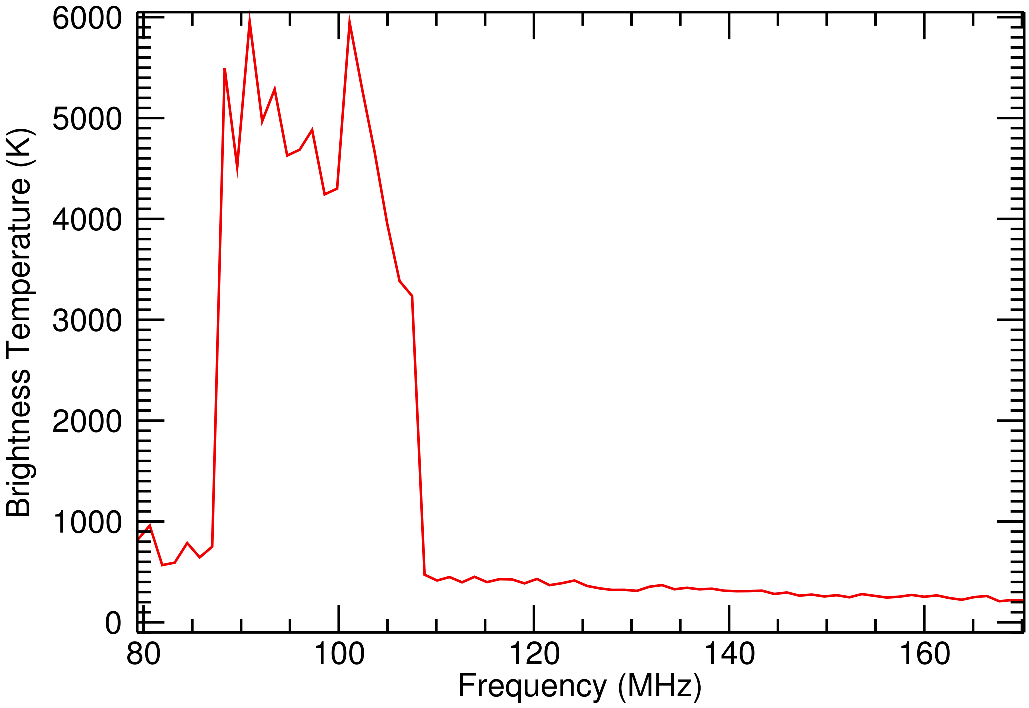

Figure 2.9 Disk average brightness temperature of the Moon calculated from MWA 32T measurements, combined with a model of the sky temperature derived from Rogers & Bowman (2008) and de Oliveira-Costa et al (2008).

the "zero spacing" is missing. We overcome this by converting the observed Moon flux density to brightness temperature by rearranging Equation (2.2) and adding the known sky temperature given by Equation (2.1). This gives us the observed Moon brightness temperature as shown in Figures 2.9 and 2.10. The brightness temperature of the Moon has been studied at a number of wavelengths, however the most relevant to these observations is that of Heiles & Drake (1963) which shows that we should expect the Moon to have a constant brightness temperature of 230 K at these frequencies. The excess brightness temperature due to reflected emission from the Earth is therefore calculated by subtracting the Moon's thermal emission and the component due to reflected galactic emission from this spectrum. This excess brightness temperature can then be converted back to flux density S_m by Equation (2.2) and to an EIP in Watts by

$$P_{\mathrm{earth}} = \frac{4^2 \pi 10^{-26} d_m^4 \Delta\nu S_m}{r_m^2 \rho_m}, \tag{2.5}$$

where d_m is the average Earth–Moon distance in m, $\Delta\nu$ is the size of the frequency bins in Hz, S_m is the observed flux density of the Moon in Jy, r_m is the radius of the Moon in m, and ρ_m is the Moon's reflectivity of 0.07 (Evans 1969).

Evaluating Equation (2.5) for the Moon's spectrum using 5 MHz wide frequency bins gives the histogram in Figure 2.11. To understand what the signal shown in Figure 2.11 means

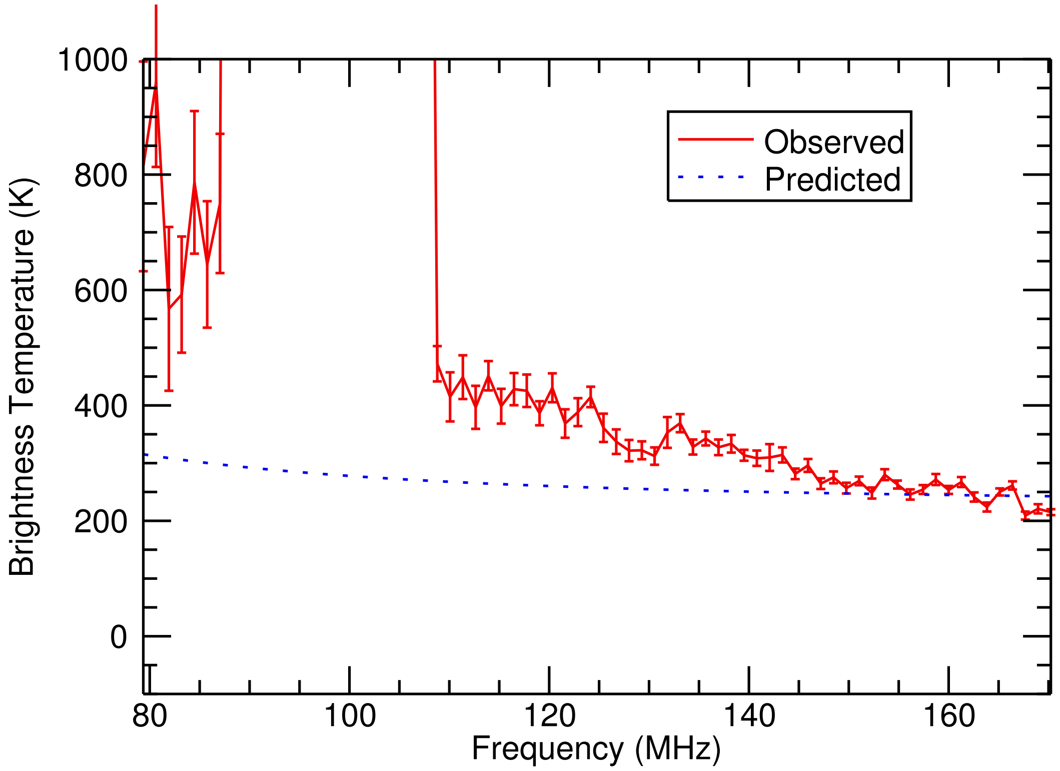

Figure 2.10 Disk average brightness temperature of the Moon calculated from MWA 32T measurements, combined with a model of the sky temperature derived from Rogers & Bowman (2008) and de Oliveira-Costa et al (2008). This is the same as Figure 2.9 but plotted on a different scale and with error bars based on the rms noise of the MWA 32T difference image. The dotted line is the thermal brightness temperature of the Moon of 230K from Heiles & Drake (1963) plus the expected reflection of galactic emission.

from the perspective of the search for extraterrestrial intelligence (SETI), we can calculate how bright the Earth might appear to an extraterrestrial observer. Summing the EIP over the 20.5 MHz of the FM band gives a value of approximately 77 MW, so to an observer orbiting our closest neighboring star, Proxima Centauri, the Earth would appear to be an extremely faint source of approximately 19 nJy within the FM radio band. As a comparison, the quiet Sun is a source of approximately 60,000 Jy (Lantos & Avignon 1975) as viewed from the Earth in this frequency band during periods of low solar activity. The Sun's total EIP in the FM band is therefore approximately 3.5 GW, so viewed from Proxima Centauri it would appear as a 0.85 μJy source and greatly outshine the Earth.

Detection of such a small signal by a nearby, technologically advanced civilization would require far superior instrumentation to our own, with even greater collecting area than is expected for future telescopes such as the Square Kilometre Array (SKA). A detection at these frequencies with an SKA equivalent instrument, with baselines long enough to resolve the Earth from the Sun, would require years of integration time. This is due largely to the high background sky temperature which dominates the system temperature at low

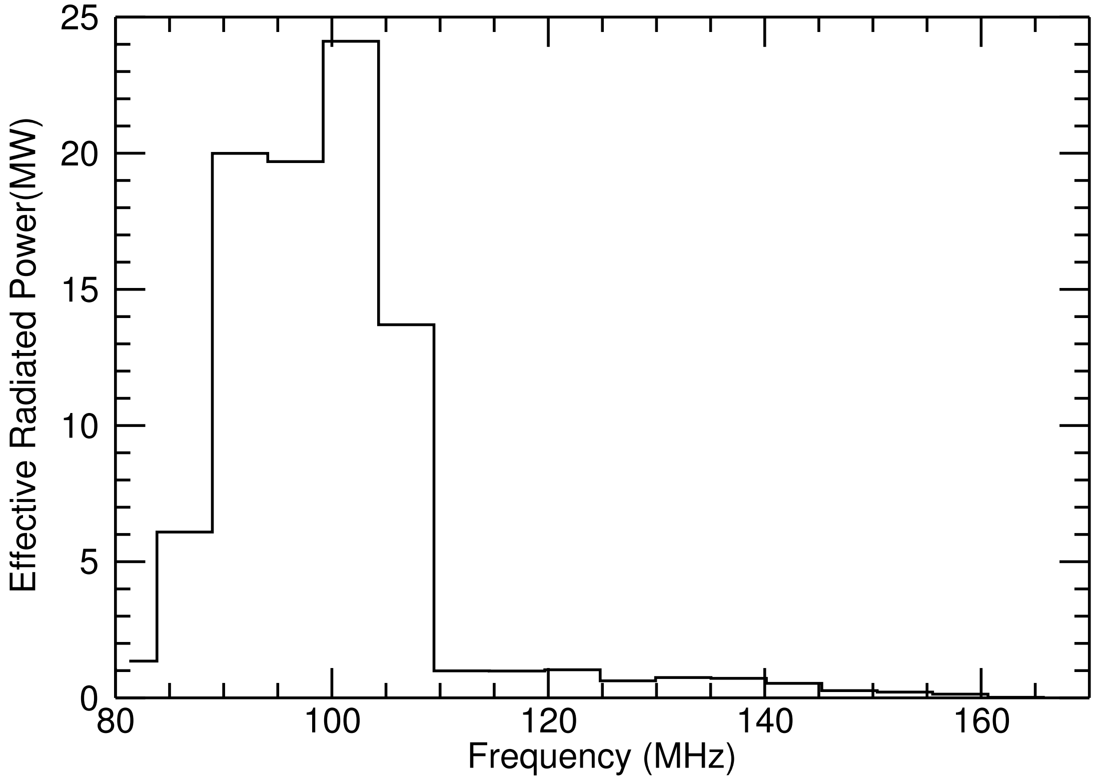

Figure 2.11 Equivalent isotropic power (EIP) of radio emissions from Earth as measured from MWA 32T observations of the Moon. The plot is a histogram with 5 MHz bins.

frequencies. Loeb & Zaldarriaga (2007) found that beamed radio leakage from a civilization within 23 pc of Earth, using high power military type radars similar to our own, should be detectable by the next generation of low frequency radio interferometers. However we note that most of these types of systems on Earth operate at higher frequencies. For this reason, radio leakage from the Earth at higher frequencies is more likely to be detectable, as the background sky temperature is lower and our highly beamed, military radars operate in the GHz frequency range. SETI experiments planned for the SKA are therefore more focused at frequencies between 1 and 10 GHz (Tarter 2004). The long baselines of the SKA will also provide the required angular resolution and RFI rejection capabilities required for such SETI searches, the importance of which have been demonstrated by recent proof-of-concept SETI observations using very long baseline interferometry techniques (Rampadarath et al 2012).

The observed Moon−sky flux density difference indicates that more observations are needed to properly characterize the Moon's radio properties at low frequencies if the Moon is to be used as a smooth spectrum calibrator for detection of the EoR signal. The very high frequency part of the radiofrequency spectrum from 30 to 300 MHz is used for many applications (ACMA 2009) including FM broadcasting, aeronautical radionavigation and communications, and amateur radio to name a few. These will all contribute to the reflected radio signal received on Earth from the Moon as evidenced by Figure 2.8. However there are methods that could be employed to reduce the impact of this reflected RFI on observations and some of these are discussed below.

The RFI signals from the Moon are expected to be strongest from the sub-Earth point where the surface behavior is closest to specular reflection. The higher spatial resolution of the completed MWA with 128 tiles and 3 km baselines will enable us to isolate the specular and diffuse reflection regions and take spectra from regions of the Moon less affected by reflected RFI from Earth.

A higher spectral resolution investigation may also provide a means of avoiding reflected RFI. In many countries including Australia and the United States (ITU 2001) FM broadcast frequencies are assigned with a channel separation of 200 kHz and a maximum frequency deviation of ±75 kHz, leaving a 'guard band' of at least 25 kHz above and below the modulation. Observation in these guard bands should be free from RFI contamination or at least be affected at a reduced level. Similarly, radio-quiet bands may be found in regions of the spectrum outside of the FM band if observing at higher spectral resolution.

The reflected radio emission from the Moon will clearly also vary strongly as a function of time as different regions of the Earth come into the line of sight of the Moon. Since terrestrial broadcasting is generally directed toward the horizon rather than straight up, the worst RFI contamination is likely to occur when the Moon's position falls near the plane of the horizon at the most highly populated regions of the Earth. Hence RFI contamination may be reduced by planning observations at times when the geometry between the Moon, the telescope, and population centers on Earth minimizes the radio signal beamed toward the Moon.

An additional concern is that the occasional presence of the Moon in observations of deep fields that are visited repeatedly may present complications due to the rapid movement of the Moon with its strong reflected signal, which itself is rich in time-variable spectral structure as the Earth rotates and different population centers illuminate the Moon with radio transmissions. Furthermore, the Moon subtends sufficient solid angle that ensembles of background sources will be steadily occulted and re-exposed in areas of long integration. This is a concern for some instruments, since the principles of aperture synthesis and coherent integration with interferometers rely on the constancy of the radio sky throughout the integration. However, instruments such as the MWA and LEDA (Greenhill & Bernardi 2012) will implement snapshot imaging with subsequent combination in the image domain, an approach that might be made robust to this kind of variability.

2.6. Conclusions

The MWA 32 tile prototype system was used to observe the Moon over two subsequent nights in order to test the viability of using the Moon as a smooth spectrum calibration source for EoR signature detection. A direct differencing experiment between the Moon and sky flux density from the same patch of sky over the two nights found that the Moon does exhibit the properties expected for a cool thermally emitting body, but that the spectrum is corrupted by radio leakage from Earth, most notably within the FM radio band of 87.5 – 108 MHz. From this reflected signal we were able to measure the EIP of the Earth in the FM radio band which was found to be approximately 77 MW.

The implications of these observations are that RFI from Earth will be a significant challenge to overcome if the Moon is to be used as a smooth spectrum calibration source for EoR detection. Reflected terrestrial radio emissions will have to be carefully taken into account in any future experiments and more Moon observations are required to characterize this RFI. Additionally, it was found that the total signal being transmitted from the Earth in the FM radio band would be difficult, but not impossible, to detect by a nearby technologically advanced civilization with superior radio astronomy technology to our own.

CHAPTER 3

The giant lobes of Centaurus A observed at 118 MHz with the Murchison Widefield Array

This chapter has been previously published as 'The giant lobes of Centaurus A observed at 118 MHz with the Murchison Widefield Array', McKinley, B., Briggs, F., Gaensler, B. M., et al., 2013, MNRAS, 436, 1286.

3.1. Abstract

We present new wide-field observations of Centaurus A (Cen A) and the surrounding region at 118 MHz with the Murchison Widefield Array (MWA) 32-tile prototype, with which we investigate the spectral-index distribution of Cen A's giant radio lobes. We compare our images to 1.4 GHz maps of Cen A and compute spectral indices using temperature–temperature plots and spectral tomography. We find that the morphologies at 118 MHz and 1.4 GHz match very closely apart from an extra peak in the southern lobe at 118 MHz, which provides tentative evidence for the existence of a southern counterpart to the northern middle lobe of Cen A. Our spatially averaged spectral indices for both the northern and southern lobes are consistent with previous analyses, however we find significant spatial variation of the spectra across the extent of each lobe. Both the spectral-index distribution and the morphology at low radio frequencies support a scenario of multiple outbursts of activity from the central engine. Our results are consistent with inverse-Compton modelling of radio and gamma-ray data that support a value for the lobe age of between 10 and 80 Myr.

3.2. Introduction

Radio galaxies consist of two or more extended regions of magnetized plasma and synchrotron-emitting, relativistic charged particles, emanating from the active galactic nucleus (AGN) of a host galaxy (Begelman et al. 1984). These radio lobes interact with the intergalactic medium and/or intracluster medium and grow in size over time, due to either a quasi-continuous injection of particles from the jets or possibly separate episodic outbursts (Subrahmanyan et al. 1996; Morganti et al. 1999). At GHz frequencies, the emission spectra of radio galaxies, within the observing band of a typical radio telescope, are often well described by a simple power law of the form $S \propto \nu^{\alpha}$, as a function of frequency, ν, where S is the observed flux density and α is the spectral index. The power-law spectrum results from the power-law energy distribution of relativistic particles producing the observed synchrotron emission. Inverse Compton emission may also be observed in radio galaxies when relativistic particles upscatter low-energy background photons, the most abundant of which are from the cosmic microwave background, to higher energies. Combining X-ray and gamma-ray data with radio data can therefore be used to constrain models of synchrotron and inverse Compton emission to estimate the physical properties of radio galaxies.

One of the most well-known and well-studied radio galaxies is Centaurus A (Cen A). This Fanaroff & Riley (FRI; Fanaroff & Riley 1974) radio source associated with the elliptical galaxy NGC5128 was first discovered by Bolton (1948) at 100 MHz, the frequency we return to here in this paper. Cen A lies at a distance of a mere 3.8 ± 0.1 Mpc (Harris et al. 2010), making it the closest radio galaxy by a large margin and providing an ideal laboratory for studying the properties and particle acceleration histories of radio galaxies. Cen A has been studied intensely over a wide range of wavelengths and physical scales (see Israel 1998 for a review), but there is still much to be learned from this complex, nearby object.

The giant lobes of Cen A have a distinctive morphology with multiple peaks and orientations that change with distance from the core. They comprise a pair of inner lobes emanating from the core of the galaxy with a combined extent of ~11 kpc, aligned at a position angle of 55° anti-clockwise from the north–south axis (Schreier et al. 1981; Clarke et al. 1992). Further from the core, the northern inner lobe is followed by a 'northern middle lobe' (NML, Morganti et al. 1999), which is the brightest part of the northern lobe situated ~30 kpc from the core and orientated at a position angle of 45°. No southern counterpart to the NML has so far been detected in total intensity measurements (Feain et al. 2011), but O'Sullivan et al. (2013) have reported the existence of a region of high fractional polarization in the southern lobe that could be the oppositely directed counterpart to the NML. Finally, there are the giant outer lobes, which have a combined extent of ~500 kpc. The northern outer lobe has a position angle of between 0° and 20° closest to the core, and then has an abrupt change in position angle at approximately RA (J2000) $13^{h}25^{m}00^{s}$, Dec (J2000) $-40°58'00''$ (Feain et al. 2011; Haynes et al. 1983; Cooper et al. 1965). The southern outer lobe also experiences a change in position angle, but one that is more gradual.

To produce the complex structure of Cen A, current models invoke a combination of separate, multiple outbursts of nuclear activity (Morganti et al. 1999), combined with interaction with the ambient medium (Norman et al. 1988; Burns 1986) and a precessing central engine (Haynes et al. 1983). An alternative explanation is that the jets interact with rotating gaseous shells (identified in optical observations by Malin et al. 1983, in 21 cm emission by Schiminovich et al. 1994, and in the far-infrared by Stickel et al. 2004) surrounding the host galaxy (Gopal-Krishna & Saripalli 1984; Gopal-Krishna & Wiita 2010). Further observational and theoretical work is required to determine the origins and evolutionary history of the giant lobes.

A new generation of low-frequency radio interferometers is beginning to produce scientific results and can provide more information on the shape of the radio spectrum of radio galaxies such as Cen A with reasonable angular resolution. These instruments, including the Low Frequency Array (LOFAR; van Haarlem et al. 2013), the Precision Array for Probing the Epoch of Reionization (PAPER; Parsons et al. 2010) and the Murchison Widefield Array (MWA; Tingay et al. 2013; Bowman et al. 2013; Lonsdale et al 2009), aim to detect the faint redshifted 21-cm spectral line signal from the epoch of reionization (EoR). They have been designed to have the wide fields of view and short baselines required to detect the EoR signal, which is expected to have characteristic angular scales up to tens of arcmin (Pritchard & Loeb 2011; Morales & Wyithe 2010; Furlanetto et al 2006), as well as the longer baselines that provide the angular resolution required for accurate instrument calibration. Therefore, these types of instruments are also ideally suited to measuring the low-frequency properties of extended objects such as Cen A.

In this paper we present a spatially resolved radio-frequency spectral-index study of the giant lobes of Cen A using data from the MWA 32 Tile prototype (MWA 32T) at 118 MHz and Parkes data at 1.4 GHz (O'Sullivan et al. 2013). In Section 2, we discuss previous radio observations and spectral analyses of the giant lobes. In Section 3, we provide the details of the MWA observations and data reduction. In Section 4, we present the results of the MWA observations and our analysis of the spatial and spectral properties of the giant lobes between 118 MHz and 1.4 GHz. In Section 5, we discuss the results in relation to current models of the origin and evolution of the giant lobes.

3.3. Previous observations and analyses of the giant lobes

Cen A has a large angular extent of $4^\circ \times 8^\circ$, making observations of the *entire* radio source difficult, especially when attempting to obtain images with reasonable angular resolution. Studies of the entire source at radio frequencies include full polarization maps obtained by Cooper et al. (1965) at 406, 960, 1410, 2650 and 5000 MHz using the Parkes Radio Telescope (with resolutions ranging from 48 to 4 arcmin depending on frequency) and polarization and total intensity maps of the full source at 4.75 GHz and 4-arcmin resolution produced by Junkes et al. (1993). More recently, Feain et al. (2011) have mapped the radio continuum structure of Cen A at 1.4 GHz at high angular resolution and O'Sullivan et al. (2013) have produced a more detailed Faraday rotation analysis.

Low-frequency observations of the giant lobes of Cen A have, until recently, suffered from poor angular resolution, e.g. the 408 MHz, $0^\circ\!.85$ resolution map of Haslam et al. (1982) and the 45 MHz, $4^\circ\!.6$ resolution map of Alvarez et al. (1997). Low-frequency (below 100 MHz), low angular resolution studies of the Cen A giant lobes have also been conducted by Hamilton & Haynes (1968), Ellis & Hamilton (1966), Shain (1959) and Sheridan (1958). A recent paper from the PAPER collaboration (Stefan et al. 2013) mapped Cen A and the surrounding field at 148 MHz with 20-arcmin resolution and constructed a spectral-index map using the frequency variation within their 100 MHz observing band; they claim to find evidence of spectral flattening in turbulent regions of the lobes identified by Feain et al. (2011). Their spectral-index analysis is only qualitative, however, due to large uncertainties in their total flux measurements, resulting in physically unrealistic spectral index values of between 0 and -3 (see Stefan et al. 2013, fig. 4).

3.3.1. Previous spectral analyses

The only spatially resolved spectral-index maps of the giant lobes of Cen A in the literature are by Combi & Romero (1997) and more recently by Stefan et al. (2013). The Combi & Romero (1997) map utilizes single-dish data from Parkes at 408 MHz and 1.4 GHz and finds the spectral index to steepen at the edges of the northern lobe and to steepen with distance from the core in the southern lobe. However, when this spectral-index map is compared with the Cooper et al. (1965) map of total intensity at 406 MHz, there is a correlation in the southern lobe between areas of steep spectral index and the estimated foreground component of emission from the 'spur' feature of Galactic emission to the south-east (Cooper et al. 1965). The spectral steepening in the northern lobe appears to correlate with regions of lower total intensity (and hence lower signal-to-noise ratio against the Galactic foreground). Stefan et al. (2013) attempt to map the spectral-index distribution of the giant lobes within the PAPER bandwidth and claim that the spectral index between 130 and 165 MHz varies as a function of distance from the core, steepening initially and then flattening towards the outer regions of the giant lobes. However, there appears to be a correlation between the total intensity and spectral-index maps in this case, indicating a possible systematic error in the calculation related to signal-to-noise ratio. The error in the spectral-index maps is likely to be high in regions of low total intensity of the lobes where the bright Galactic foreground emission at low frequencies (de Oliveira-Costa et al 2008; Bernardi et al 2009) is a significant fraction of the emission, and particularly in the case of Stefan et al. (2013) where the fractional frequency over which the spectral index is computed is very small.

All other spectral-index calculations have been performed by taking ratios of flux densities summed over large regions, for example Alvarez et al. (2000) and Hardcastle et al. (2009). This type of calculation is prone to error due to the inclusion of flux from foreground and background sources and constant offsets in maps due to missing short spacings. This is reflected in the large errors included in the spectral-index estimates of Alvarez et al. (2000). The most detailed spectral-index measurements of the giant lobes to date are from Hardcastle et al. (2009), who split the lobes into five large regions and use a combination of single-dish and 5-year Wilkinson Microwave Anisotropy Probe (WMAP) data (Hinshaw et al. 2009) to constrain models of the spectral energy distribution (SED) and to make predictions as to whether the *Fermi* Large Area Telescope (Fermi-LAT; Atwood et al. 2009) would detect gamma-ray emission from the lobes. Subsequent results from Fermi-LAT revealed strong gamma-ray detections in both the northern and southern lobes of Cen A (Abdo et al. 2010a; Yang et al. 2012).

3.4. Observations and Data Reduction

The MWA 32T was a scaled-down prototype version of the MWA, consisting of 32 antenna tiles, each tile consisting of 16 crossed-dipole antennas above a conducting mesh ground plane. The prototype was operated over the period 2007 September to 2011 September within the radio-quiet Murchison Radio Observatory in Western Australia at a latitude of

-26°.7. Cen A was observed with the MWA 32T over three consecutive nights from 2011 April 29 to 2011 May 1, using 80-s snapshot observations scheduled over a wide range of hour angles. Each snapshot observation used a different, fixed setting of the analogue beamformers. The observations used in this paper consisted of a 30.72 MHz frequency band covering the frequency range of 108 to 139 MHz. The resulting data set contained 80 snapshot observations, centred on 124 MHz, but only the lower 20 MHz was used in imaging for reasons that will be discussed below. These snapshot observations were converted to UVFITS format and imported into CASA (Common Astronomy Software Applications) at a resolution of 1 s in time and 40 kHz in frequency. CASA was used for all further data reduction. AOFLAGGER (Offringa et al. 2010, 2012) was used to flag radio frequency interference (RFI) in each individual CASA measurement set. Additionally the central 40-kHz fine channel in each 1.24-MHz 'coarse channel' and three fine channels at each coarse channel edge were flagged due to known rounding errors and aliasing, respectively. The measurement sets were then averaged to 4-s and 160-kHz resolution and concatenated into a single CASA measurement set.

We performed self-calibration on Cen A itself, beginning with a simple, flat-spectrum point source model at the phase centre, while excluding baselines shorter than 100 λ. This was an effective calibration strategy, since the longer baselines do not resolve the bright central core of Cen A, while excluding the shorter baselines removes the effect of the diffuse emission. A multi-frequency synthesis image of the entire 30.72 MHz bandwidth was made using a relatively shallow CLEAN in CASA in order to improve the sky model, and a single self-calibration iteration was then performed across this frequency band. The final image used a 20-MHz sub-band at a centre frequency of 118 MHz in order to have the widest (and simplest) primary beam shape. Use of only the lower 20 MHz of the bandwidth was found to reduce imaging artefacts around the centre of the source. It was found that natural weighting and a simple Cotton-Schwab CLEAN, without using the multiscale option, produced the best images. The W-projection algorithm (Cornwell et al. 2008) was used to account for widefield effects.

The imaging did not take into account the changing primary beam shape that varies as a function of frequency and time, making the beam and its polarization properties different for each beamformer setting. This could be addressed using a Mosaic CLEAN if MWA primary beam shape images could be supplied to CLEAN. However, this functionality is currently not available and would require further development to be included in CASA. Our approach differs from that of Williams et al (2012), who combined snapshots in the

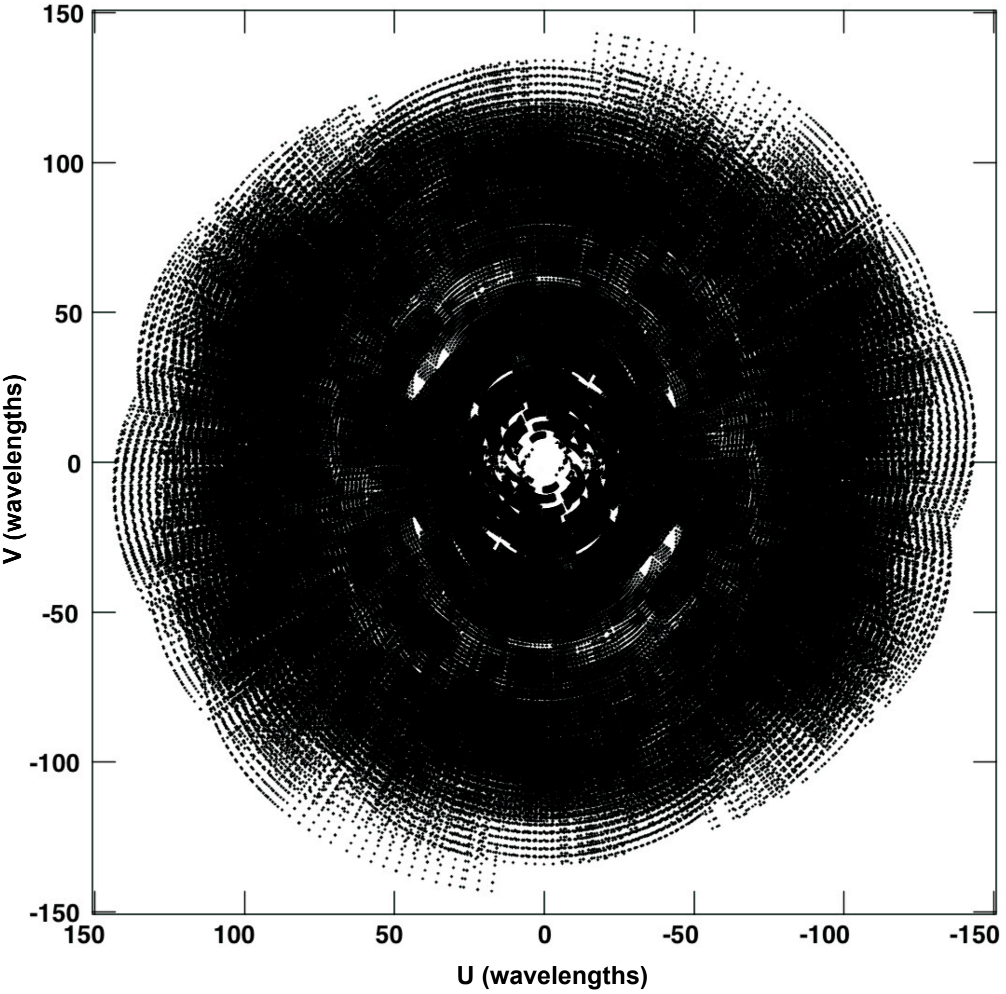

Figure 3.1 Combined uv-coverage for all snapshots centred on 118 MHz with a bandwidth of 20 MHz, in units of wavelength. The plot does not include the three shortest baselines, which were excluded from calibration and imaging.

image domain, allowing them to assume a constant primary beam shape over each snapshot. The difference in approach is due to the scientific goal of imaging the large-scale structure associated with Cen A and the foreground Milky Way with a very small number of short baselines. Earth rotation synthesis was required in order to increase the uv-coverage of the short spacings and to allow the CLEAN algorithm to reconstruct the large-scale structure. The combined uv-coverage for all snapshots at a centre frequency of 118 MHz, with a bandwidth of 20 MHz, is shown in Fig. 3.1.

The MWA tile beam shape is different for both instrumental polarizations and varies as a function of frequency and time (due to different beamformer settings). An average 'Stokes I'

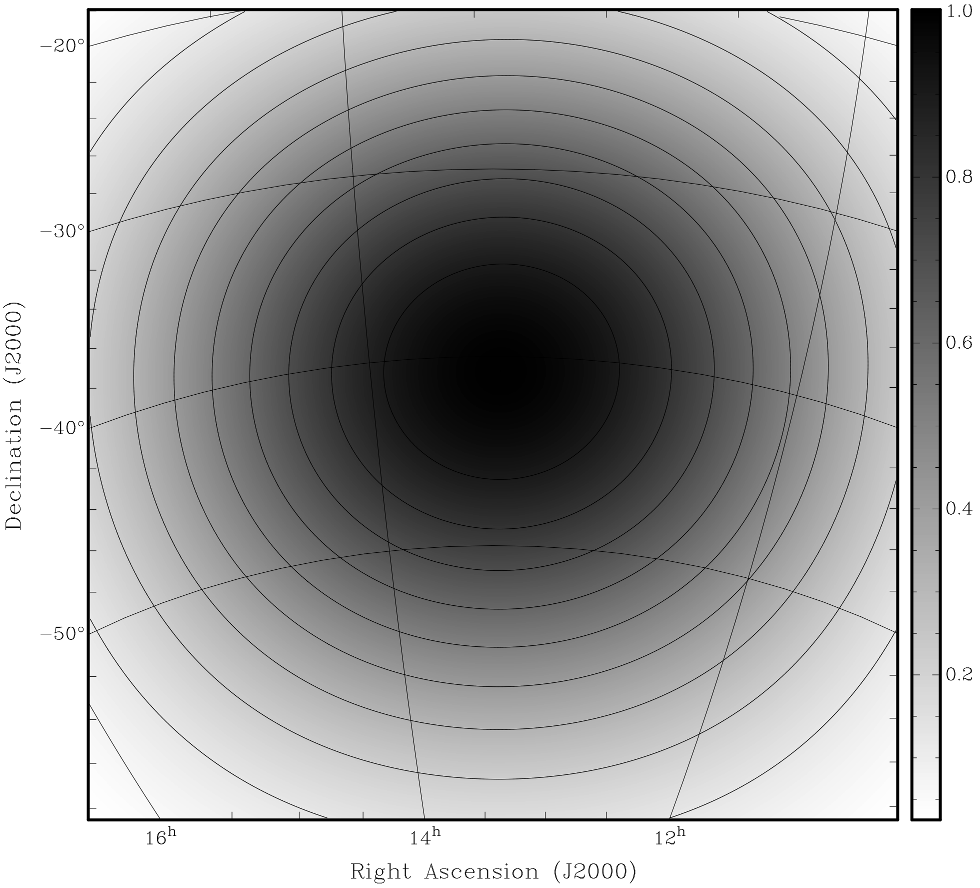

Figure 3.2 Average tile primary beam from an analytic model. The centre frequency is 118 MHz. Contours are from 10 to 90 per cent of the peak gain (normalized to 1), incrementing in steps of 10 per cent.

primary beam image was calculated by summing analytic primary beams calculated for each instrumental polarization at each beamformer setting, using the same analytic primary beam model as Williams et al (2012), and then taking the average of the two instrumental polarization beamshapes. The average primary beam for the 118-MHz image is shown in Fig. 3.2. The peak of the average primary beam in Fig. 3.2 is approximately 2° north of the core of Cen A, due to the discrete nature of the beamformer settings used to electronically point the telescope tiles. The average primary beam correction was applied in image space to the final cleaned image. This approach assumes that each tile beam is the same, when in fact there will be some variation in the beam shapes between tiles. Bernardi et al. (2013) have shown that the error introduced by the tile beam model used in MWA 32T observations at 189 MHz, also assuming the same beam shape for each tile, is at about the 2% level.

Since self-calibration on Cen A did not provide us with an overall flux scale, the flux scale was set using an ensemble of point sources within the full-width half-maximum (FWHM) of the primary beam. The Culgoora catalogue (Slee 1977, 1995) is the only point source catalogue

Table 3.1 Sources Used to Set Flux Density Scale

Source Name	Expected flux at 118 MHz (Jy)	Scaling factor
PKS B1346-391	23.2	1946
PKS B1246-410	31.6	1156
PKS B1247-401	15.4	1185
PKS B1340-373	6.6	1699
PKS B1355-416	32.1	1237
PKS B1243-412	13.7	1870
PKS B1233-416	12.7	1153
PKS B1407-425	13.4	1253
	Average scaling factor:	1438

covering this region of sky at the frequencies of interest. Eight unresolved Culgoora sources with measurements at both 80 and 160 MHz were identified within a 10° radius of Cen A. A scaling factor was calculated for each of these sources by dividing its expected flux density (based on the Culgoora measurements at 80 and 160 MHz) by its measured flux density in the primary-beam-corrected MWA image. The details of the sources used to set the flux density scale in the MWA map at 118 MHz are given in Table 3.1. The scaling factors are large because the flux density of the core of Cen A was arbitrarily set to 1 Jy in the initial calibration. The standard deviation of the scaling factors listed in Table 3.1 is 319, calculated as $\sigma = \sqrt{\frac{1}{N}\sum_{i=1}^{N}(x_i - \mu)^2}$, where N is the number of Culgoora sources used, x_i is the ith scaling factor and μ is the average of the scaling factors. This value is 22% of the average scaling factor of 1438. We therefore estimate the uncertainty in the flux scale of the MWA image of Cen A to be ±22%. This is similar to the result of Jacobs et al. (2013a) who calculate a flux-scale uncertainty of 20% for the MWA 32T over the full extent of its $\sim 25^\circ$ field of view and attribute most of this error to uncertainties in the primary beam model and to errors introduced by the CLEAN algorithm.

3.5. Results and Analysis

Fig. 3.3 shows the MWA image of the Cen A field at 118 MHz with the primary beam correction and flux scale applied. At this frequency, the spatial resolution is approximately 25 arcmin. The uv-range for this image was restricted to exclude the shortest three baselines of the MWA 32T that are problematic for calibration and imaging. This also effectively filters out features on scales larger than about 12°, which would include much of the large-scale Galactic emission expected at these frequencies. Due to the similarities between PAPER and the MWA, many of the same imaging and calibration challenges described by Stefan et al. (2013) have also been encountered in this work. We note that the missing short baselines in the MWA images result in a negative bowl around Cen A, which affects the measurement of flux densities to some extent. Fig. 3.4 shows a profile through the centre of the MWA image along a constant declination of (J2000) −43°01′9″. It appears from Fig. 3.4 that the negative bowl, on the order of a few Jy/beam, is roughly constant within a 5° radius of the core of Cen A and hence has little effect on most of the subsequent analysis of Cen A's giant lobes. The total integrated flux density of the entire source in our 118 MHz image, measured by summing the flux in Cen A above the 2.5 Jy/beam contour level, is 6620 ± 1460 Jy. Alvarez et al. (2000) show that the flux-density spectrum integrated over the full extent of Cen A follows a power law with a spectral index of -0.70 ± 0.01 from 10 MHz to 4.75 GHz and their fig. 2 predicts a flux density of approximately 7250 Jy. Our measured flux density for the entire source is consistent with the predicted value of Alvarez et al. (2000).

The peak brightness of Cen A at 118 MHz is 1698 ± 374 Jy/beam (where the Gaussian restoring beam is 0°.38 × 0°.32 with a major axis position angle of 171°) at RA (J2000) $13^{h}25^{m}28^{s}$, Dec (J2000) −43°01′9″. This position is consistent with the known position of the centre of the radio source given by Ma et al. (1998). At our angular resolution of 25 arcmin, the central resolution element contains the entirety of the inner lobes and the brightest part of the NML. The rms in a typical 'empty' region of the image is approximately 0.5 Jy/beam, giving a dynamic range of at least 3000. At this frequency, the primary beam FWHM is approximately 31°, and many faint point sources occupy the field of view. Apart from Cen A, other distinctive features visible in Fig. 3.3 include the supernova remnant G296.5+10.0 in the south-west and the Galactic plane along the bottom of the image. The Galactic plane is not well reconstructed by the MWA 32T due to its large angular size, which is not sampled by the shortest baselines. Additionally, the Galactic plane is well outside the FWHM of the tile primary beam. Despite the relatively small number of short baselines, faint diffuse emission from the Milky Way on scales smaller than 12° can be seen across the map. To show that these large-scale structures in the surrounding field are real and not imaging artefacts, we show in Fig. 3.5 a comparison between the 408 MHz map of Haslam et al. (1982) and the MWA 118 MHz map. The MWA image has been smoothed to the same resolution as the 408 MHz map (0°.85). The original Haslam et al. (1982) data show a roughly linear

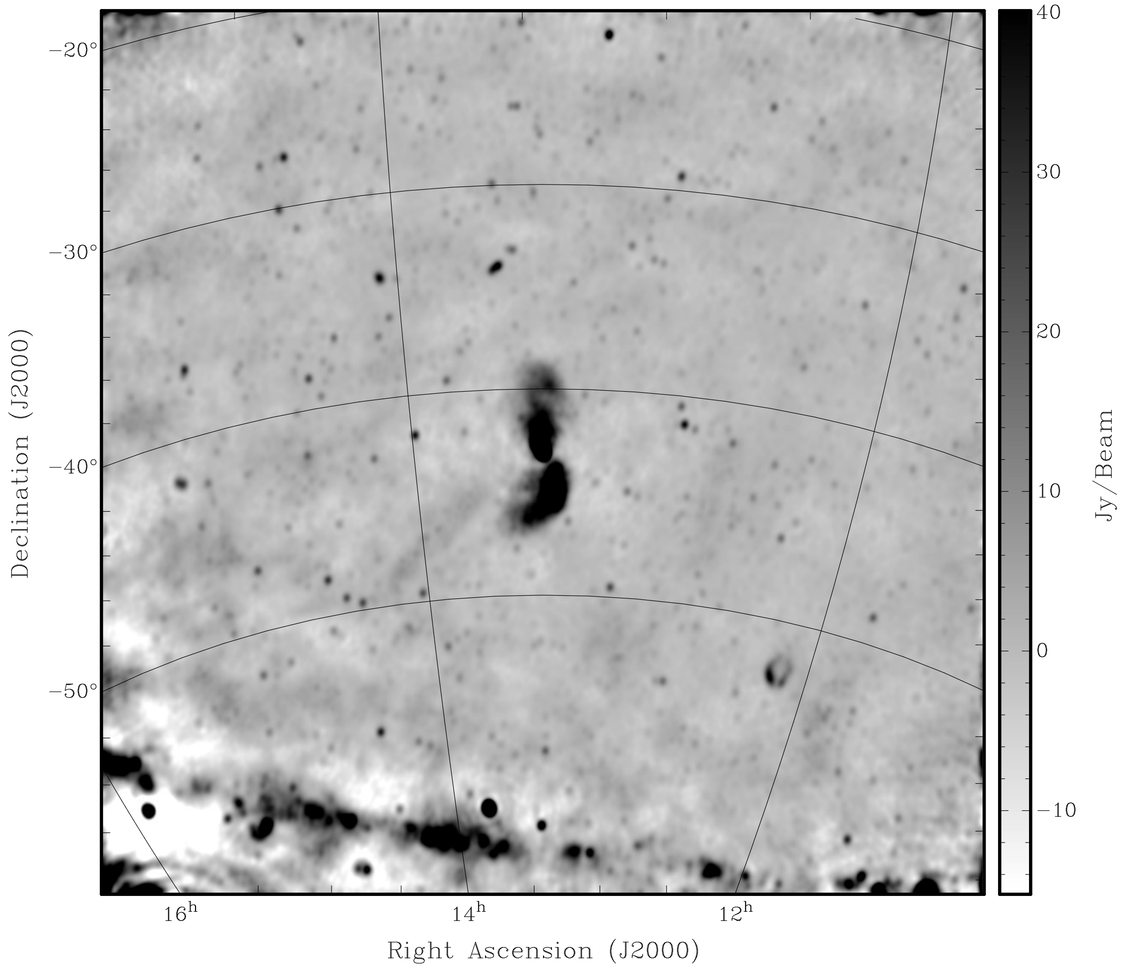

Figure 3.3 Cen A and surrounding field at 118 MHz with the MWA 32-Tile prototype. The image is shown on a linear scale between −15 and +40 Jy/beam. It has an angular resolution of 25 arcmin and an rms noise of approximately 0.5 Jy/beam in 'empty' regions of the map.

decrease in average intensity from the south-east corner to the north-west (presumably due to Galactic emission). This large-scale gradient, undetectable to the shortest baselines of the MWA 32T, has been subtracted away from the Haslam et al. (1982) map to make the smaller-scale structures clearer. In Fig. 3.5, much of the diffuse structure between the two images matches well by eye, particularly the shape of the giant radio lobes of Cen A themselves and the 'spur' feature to the south-east (label 1). Labels 2 and 3 in Fig. 3.5 show two other distinctive large-scale foreground features that appear in both maps. The qualitative comparison between the Haslam et al. (1982) and MWA maps confirms that the features on the angular scales associated with the Cen A giant lobes are being reconstructed properly in the MWA image. We do not pursue a spectral comparison with the Haslam map as the angular resolution is too coarse and the frequency difference between the two maps is too small for our purposes. Instead, we use data at 1.4 GHz for our spectral analysis.

Fig. 3.6 shows the MWA image at 118 MHz (in both gray scale and contours) overlaid with

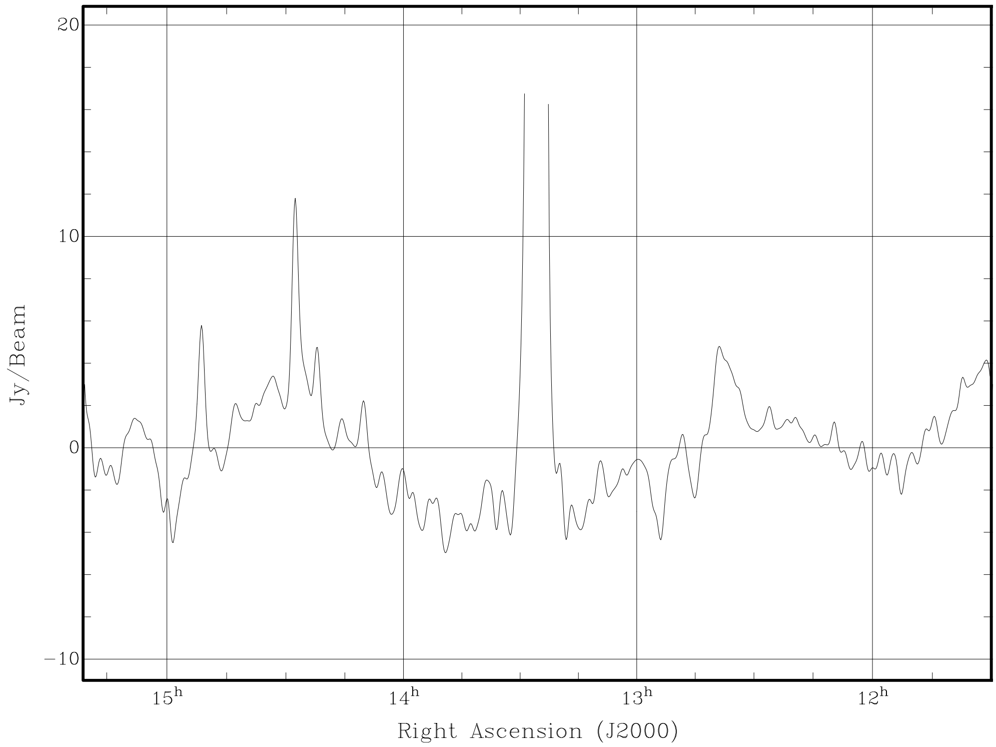

Figure 3.4 Profile through the centre of the MWA 118 MHz image of Cen A (see Fig. 3.3) along a constant declination of (J2000) −43°01′9″, showing the negative bowl surrounding the core of Cen A in the image.

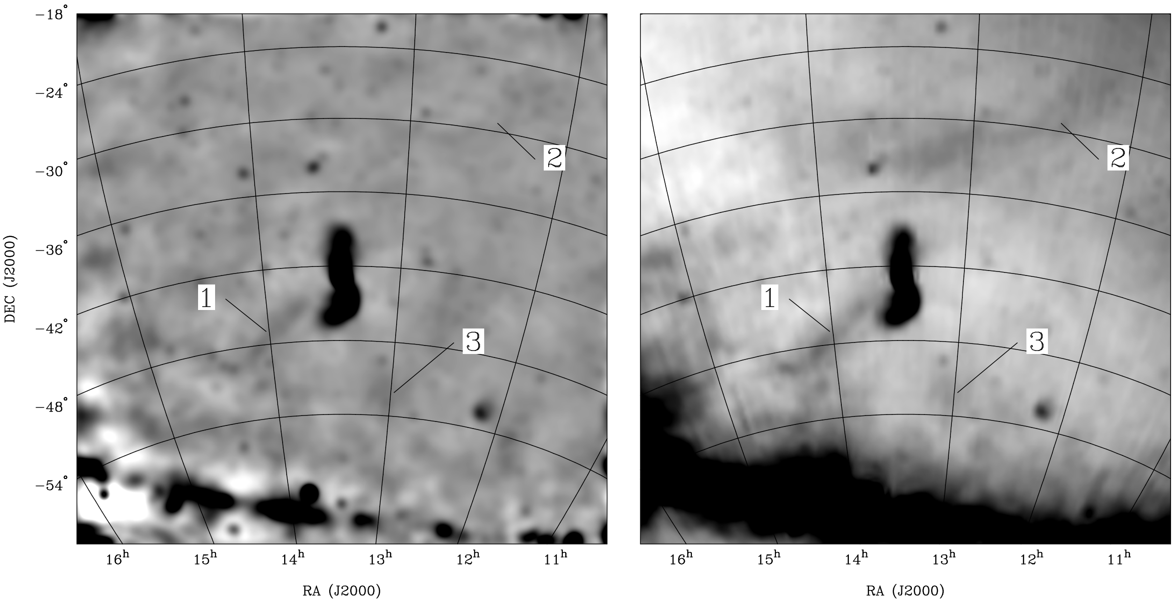
−18°
−24°
−30°
−36°
−42°
−48°
−54°
DEC (J2000)
1
2
3
16h
15h
14h
13h
12h
11h
RA (J2000)
1
2
3
16h
15h
14h
13h
12h
11h
RA (J2000)

Figure 3.5 Comparison between the MWA 118 MHz image (left) and Haslam et al. (1982) 408 MHz image (right), both smoothed to the same angular resolution of 0.°85. A linear brightness gradient has been subtracted from the Haslam et al. (1982) map to make the smaller-scale structures clearer. The faint diffuse structure on scales less than 12° matches well by eye. Labels 1 to 3 indicate large-scale foreground features clearly present in both maps.

the Parkes 1.4 GHz Stokes I contours from O'Sullivan et al. (2013). The 1.4 GHz map has been smoothed to the same resolution as the MWA map. The structure of Cen A at 118 MHz matches very closely with the structure seen at 1.4 GHz. However there are a few areas where the morphologies appear to be slightly different. Of particular interest is the northern part of the southern giant lobe at approximately RA (J2000) $13^{\mathrm{h}}23^{\mathrm{m}}$, Dec (J2000) $-43^{\circ}45'$, where there appears to be additional structure at 118 MHz that is not present in the 1.4 GHz image. This is discussed further in combination with the spectral tomography results in Section 4.1.1. In the central regions of Cen A, it appears from Fig. 3.6 that the source is wider at 1.4 GHz than at 118 MHz. This is most likely due to the negative bowl in the MWA image, as discussed above, and not due to a region of inverted-spectrum emission.

3.5.1. Spectral index of the giant lobes

Calculation of the spectral index only within the 30 MHz MWA band is unlikely to produce accurate values since the fractional frequency coverage is too small to accurately measure changes in flux density. Instead, we compare data at 1.4 GHz (O'Sullivan et al. 2013) to our 118 MHz image in order to compute spectral indices. This larger frequency ratio makes the spectral-index calculations more robust to errors in both maps. The assumption of a single spectral index over such a large frequency range is simplistic as there could be curvature in the spectrum. However, between 118 MHz and 1.4 GHz the spectral curvature is expected to be small, as predicted by the inverse-Compton modelling of Yang et al. (2012); for example see their fig. 8. Additionally, Alvarez et al. (2000) have shown that the spectrum of the whole source, which is dominated by the flux-density of the giant outer lobes, closely follows a single power law, with no spectral break, between 10 MHz and 4.75 GHz. This provides further reassurance that there is little curvature in the spectrum of the Cen A lobes between 118 MHz and 1.4 GHz.

We first measure the spectral indices of the giant lobes over the same regions as Hardcastle et al. (2009) using T-T plots. This technique accounts for the possibility of constant offsets between maps due to missing short spacings or large-scale foreground contamination. T-T plots were initially used in the analysis of astronomical observations to account for a constant but unknown component of antenna temperature being contributed by the ground in observations of the spectrum of Galactic radio emission (Turtle et al. 1962). The technique takes the brightness temperature of many points within a region of the sky (assumed to have the same spectral index) at two different frequencies and plots them against each other. If there is a constant offset between the brightness temperature values within a region due

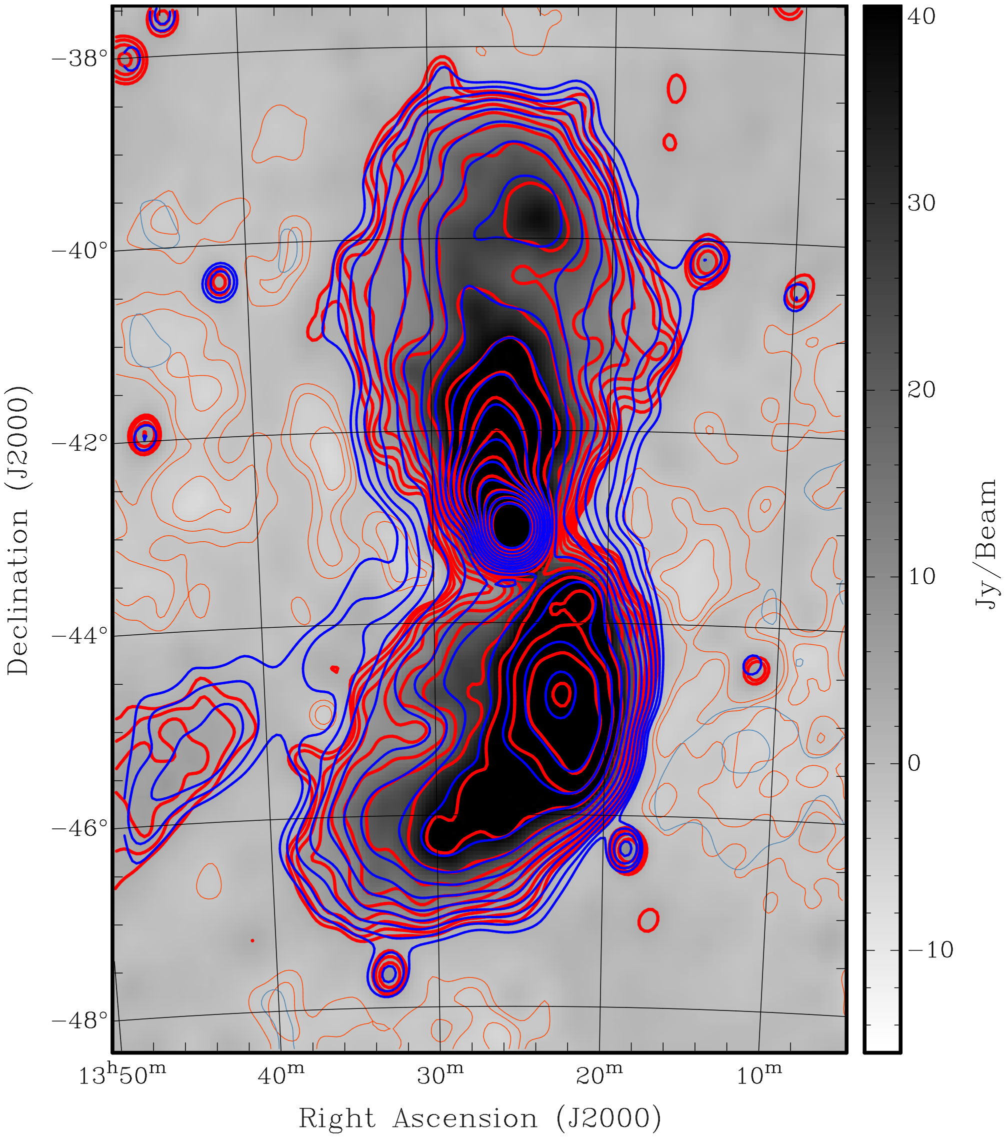

Figure 3.6 Cen A at 118 MHz (gray scale and red contours) overlaid with Parkes 1.4 GHz contours in blue, smoothed to the same angular resolution of 25 arcmin. Positive contours are bold and start at 2.5 Jy/beam for 118 MHz and 0.50 Jy/beam for 1.4 GHz, incrementing in a geometric progression of $\sqrt{2}$. Negative contours (thinner and lighter shade) start at -2.5 Jy/beam for 118 MHz and -0.50 Jy/beam for 1.4 GHz and decrement in a geometric progression of $\sqrt{2}$.

to emission from the ground (or any other reason) then this will be obvious in a T-T plot; the points in a T-T plot between frequencies ν_1 and ν_2 will fall along a line having a slope equal to $(\nu_1/\nu_2)^\alpha$, and with a non-zero y-intercept resulting from the constant offset between the two regions. At 118 MHz, the brightness temperature of the Galactic foreground is two orders of magnitude higher than at 1.4 GHz and if significant on the spatial scales of our chosen regions, it would show up as a constant offset in T-T plots between 118 MHz and 1.4 GHz. The effects of missing flux due to missing short baselines in the interferometer data would also cause a constant offset in the T-T plots.

We constructed T-T plots for the five regions shown in Fig. 3.7, chosen to match with the regions defined by Hardcastle et al. (2009). Our region 3 differs from Hardcastle et al. (2009) in that we use a rectangle, rather than a circle, to define this region. The 1.4 GHz images were smoothed to the same 25-arcmin resolution as the MWA map (Fig. 3.3) and both images were resampled to make the pixel size as large as the synthesized beam. This produced independent measurements of the flux density at each (equally sized) pixel in both images, allowing us to perform a chi-squared analysis. For each region, the flux densities at the low and the high frequencies at each pixel were plotted against each other. The error bars for each point were estimated by selecting off-source regions to the east and west of each of the regions in Fig. 3.7 and measuring the rms noise in each. These off-source regions were large enough to ensure that the rms measurement included both variations in Galactic foreground emission and the contribution of background point sources. The reduced chi-squared (χ^2_{red}) was also computed for each T-T plot and used as an indicator of the validity of the assumption of a single spectral index over the spatial extent of a given region. A line was fit to the data using orthogonal-distance regression (Boggs & Rogers 1990) and the spectral index for each region, α_R, was calculated using:

$$\alpha_R = \frac{\log(\Delta)}{\log(\nu_{low}/\nu_{high})}, \tag{3.1}$$

where Δ is the slope of the line of best fit for the T-T plot of region R and ν_{low} and ν_{high} are the low and high frequencies, respectively.

Fig. 3.8 shows T-T plots for the five regions of the giant lobes and the computed values of α and χ^2_{red} for each. The centre row of Fig. 3.8 contains two plots for region 3; on the left all pixels have been included, and on the right the bright central pixel has been excluded to remove the influence of the inner lobes, since we are primarily concerned with the spectral indices of the giant outer lobes in this paper. The χ^2_{red} values for regions 2 and 5, corresponding to the inner part of the northern outer lobe and the outer part of the southern outer lobe, respectively, are close to unity, indicating that the spectral indices of

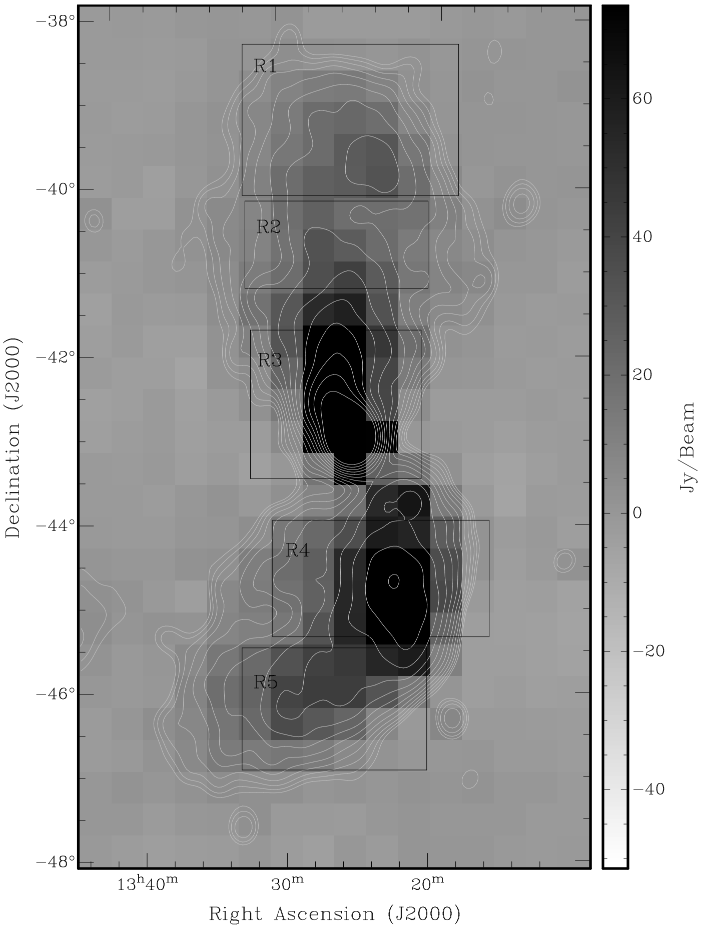

Figure 3.7 Regions from Hardcastle et al. (2009) used for constructing T-T plots, overlaid on the MWA 118 MHz image resampled to 1 pixel per beam. Contours are of the full resolution 118 MHz image, incrementing in a geometric progression of $\sqrt{2}$ from 2.5 Jy/beam.

these regions show little spatial variation. The T-T plots for region 3 have χ^2_{red} values of 56.0, if the central pixel is included, and 42.1, if the central pixel is excluded. These χ^2_{red} values are an order of magnitude larger than for the other regions, indicating significant spatial variation of the spectral index. This is probably due to the complex structure of the region that contains the NML. Regions 1 and 4 were also found to have high χ^2_{red} values of 2.7 and 3.6, respectively. The variation in spectral index in these regions will be investigated in detail using spectral tomography in Section 4.1.1.

The spectral indices derived from the T-T plots can be considered as averages over each region and so can be compared to the values computed using summed flux densities in previous studies. The main source of error in the spectral indices is due to the 22% uncertainty of the global flux scale in the MWA 118 MHz image. This error does not affect differences in the spectral indices computed between regions. We therefore quote separately the systematic errors due to global flux scale uncertainties and the statistical errors due to random errors in the images. The error in the flux scale of the 1.4 GHz

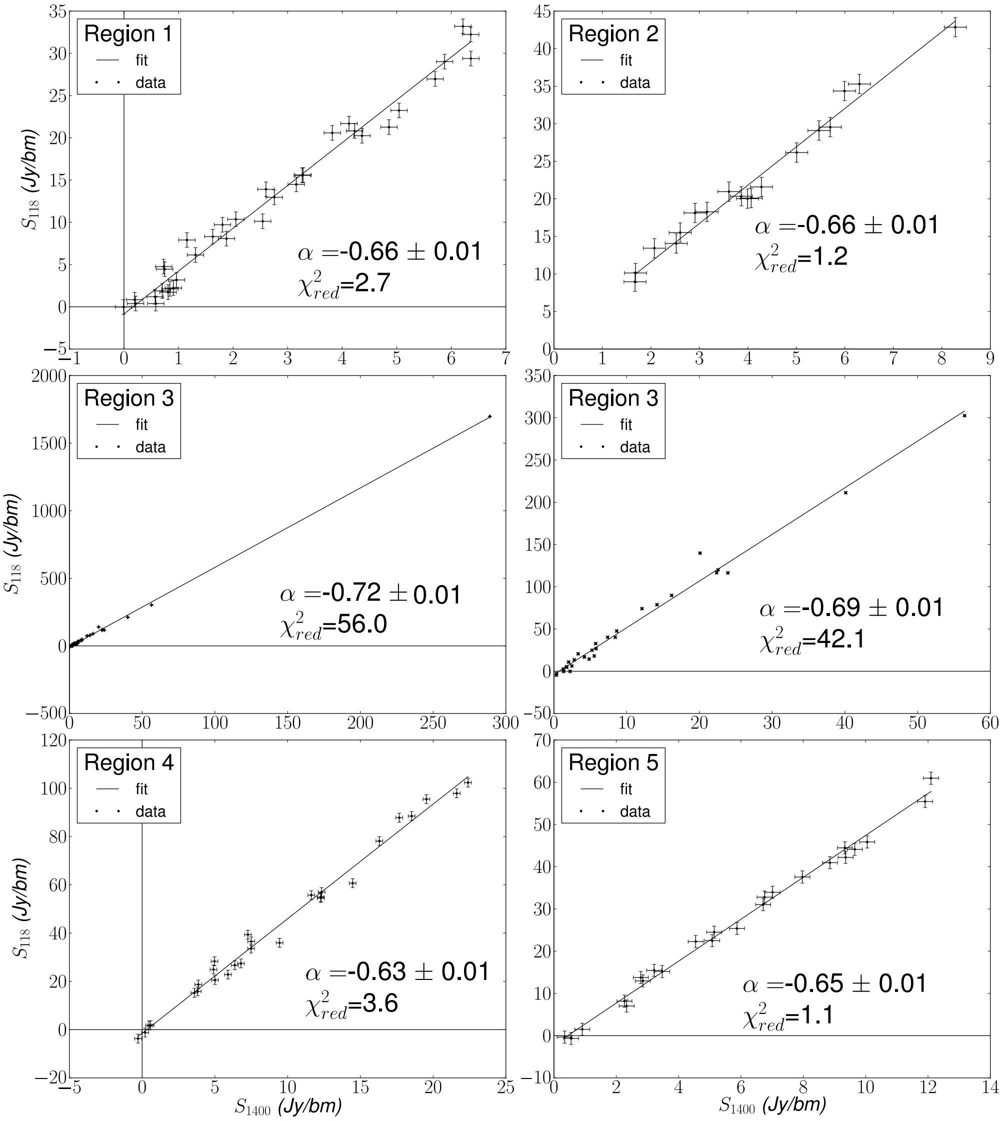

Figure 3.8 T-T plots for the five regions of the giant lobes of Cen A and the computed spectral indices between 118 and 1400 MHz, including the χ^2_{red} values for each region as defined in Fig. 3.7. The centre row contains two plots for region 3; on the left all pixels have been included, and on the right the bright central pixel has been excluded to remove the influence of the inner lobes. The uncertainties in the spectral indices displayed are derived from the uncertainty in the slope of the line of best fit and represent random errors only. See text for the inclusion of systematic errors due to global flux scale uncertainties.

data is approximately 2% (Reynolds 1994; Baars et al. 1977) and is negligible compared to the uncertainty at 118 MHz. We find a spectral index in regions 1 and 2 (northern outer lobe) of $\alpha_{1,2} = -0.66 \pm 0.01(\mathrm{stat})^{+0.10_{\mathrm{sys}}}_{-0.08_{\mathrm{sys}}}$, and in regions 4 and 5 (southern outer lobe) of $\alpha_4 = -0.63 \pm 0.01(\mathrm{stat})^{+0.10_{\mathrm{sys}}}_{-0.08_{\mathrm{sys}}}$ and $\alpha_5 = -0.65 \pm 0.01(\mathrm{stat})^{+0.10_{\mathrm{sys}}}_{-0.08_{\mathrm{sys}}}$, respectively. The calculated spectral-index values are consistent with Alvarez et al. (2000), who found the spectral indices of the northern and southern lobes between 408 MHz and 1.4 GHz to be -0.75 ± 0.08 and -0.70 ± 0.08, respectively. Our values are also consistent with the Hardcastle et al. (2009) spectral indices between 408 MHz and 1.4 GHz (which we calculated from the flux density values in their Table 1) of $\alpha_1 = -0.60 \pm 0.05$ and $\alpha_2 = -0.65 \pm 0.07$ in the northern lobe and $\alpha_4 = -0.47 \pm 0.06$ and $\alpha_5 = -0.62^{+0.12}_{-0.11}$ in the southern lobe.

As well as being averages across a given angular region, the spectral indices computed using T-T plots are averages along our line of sight. This presents a problem if there are overlapping regions with different spectral indices. In a scenario where the lobes were formed by multiple, separate outbursts from the central engine (Morganti et al. 1999; Saxton et al. 2001), there could be overlapping structures of synchrotron-emitting particles produced during different epochs of activity, as discovered in another relatively close-by radio galaxy Hercules A (Gizani & Leahy 2003). In this case, the restarted jets forming the more recent lobe structures have a faster advance speed than the previous jets since they are travelling through an underdense region that has been cleared of material in the previous epoch of activity (Clarke & Burns 1991). As the new lobes catch up to the older lobes, this results in particles with different spectral ages (and presumably different spectral indices) overlapping along our line of sight. To investigate this possibility further we apply the technique of spectral tomography in Section 4.1.1.

Spectral Tomography

The simple two-point spectral index generated by dividing images at different frequencies is unable to separate structures with different spectral indices when they are aligned along our line of sight, instead giving a weighted average of the two. Spectral tomography has been used to identify overlapping spectral structures within radio galaxies (Katz-Stone & Rudnick 1997; Gizani & Leahy 2003) and has also been applied to Galactic sources (DeLaney et al. 2002; Gaensler & Wallace 2003). Here we apply the technique to the giant lobes of Cen A to search for regions with distinctly different spectral indices, which may overlap along our line of sight and therefore may be difficult to detect using conventional methods.

Since the spectral index of each component is not known, a cube of images is generated, each with a different spectral component subtracted away. The cube of images, $M_{tom}(\alpha_t)$, is given mathematically by

$$M_{tom}(\alpha_t) \equiv M_{low} - \left(\frac{\nu_{low}}{\nu_{hi}}\right)^{\alpha_t} M_{hi}, \tag{3.2}$$

where M_{low} and M_{hi} are the low and high-frequency maps, ν_{low} and ν_{hi} are the low and high frequencies, respectively, and α_t is the trial spectral index for that image in the cube.

When the trial spectral index is correct, the component is subtracted perfectly and the region of the image appears to match with the background. Whenever the trial index is incorrect, the component is either under-subtracted or over-subtracted, making it appear lighter or darker than the background. The uncertainty in the spectral index is determined by the range of trial values in which a feature on the map is neither under-subtracted nor over-subtracted. The uncertainties quoted in this section are therefore due to random errors only and do not include the systematic error introduced by the uncertainty in the global flux scale. We generated a spectral tomography cube with trial spectral indices from -0.01 to -1.50, decrementing in steps of 0.01. When the tomography cube is viewed as a movie, it is clear that there are variations in spectral index with position across both the northern and southern outer lobes of Cen A. We show a subset of the images from the cube in Figs 3.9 and 3.10.

First we examine the northern lobe, and in particular region 1 where the χ^2_{red} of the T-T plot indicated that a power law with a single spectral index for the whole region was not a good model (see Fig. 3.8). A series of six slices of the tomography cube is shown in Fig. 3.9, with trial spectral indices from $\alpha_t = -0.45$ to $\alpha_t = -0.70$, decrementing in steps of 0.05. The spectral tomography reveals that the spatial distribution of spectral-index values is complex, and although the average value of around -0.65 (lower, centre panel) agrees well with the T-T plots, it is clear that there are a range of spectral-index values distributed across region 1 and across the rest of the northern lobe. In particular, the spectral index flattens significantly at a declination of around $-39\overset{\circ}{.}5$ (label A) where the position angle of the northern lobe changes to form the outer northern-hook structure. From the tomography cube, we estimate that the spectral index of this flattened region is -0.55 ± 0.05 and steepens to -0.70 ± 0.05 at the end of the northern hook (label B). An interesting result is that a similar positional change in spectral index also occurs in the region closer to the core. Immediately south of declination -42° there is a relatively flat region of spectral index -0.67 ± 0.01 (label D) which abruptly steepens to -0.72 ± 0.01 north of declination -42° (label C). These features are most clearly seen where they are slightly over-subtracted or under-subtracted, hence the reason for showing slices at $\alpha_t = -0.65$ and $\alpha_t = -0.70$ in Fig. 3.9, rather than $\alpha_t = -0.67$ and

$\alpha_t = -0.72$. There is also a distinctly steeper region at $13^{\mathrm{h}}31^{\mathrm{m}}18^{\mathrm{s}}$, $-41°19'54''$; however this is not a feature of the lobes of Cen A. It is due to the background point source PKS 1328-410 (Large et al. 1981), which can also be seen clearly in the high-resolution map of Feain et al. (2011).

A subset of the spectral tomography cube zoomed in on the southern outer lobe is shown in Fig. 3.10. Although the large-scale morphology is quite different from the northern lobe, we do see similar changes in spectral index with position in the south. This is most prevalent in the northern region of the southern lobe (corresponding to region 4 in the T-T plots in Fig. 3.8). Of interest is the distinctly steeper region at approximately Dec (J2000) $-43°45'$ (label E) with a spectral index of -0.69 ± 0.02 surrounded by regions of spectral index -0.57 ± 0.02 immediately to the north and south (label F). This is best seen in the lower-left panel ($\alpha_t = -0.59$) of Fig. 3.10, where the steeper feature is under subtracted, appearing darker than the flatter-spectrum region surrounding it. The feature labelled E in Fig. 3.10 appears to be present at 118 MHz but not at 1.4 GHz. To exclude the possibility that this could be due to a bright, steep-spectrum background point source, we have plotted in Fig. 3.11 the MWA and Parkes contours over the high-resolution ATCA+Parkes map of Feain et al. (2011). Fig. 3.11 shows that the additional peak at RA (J2000) $13^{\mathrm{h}}23^{\mathrm{m}}$, Dec (J2000) $-43°51'$ in the 118 MHz map does not coincide with any background sources visible at 1.4 GHz. The bright extended source MRC 1318-434B (Schilizzi & McAdam 1975; Large et al. 1981) is clearly visible in the high resolution gray-scale image and is largely responsible for the peak in the contours of the smoothed 118 MHz and 1.4 GHz images at RA (J2000) $13^{\mathrm{h}}21^{\mathrm{m}}$, Dec (J2000) $-43°48'$, which is approximately 30 arcmin away from the additional peak in the 118 MHz image. The positional registration of the two images is accurate to within 1 arcmin. Two other steep spectrum features that are prominent in Fig. 3.10 at RA (J2000) $13^{\mathrm{h}}29^{\mathrm{m}}38^{\mathrm{s}}$, Dec (J2000) $-44°44'14''$ and RA (J2000) $13^{\mathrm{h}}33^{\mathrm{m}}57^{\mathrm{s}}$, Dec (J2000) $-46°41'32''$ are due to the background point sources SUMSS J132937-444413 (Mauch et al. 2003) and PMNM 133051.5-462614 (Large et al. 1981), respectively. Again, these bright background sources are clearly visible in the high resolution map of Feain et al. (2011).

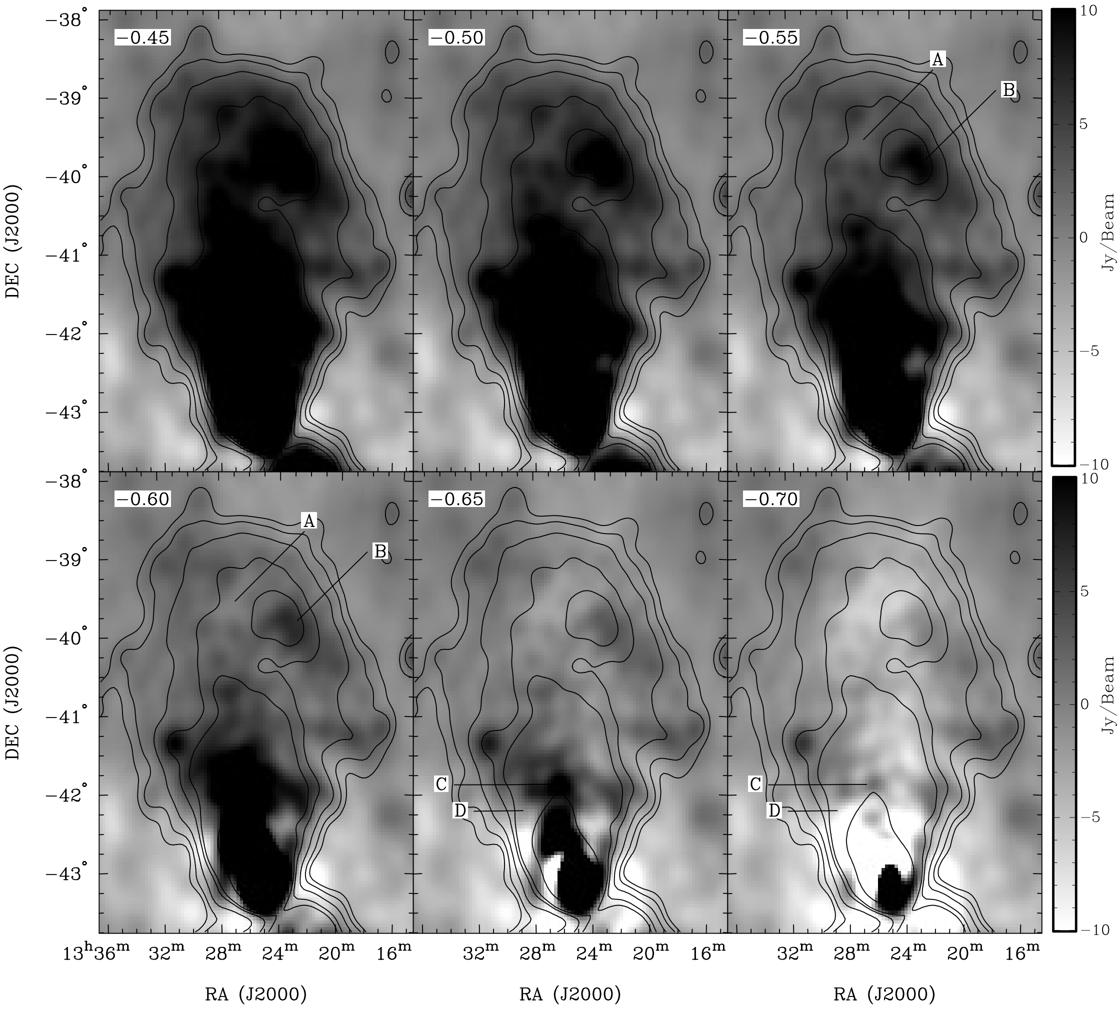

Figure 3.9 A subset of the spectral tomography images of the northern lobe between 118 MHz and 1.4 GHz with trial spectral indices as indicated in the top-left corner of each sub-image. Gray scale is from -10 to 10 Jy/beam. Overlaid are contours from the 118 MHz image at 2.5, 5, 10, 20, 28.3 and 113 Jy/beam. The feature labelled A has a significantly flatter spectral index than that labelled B. Similarly, there is a change in spectral index between the flatter region labelled D and the steeper feature labelled C.

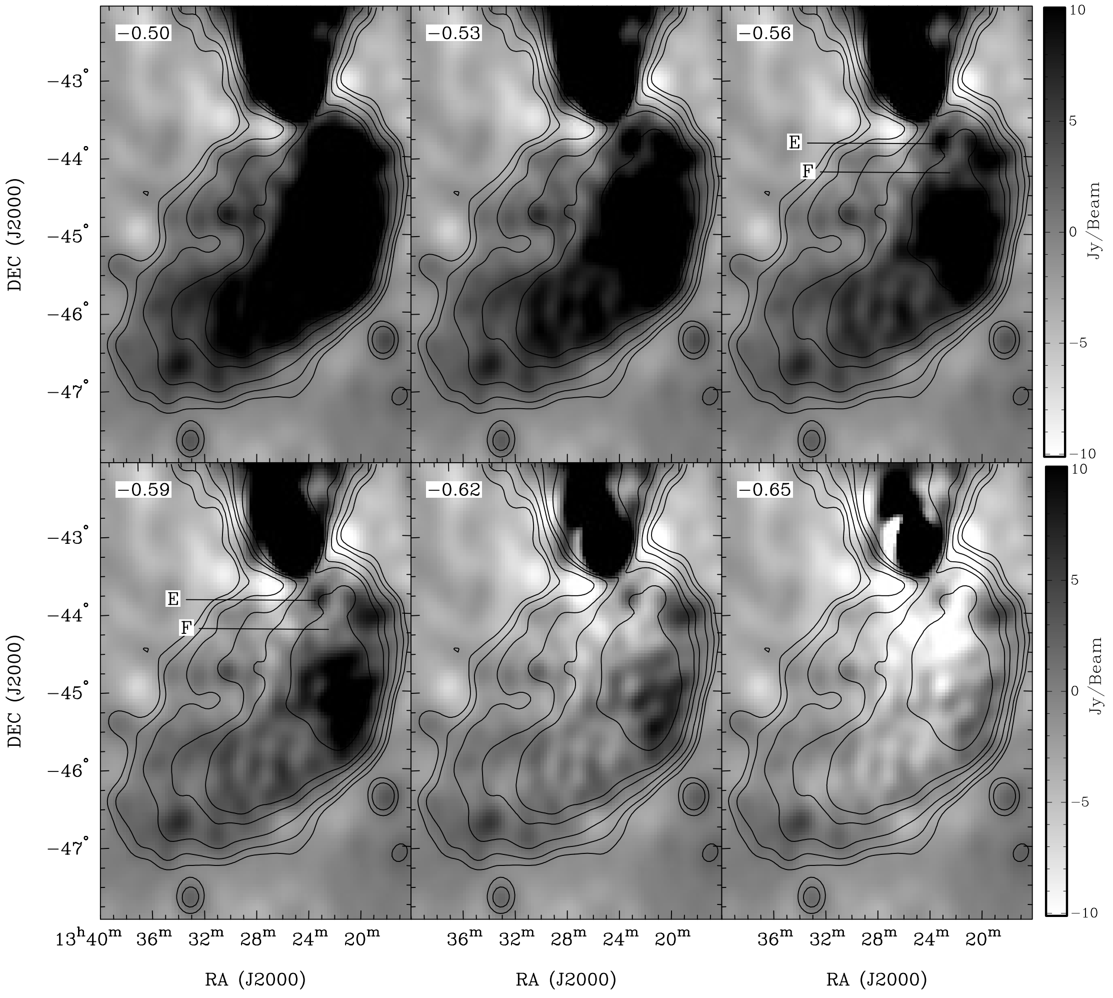

Figure 3.10 As for Fig. 3.9, but for the southern lobe with contours from the 118 MHz image at 2.5, 5, 10, 20, 28.3 and 56.5 Jy/beam. The feature labelled E has a significantly steeper spectral index than that labelled F.

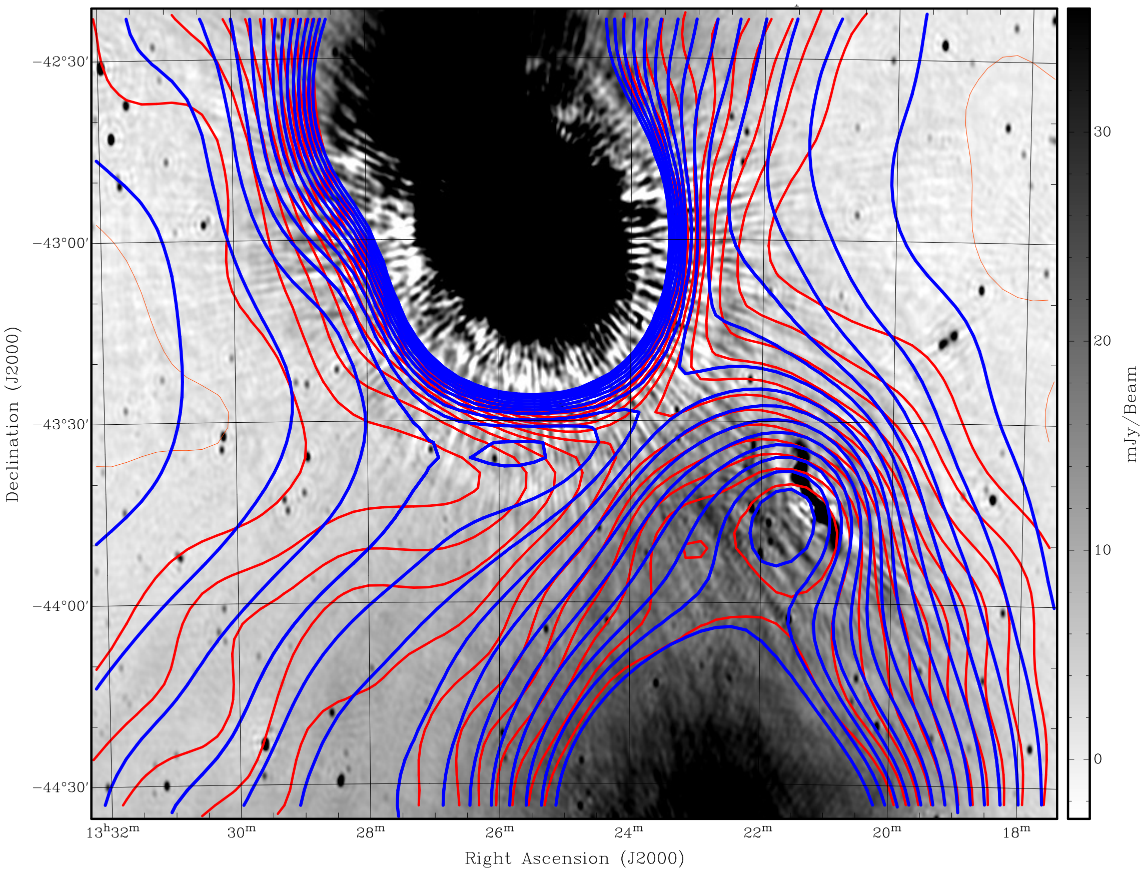

Figure 3.11 High resolution 1.4 GHz Parkes+ATCA map (Feain et al. 2011) in gray scale, overlaid with the 1.4 GHz Parkes contours (O'Sullivan et al. 2013) in blue and the MWA 118 MHz contours in red. Positive 118 MHz MWA contours are from 3 Jy/beam incrementing in steps of 5 Jy/beam and 1.4 GHz Parkes contours are from 1 Jy/beam incrementing in steps of 1 Jy/beam. There is one negative contour visible, which is the −3 Jy/beam level of the 118 MHz map, shown as a thinner, lighter red line. There is a peak at $13^{h}23^{m}$, −43°51′ in the 118 MHz map that is not visible in the 1.4 GHz images and does not coincide with any background sources visible at 1.4 GHz. The bright background source MRC 1318-434B, at $13^{h}21^{m}18^{s}$, −43°41′15″, extends approximately 20 arcmin and is coincidentally aligned with the position angle of the inner lobes of Cen A.

3.6. Discussion

3.6.1. Morphology, spectral index and clues about lobe formation history

The morphology of Cen A at 118 MHz with 25-arcmin resolution matches closely with the single dish Parkes observations at 1.4 GHz, as shown in Fig. 3.6. The 15 arcmin gap between the northern and southern lobes reported by Feain et al. (2011) can also be seen in the 118 MHz image, although in the latter data the emission does not quite disappear down to the noise level, since the synthesized beam of 25 arcmin is too large to fully resolve this feature. The difference in the large-scale morphologies between the northern and southern lobes is quite distinct, with the northern lobe characterized by an abrupt change in position angle producing the northern hook feature and the southern lobe having a much smoother variation in orientation. These large-scale features mirror the morphology of the inner lobes as imaged at high spatial resolution with the Very Large Array (Schreier et al. 1981; Clarke et al. 1992). In the north, a sudden change in position angle of the radio emission is also seen at an intermediate scale in the NML, as imaged in detail by Morganti et al. (1999) (see e.g., their fig. 4). An explanation for the existence of the intermediate scale NML and the fact that it mirrors the shape of the inner lobes was proposed by Morganti et al. (1999), who suggested that the central engine has undergone multiple outbursts of activity. In this scenario, the inner lobes are due to the most recent outburst and the middle and outer lobes are relics of past activity. They suggest that the distinctive shape of the NML and its associated large-scale jet could be due to a similar type of interaction with the surrounding environment that produces the class of radio galaxies known as wide-angled tailed (WAT) radio galaxies. Norman et al. (1988) used numerical simulations of jets disrupted by shocks in the ambient medium to reproduce the structure of WATs and the inner northern jet of Cen A. If the inner lobes are the result of the current outburst of activity from the core and the NML is the result of a previous outburst, then the outer northern lobe with its hook-like structure seen at frequencies below 5 GHz is probably the result of similar previous outbursts of AGN activity. In order to build up such large, energetic structures as the giant outer lobes, many outbursts similar to the current inner lobe activity are likely to have been required.

Clear evidence of multiple, separate outbursts of activity in radio galaxies is seen in the class of radio galaxies known as ‘double-double’ radio galaxies (see e.g., Schoenmakers et al. 2000; Jamrozy et al. 2009). However, these are characterized by edge-brightened lobes like those seen in FRII galaxies. Jamrozy et al. (2009) single out several other radio galaxies that show evidence of multiple outbursts of activity including 3CR310 (Leahy et al. 1986), the WAT galaxy in the cluster A 2372 (Giacintucci et al. 2007), Hercules A (Her A, Gizani & Leahy 2003) and also Cen A. Spectral-index maps of the WAT galaxy in A 2372 and Her A show similar features to our spectral-tomography results, where the spectral index changes with distance from the core, showing alternating regions of flatter and steeper spectral index indicating different spectral ages across the lobes. In our spectral-tomography results for the northern lobe of Cen A (Fig. 3.9), we show that the spectral index steepens along the extended structure associated with NML from point D to point C, indicating an older population of particles further from the core. The spectrum then flattens again at point A, which could be due to reacceleration of particles in this region, caused by interaction with newer, more energetic particles from the outburst that created the NML. The new material catches up to the old lobes as it has a less dense medium to travel through, as shown in numerical simulations by Clarke & Burns (1991). Finally, the spectrum steepens again at the end of the northern hook (point B in Fig. 3.9); this could indicate an older population of particles that has not experienced reacceleration, possibly because the central engine has precessed and the subsequent outbursts are not directed towards this region. The spectral variations we observe in Cen A, however, are relatively subtle. In most cases $\Delta\alpha_{118}^{1400} < 0.1$, while in Her A $\Delta\alpha_{1300}^{4800} \approx 0.8$ between the bridge and the jet and ring features (Gizani & Leahy 2003). While some of the difference in magnitude of the spectral variation can be attributed to the lower frequency of the Cen A spectral-index measurement, it is possible that variations in the magnetic field strength or the initial jet spectrum may be enough to cause such variations without the need for reacceleration.

The structure of Cen A is complicated by the bending of the lobes, which is probably due to both the interaction with the ambient medium (Morganti et al. 1999), at least for the northern lobe, and the precession or reorientation of the central engine over time (Haynes et al. 1983). The radio morphology of Cen A at small, intermediate and large scales supports the multiple-outburst scenario described above, where there appear to have been three epochs of activity that formed the inner, middle and outer lobes, respectively. However, the detailed timing of these outbursts of activity is difficult to determine and remains unclear. Hardcastle et al. (2009) calculate spectral ages of ~30 Myr for the outer lobes of Cen A and Haynes et al. (1983) calculate a precession rate for the central engine of 1×10^{-5} deg yr^{-1} from the stellar ages of observed B supergiants near the NML (Osmer 1978). This implies that over the time of formation of the outer lobes, there were several precessional periods of the central engine and also time for several outbursts of activity on similar scales to that which formed the inner lobes, which have an estimated spectral age of ~ 5 Myr (Burns et al. 1983). In a separate analysis, Wykes et al. (2013) estimate much greater ages for the giant lobes of 440 to 645 Myr and 560 Myr (for both lobes) based on dynamical and buoyancy arguments respectively, which would allow time for many more outbursts of activity and precessional periods. Wykes et al. (2013), however, recognize that their age estimates differ from ages derived by radio spectral index information by a large amount and we note that the arguments they base their calculations on are known to overestimate lobe ages in radio galaxies as detailed in McNamara & Nulsen (2007).

Alvarez et al. (2000) discuss the relationship between the break frequency in the lobes of Cen A and their spectral ages, and use their equation 1 (following Perola 1981) to calculate spectral ages for the lobes, based on their lower limit on the break frequency of 4.75 GHz, and find the lobe spectral ages to be less than 28 Myr. The SED fitting of Hardcastle et al. (2009), over a wider frequency range, reveals a break frequency in the lobes of around 6 GHz (corresponding to similar spectral ages of around 30 Myr). If the lobe ages Wykes et al. (2013) were also the spectral ages of the lobes then the inferred break frequency from Alvarez et al. (2000), equation 1, would be on the order 10 MHz, which is clearly ruled out by the observations. If the dynamical ages estimated by Wykes et al. (2013) do, however, represent the actual time since the formation of the lobes, then the large discrepancy between these dynamical ages and the spectral ages estimated by Hardcastle et al. (2009) and Alvarez et al. (2000) could be attributed to ongoing reacceleration of the relativistic particles in the lobes (Wykes et al. 2013).

A problem with the multiple-outburst scenario is the apparent non-existence of a southern counterpart to the NML. Our 118 MHz map and spectral-tomography results do however indicate the existence of a steeper spectrum component along the southern lobe (see Figs 3.10 and 3.11) at a location that is at approximately the correct position angle to be associated with the same period of activity as the NML. Whether this is evidence for the existence of a faint, steep spectrum feature associated with a 'southern middle lobe' will be investigated through future observations with the full 128-tile MWA, which will provide higher angular resolution and increased sensitivity to such diffuse radio structures.

3.6.2. Comparison to gamma-ray data

Yang et al. (2012) model the SEDs of the northern and southern lobes of Cen A using gamma-ray observations from Fermi-LAT and radio data from ground-based telescopes (see Hardcastle et al. 2009) and WMAP (Hinshaw et al. 2009; Komatsu et al. 2011). They present SEDs from inverse-Compton models, which predict the flux density of the radio emission at low frequencies, integrated over the entire gamma-ray emitting region of the lobes. Figs 8 and 9 of Yang et al. (2012) show SEDs for two values of the model age of the outer lobes, t, selected based on the approximate lower limit of the lobe ages of 10^7 years, set by dynamical arguments and the modelling of Hardcastle et al. (2009), and an upper limit of 10^8 years, supported by the GeV data in the Yang et al. (2012) paper itself. We calculated the predicted two-point flux-density spectral index between 118 MHz and 1.4 GHz for both of the Yang et al. (2012) models, from the flux and frequency values read from their figs 8 and 9. For a lobe age of 10 Myr the predicted spectral index in both the northern and southern lobes is approximately -0.62 and for a lobe age of 80 Myr the predicted spectral index in both lobes is -0.57. Our values for the average spectral indices of the lobes as derived from the T-T plots (Fig. 3.8) of $\alpha_{1,2} = -0.66 \pm 0.01(\mathrm{stat})^{+0.10_{\mathrm{sys}}}_{-0.08_{\mathrm{sys}}}$ in the northern lobe and $\alpha_4 = -0.63 \pm 0.01(\mathrm{stat})^{+0.10_{\mathrm{sys}}}_{-0.08_{\mathrm{sys}}}$ and $\alpha_5 = -0.65 \pm 0.01(\mathrm{stat})^{+0.10_{\mathrm{sys}}}_{-0.08_{\mathrm{sys}}}$ in the southern lobe, are consistent with both of these predictions. The difference between the predicted spectral indices is too small for us to distinguish between the lobe ages from our measured spectral indices and in any case the modelling of Yang et al. (2012) can only be considered a first-order approximation to the true physical conditions. Assumptions such as a single age and spectral index for the lobes, a constant magnetic field and constant particle densities have been shown to be untrue (see e.g., Junkes et al. 1993; Feain et al. 2011, this work) therefore more detailed theoretical models are needed to take full advantage of current and future observational data.

3.7. Conclusion

We have imaged the entirety of Cen A and a large surrounding field at 118 MHz with the MWA 32T. The wide field of view and good uv-coverage of the MWA 32T allow us to map the giant lobes at a reasonable angular resolution and to reconstruct their large-scale structure. We have investigated the spatially-resolved spectral properties of the giant lobes by comparing the MWA map at 118 MHz to Parkes data at 1.4 GHz. Through the use of T-T plots and spectral tomography, we find that the spectral index of the lobes between 118 MHz and 1.4 GHz has a spatially-averaged value consistent with measurements at other frequencies, but that there is a complex spatial distribution of spectral index across the lobes. The morphology and spectral-index distribution of the lobes support a scenario of multiple outbursts from a precessing central engine, and we find tentative evidence for the existence of a faint, steep spectrum southern counterpart to the NML. We find that our results also agree well with the inverse-Compton modelling of gamma-ray and radio data. Future observations with the complete 128-tile MWA will provide a more detailed picture of the low-frequency properties of Cen A, which can be used to constrain more complex theoretical models.

CHAPTER 4

Modelling of the Spectral Energy Distribution of Fornax A: Leptonic and Hadronic Production of High Energy Emission from the Radio Lobes

This chapter has been submitted to MNRAS as 'Modelling of the Spectral Energy Distribution of Fornax A: Leptonic and Hadronic Production of High Energy Emission from the Radio Lobes', McKinley, B., Yang, R., López-Caniego, M., et al., 2014, MNRAS submitted.

4.1. Abstract

We present new low-frequency observations of the nearby radio galaxy Fornax A at 154 MHz with the Murchison Widefield Array, microwave flux-density measurements obtained from *WMAP* and *Planck* data, and γ-ray flux densities obtained from *Fermi* data. We also compile a comprehensive list of previously published images and flux-density measurements at radio, microwave and X-ray energies. A detailed analysis of the spectrum of the radio lobes between 154 MHz and 1510 MHz reveals that both radio lobes have a similar spatially-averaged spectral index. Taking the spectral index of both lobes to be the same, we model the spectral energy distribution of Fornax A across an energy range spanning eighteen

orders of magnitude, to investigate the origin of the X-ray and γ-ray emission. A standard leptonic model for the production of both the X-rays and γ-rays by inverse-Compton scattering does not fit the multi-wavelength observations. Our results best support a scenario where the X-rays are produced by inverse-Compton scattering and the γ-rays are produced primarily by hadronic processes confined to the filamentary structures of the Fornax A lobes.

4.2. Introduction

A number of radio galaxies have been shown to have associated γ-ray emission (Nolan et al. 2012). In the case of the nearest radio galaxy, Centaurus A, *Fermi* Large Area Telescope (*Fermi*-LAT; Atwood et al. 2009) observations revealed that the γ-rays originate predominantly in the extended radio lobes (Abdo et al. 2010a), rather than the central active galactic nucleus (AGN). The mechanism for producing these γ-rays was interpreted by Abdo et al. (2010a) as inverse-Compton (IC) radiation from the up-scattering of cosmic microwave background (CMB) and extragalactic background light (EBL) photons by relativistic electrons. Using a larger *Fermi*-LAT data set, Yang et al. (2012) found that a contribution from proton interactions in the lobe plasma could also account for the shape of the spectral energy distribution (SED) of the Centaurus A lobes. Further observational and theoretical investigation into the origin of the γ-ray emission from the lobes of radio galaxies is required to determine the relative contributions of the physical mechanisms responsible.

In the IC scattering model of γ-ray production, we assume that a single population of highly relativistic electrons, with a power-law energy distribution, is responsible for up-scattering seed photons (the most abundant of which are CMB photons) to higher energies. The power-law energy distribution of the electrons results in a power-law spectrum of the synchrotron emission such that the flux density, S_ν, is given by $S_\nu \propto \nu^{\alpha_r}$, where ν is frequency and α_r is the radio spectral index. The power-law energy distribution of electrons also results in an IC emission spectrum at higher energies that has the same spectral shape as the synchrotron spectrum. The electron energy index, p, which characterizes the shape of the underlying electron energy distribution, is given by $p = 2\alpha_r + 1$.

In the hadronic scenario for the production of γ-rays in radio galaxy lobes, nonthermal cosmic-ray protons produce mesons through proton-proton (p-p) collisions and γ-rays result from the decay of the neutral pion component. This mechanism has been proposed as an explanation for the γ-ray emission observed in the so-called *Fermi* bubbles of our own

Galaxy (Crocker & Aharonian 2011; Crocker et al. 2013).

Fornax A was the first radio galaxy shown to emit X-ray IC radiation resulting from the up-scattering of CMB photons by relativistic, synchrotron-emitting electrons in its lobes (Laurent-Muehleisen et al. 1994; Feigelson et al. 1995) and has also been detected as a γ-ray point source by *Fermi* (Nolan et al. 2012).The host galaxy is the elliptical NGC 1316, which lies at a distance of 18.6 Mpc (Madore et al. 1999).

In this paper we investigate the origin of the Fornax A γ-rays through a detailed analysis of the synchrotron emission in the lobes and broadband SED modelling using a combination of new low-frequency data from the Murchison Widefield Array (MWA; Lonsdale et al 2009; Tingay et al. 2013; Bowman et al. 2013), microwave data from *Planck* (Tauber et al. 2010; *Planck* Collaboration 2013) and *WMAP* (Bennett et al. 2003a,b), γ-ray data from *Fermi*-LAT and previously published data from a range of ground and space-based telescopes. In Section 2, we discuss previous observations and analyses of the Fornax A radio lobes. In Section 3, we provide details of the new observations and data reduction procedures and describe the previously published data used. In Section 4, we present a spatially resolved analysis of the low-frequency spectral index of the lobes of Fornax A. We then fit the multi-wavelength data, using different emission models, to investigate various scenarios for the production of both the X-ray and γ-ray photons. We discuss the results of our analyses in Section 5.

4.3. Previous radio observations and analyses of For A

Fornax A was one of the earliest identified extragalactic radio sources (Mills 1954). The flux density of the entire source has been measured over a wide range of radio frequencies, from 5 MHz (Ellis & Hamilton 1966) to 5 GHz (Gardner & Whiteoak 1971). However, low-frequency observations (below 400 MHz) lacked the angular resolution required to resolve the two radio lobes and were also unable to resolve the fainter, compact core, which is clearly evident in the higher-frequency images (e.g. Fomalont et al. 1989) and in this work.

Bernardi et al. (2013) examined the radio spectrum of Fornax A between 5 and 1415 MHz using previously published data and measured the total flux density of Fornax A using the MWA 32-tile prototype. By fitting a power-law spectrum to the measurements between 30 and 400 MHz (excluding two data points at 100 MHz and one point at 400 MHz, which appeared to be affected by systematic errors) they calculated a spectral index of -0.88 ± 0.05. Their measured total flux density was 519 ± 26 Jy at 189 MHz. The MWA Commissioning

Survey (MWACS; Hurley-Walker et al. 2014) has also measured the flux density of Fornax A with sub-array configurations of the MWA during science commissioning. Since the sub-arrays had insufficient short spacings to fully sample the large-scale structure of Fornax A, they quote lower limits on the flux densities, which are > 786, > 668 and > 514 Jy at 120, 150 and 180 MHz, respectively.

There have been several confirmations of the X-ray IC emission from the lobes of Fornax A, since the work of Laurent-Muehleisen et al. (1994) and Feigelson et al. (1995). Kaneda et al. (1995) observed IC X-rays in the lobes of Fornax A and compared their measurements to previously-published radio data to estimate a magnetic field strength in the lobes of 2-4 μG. In their analysis, they derived a radio spectral index for the entire source of $\alpha_r = -0.9 \pm 0.2$ from three published data points at 408 MHz (Cameron 1971), 1.4 GHz (Ekers et al. 1983) and 2.7 GHz (Shimmins 1971). Subsequently, Isobe et al. (2006), using X-ray data on the east lobe of Fornax A from *XMM-Newton*, improved on the IC analysis by using a more comprehensive set of published radio data. They obtained a radio spectral index, again using data for the entire source, of $\alpha_r = -0.68 \pm 0.10$ and used this value to derive the physical quantities of the lobes.

Tashiro et al. (2009) performed an updated IC analysis, this time on the west lobe and going to a higher X-ray energy of 20 keV. The higher X-ray energy means that the same population of electrons (in terms of energy) is being sampled in both the synchrotron (radio) and IC (X-ray) measurements. Tashiro et al. (2009) also fixed the radio spectral index at -0.68, as derived by Isobe et al. (2006), when fitting the SED and deriving the physical quantities of the lobes. Isobe et al. (2006) and Tashiro et al. (2009) also report best-fit X-ray spectral indices of $-0.62^{+0.15}_{-0.24}$ (Isobe et al. 2006) and -0.81 ± 0.22 (Tashiro et al. 2009) for the east and west lobes, respectively. The X-ray spectral indices for both lobes are consistent with the radio spectral index of -0.68 ± 0.10, as is expected in the IC emission model.

In all of the above cases, the available radio data used did not allow evaluation of the spectral index for each of the Fornax A lobes individually and it was assumed that the spectral behaviour of both lobes was the same. Since the errors on the X-ray spectral indices are large, it is conceivable that the lobes have different electron energy indices. For accurate modelling of the broadband SED it is therefore important to determine if the radio spectral index (and therefore the electron energy index) of each of the lobes is indeed similar.

4.4. Multi-wavelength Data

4.4.1. 154 MHz MWA observations and data reduction

The MWA (Lonsdale et al 2009; Tingay et al. 2013; Bowman et al. 2013) is a new low-frequency radio interferometer array that began science operations in 2013 July. It consists of 128 antenna tiles, each containing 16 crossed-dipole antennas above a conducting ground plane. The tiles are pointed electronically using analogue beamformers. The MWA is an official Square Kilometre Array precursor instrument, located at the Murchison Radio Observatory in Western Australia at a latitude of $-26\overset{\circ}{.}7$.

Observations of Fornax A were made with the MWA on 2013 August 21, comprising of seven snapshot observations, each of 112 s duration and using the same beamformer delay settings. The centre frequency was 154.315 MHz and the full 30.72 MHz bandwidth was used in calibration and imaging. The data were converted from their raw format into CASA measurement sets using COTTER, a data conversion pipeline that implements radio-frequency interference (RFI) flagging with AOFLAGGER (Offringa et al. 2010, 2012). An initial set of complex antenna gain solutions was obtained using a single snapshot observation of the bright calibrator source Pictor A (Pic A). The VLA image of Pic A (Perley et al. 1997) at 1.4 GHz was re-scaled to match the flux-density value of Pic A at 154 MHz according to Jacobs et al. (2013b) and multiplied by the MWA primary beam, as calculated analytically for the chosen antenna tile pointing. This model was then used to calibrate the data using the BANDPASS task in CASA.

The initial calibration solutions from Pic A were transferred to one of the Fornax A snapshots and an image was made using WSCLEAN (Offringa et al. 2014). The advantage of WSCLEAN over other packages is the high speed at which we were able to produce large, widefield images in a standard projection, which could then be used for self-calibration. A 7000 by 7000-pixel image was produced for both of the instrumental polarizations and the resulting clean-component model was placed into the model column of the measurement set. For the self-calibration iterations, WSCLEAN was stopped when the first negative component was produced. Self-calibration was then performed in CASA with the BANDPASS task. The uv range for calibration was restricted to exclude baselines shorter than 30 wavelengths, since diffuse emission on these scales is not represented in the calibration model.

Three self-calibration iterations were performed and the final set of calibration solutions was then applied to each of the seven Fornax A snapshots. Both instrumental polarizations were then imaged for each snapshot using wsclean with a pixel size of 0.5 arcmin and an image size of 7000 by 7000 pixels. A value of 100 was used for the number of 'wlayers' (Offringa et al. 2014) and major iterations were used as per the Cotton-Schwab (Schwab 1984) algorithm. The resulting fourteen images were then mosaiced together, using weights for each pixel that were derived from the primary beam shape, which was calculated analytically for each snapshot and each antenna polarization.

Self-calibration is known to affect the flux-density scale of MWA images. To check the flux-density scale, 16 unresolved point sources from the Culgoora (Slee 1977, 1995) catalogue were identified within 10° of the centre of the average primary beam. A scaling factor was calculated from the ratio of the expected flux density at 154 MHz and the measured peak brightness in the MWA mosaic for each source. The mean of these scaling factors was 1.325 and the standard deviation was 19% of the mean. The scaling factor was then applied to the MWA mosaic to produce the final, correctly scaled image. The likely cause for the initial lower-than-expected flux-density scale in the original MWA mosaic is the initial transfer of calibration solutions from a different antenna tile pointing, combined with the effects of self-calibration with an imperfect model. We take the 19% standard deviation of the scaling factors as the uncertainty in the flux-density scale of the image.

The final widefield image, with the Culgoora sources used to set the flux-density scale circled, is shown in Fig. 4.1. Fornax A is clearly visible as the large double source near the centre of the image. The angular resolution is approximately 3 arcmin and the rms is approximately 15 mJy/beam in regions where there are no sources present above the 5-sigma level and more than 1° away from Fornax A. Close to Fornax A the rms is slightly higher due to calibration and deconvolution errors and is approximately 25 mJy/beam. The position of the peak pixel in the core is RA (J2000) $3^{\rm h}22^{\rm m}43^{\rm s}$, Dec (J2000) $-3712'2''$. This is consistent with the position of the host galaxy NGC 1316, given our pixel size of 28.8 arcsecs, which is located at RA (J2000) $3^{\rm h}22^{\rm m}41.718^{\rm s}$, Dec (J2000) $-3712'29.62''$ (Shaya et al. 1996). The peak brightness of the core is 4.24 Jy/beam and the Gaussian restoring beam is 3.08 × 3.08 arcmin. A zoomed in region centred on Fornax A is shown in Fig. 4.2, which clearly shows the structure of the bright lobes and the fainter central core. The peak brightness of the entire source is 19.7 Jy/beam, at a point in the west lobe at RA (J2000) $3^{\rm h}21^{\rm m}17^{\rm s}$, Dec (J2000) $-379'10''$. The extent of the lobes is approximately 72 arcmin in the east-west direction, corresponding to a linear extent of 389 kpc.

To measure flux densities for Fornax A, we first blanked out all pixels with a value less than 0.20 Jy/beam, then selected regions of the image using kvis. We measured the flux

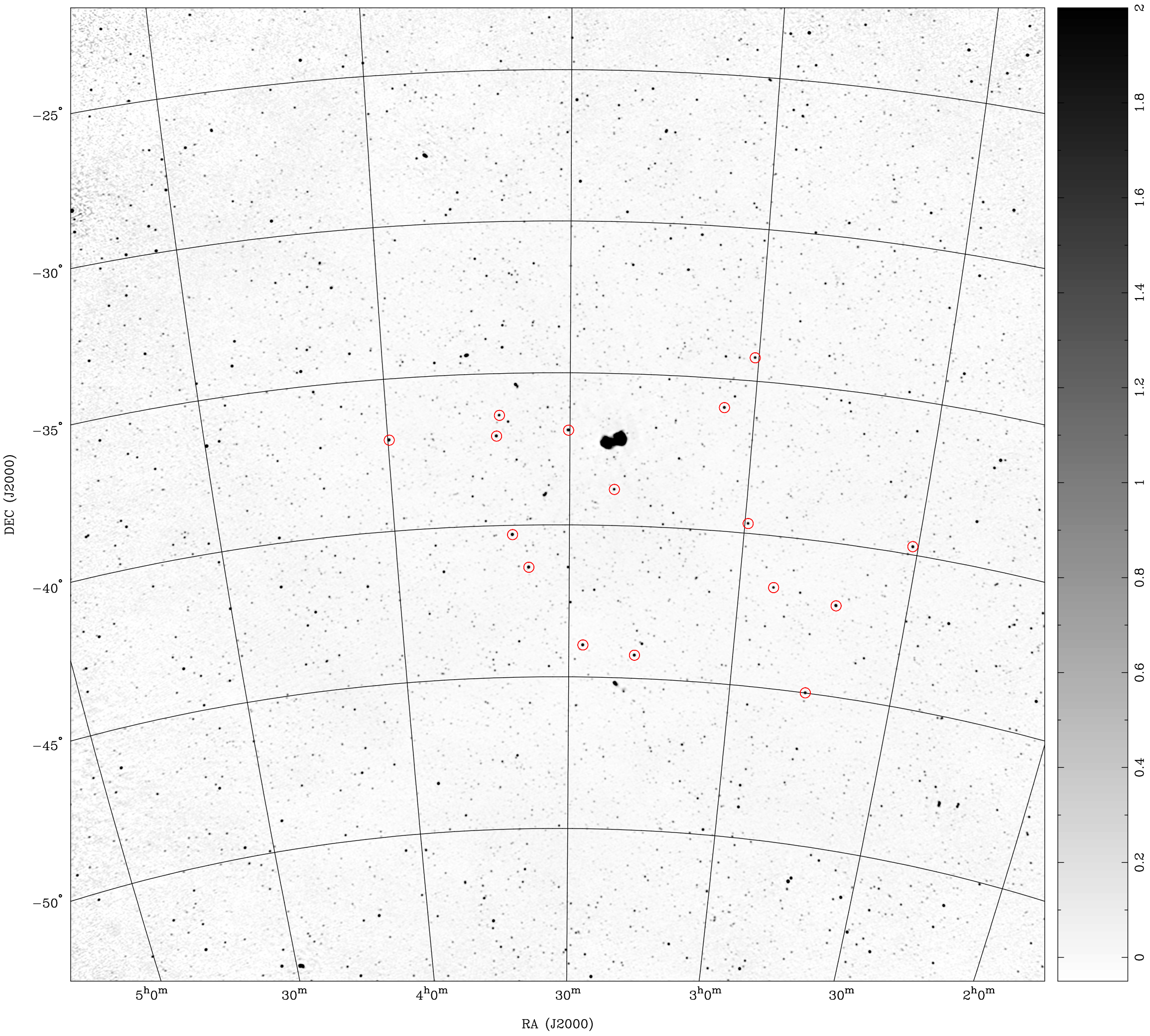

Figure 4.1 Fornax A and surrounding field at 154 MHz with the Murchison Widefield Array. The image is shown on a linear scale between −0.05 and +2 Jy/beam. It has an angular resolution of 185 arcsec and an rms noise of approximately 15 mJy/beam in 'empty' regions of the image more than 1° away from Fornax A. The red circles mark the positions of the Culgoora sources (Slee 1977, 1995) used to set the flux-density scale.

density of the east lobe, defined as the region of the source east of RA (J2000) $3^h23^m0^s$ to be 260 ± 50 Jy. We defined the west lobe as the region to the west of RA (J2000) $3^h23^m0^s$, minus a box surrounding the central core. We measured the flux density of the west lobe to be 480 ± 90 Jy and the core flux density to be 12.0 ± 2.3 Jy. The total source flux density at 154 MHz is 750 ± 140 Jy. The errors are dominated by the 19% flux-density scale uncertainty. Other sources of error, such as imperfect bandpass calibration and deconvolution errors, are estimated to be at the sub-Jy level and their impact on the flux-density measurements of Fornax A are negligible.

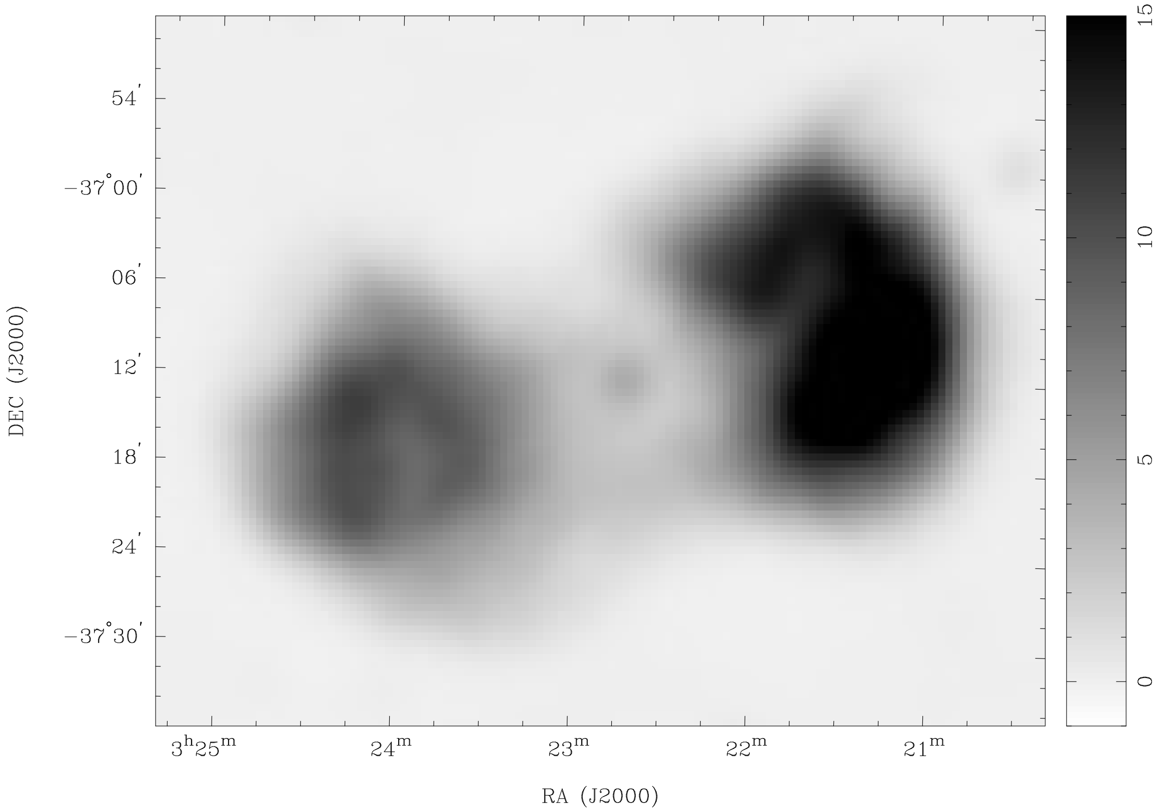

Figure 4.2 As for Fig. 4.1, but zoomed in on Fornax A. The image is shown on a linear scale between −1 and +15 Jy/beam.

4.4.2. Microwave-band data reduction

We obtained flux-density measurements at 70 and 100 GHz for both of the Fornax A lobes by analysing the most recently released *Planck* images (*Planck* Collaboration 2013). In all except the lowest *Planck* observing band we are able to resolve the lobes of Fornax A. To measure the flux density of the lobes at 70 GHz, we first projected a patch of 7.328 square degrees and 128 × 128 pixels, roughly centred on NGC 1316, and blindly searched in that patch using the biparametric adaptive filter (BAF) of López-Caniego & Vielva (2009). At the positions of the peaks found, a centroid search was performed with sub-pixel accuracy to re-estimate the coordinates. Both radio lobes were detected, with a signal-to-noise ratio of 9.5 and 9.1 for the west and east lobes, respectively. The BAF analysis was then repeated using the coordinates from the blind search and a new 7.328 square degree patch centred on each of the lobes. The flux density for each lobe and the noise level in the vicinity of the source were measured, masking other bright spots that could bias the estimation of the noise level, in this case, the other lobe. This process was then repeated with the 100 GHz and 143 GHz data, however, at 143 GHz there was only a 2-σ detection of the lobes and so these data are not included. The measured flux densities and error estimates are in Table 4.1.

The spectral indices of the two radio lobes calculated from the *Planck* flux densities are α_{70}^{100}(west) = −4.0 ± 0.6 and α_{70}^{100}(east) = −3.8 ± 0.6.

Fornax A is identified in the most recent *WMAP* point source catalogue from the 9-year data release (Bennett et al. 2013). In order to take advantage of the full nine years of data and maintain consistency in the technique used to extract the flux-density measurements, we have chosen to re-measure the flux density of Fornax A in the 9-year *WMAP* data, using the BAF algorithm. We use the same method described above for the *Planck* data to measure flux densities for the whole source at 23, 33, 41, 61 MHz. Our results, shown in Table 4.1, are consistent with the values reported in the CMB-free QVW point source catalogue of Bennett et al. (2013).

4.4.3. *Fermi*-LAT data reduction

We selected five years of data (MET 239557417 - MET 401341317) observed by *Fermi*-LAT for regions around Fornax A and used the standard LAT analysis software (v9r32p5)[1]. The photons above 100 MeV were selected for the analysis. The region-of-interest (ROI) was selected to be a 20° × 20° square centred on the position of Fornax A. To reduce the effect of the Earth's albedo background, time intervals when the Earth was appreciably in the field-of-view (FoV)[2] were also excluded from the analysis. The spectral analysis was performed based on the P7REP version of post-launch instrument response functions. Both the front and back-converted photons were selected. The standard likelihood-analysis method, incorporated in the routine GTLIKE, was adopted.

The Galactic and isotropic diffuse models provided by the *Fermi* collaboration[3] were used in the analysis. 2FGL sources (Nolan et al. 2012) were also included and the parameters for point sources within 5° of Fornax A were allowed to vary. The counts image and residual image above 100 MeV are shown in Fig. 4.3. To study the spatial extension of the source, we also introduced disk templates and varied the radius of the disk, but found no improvement in the fitting. Thus, we treat Fornax A as a point source in the spectral analysis. It should be noted that Fornax A is already included in the 2FGL catalogue (Nolan et al. 2012) as a point source (2FGL J0322.4-3717).

---

[1] http://fermi.gsfc.nasa.gov/ssc

[2] That is when the centre of the FoV is more than 52° from zenith, as well as time intervals when parts of the ROI are observed at zenith angles > 100°.

[3] Files: gll_iem_v05.fit and iso_source_v05.txt available at
http://fermi.gsfc.nasa.gov/ssc/data/access/
lat/BackgroundModels.html

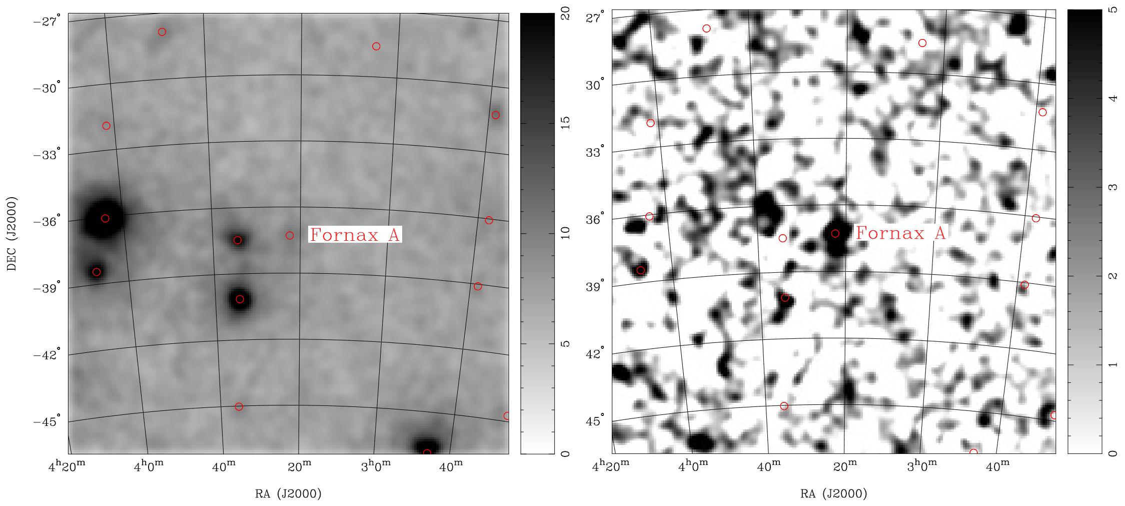

Figure 4.3 γ-ray counts image (left panel) and residual image (right panel) above 100 MeV in the ROI. The sources in the 2FGL catalogue are marked as red circles.

The best-fit position of Fornax A was found to be RA (J2000) $3^{h}22^{m}34^{s}$, Dec (J2000) -37°21′11″, with an error radius of 0.13, which is consistent with the position given in 2FGL catalogue of RA (J2000) $3^{h}22^{m}24^{s}$, Dec (J2000) -37°17′31″. We find that Fornax A has a flux of 6.7×10^{-9} ph cm^{-2} s^{-1} and a photon index of 2.2 ± 0.1 above 100 MeV (photon index, Γ, defined as $dN/dE \propto E^{-\Gamma}$, where N is the number of photons and E is energy). The test statistic value of the source was 64 in the same energy range, corresponding to a significance of about 8σ. These values are consistent with the values for Fornax A reported by Nolan et al. (2012) of 0.5×10^{-9} ph cm^{-2} s^{-1} above 1000 MeV.

To obtain the SED of Fornax A above 100 MeV, we divided the energy range into logarithmically spaced bands and applied gtlike in each band. Only the energy bins for which a signal was detected with a significance of at least 2σ were considered. The derived high-energy SED is shown in Fig. 4.4. The γ-ray flux is approximately constant from 200 to 3000 MeV, but drops significantly in the highest energy bin.

4.4.4. Previously published data

We have conducted a thorough search of the literature and compiled a comprehensive list of flux-density measurements of Fornax A across a wide frequency range. These are summarised in Table 4.1. The listed flux-density measurements are for the whole source, since there are only a few published flux-density measurements of the individual lobes. Where the measurements are resolved, we report the sum of the two lobes and where the core is also measured, we include this in the sum, as it is included in all of the unresolved

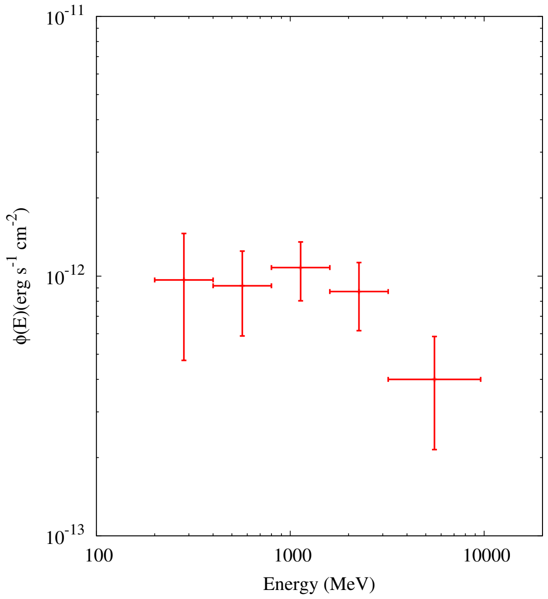

Figure 4.4 The SED of Fornax A above 100 MeV derived from *Fermi*-LAT observations.

measurements. The inclusion of the core is a source of error, however, it is not considered to affect the results of our modelling significantly. At 154 MHz the core represents less than 2% of the total flux density and at 1415 MHz the contribution of the core is less than 0.2%. We show in Section 4.1.1 that the core has a steeper spectrum than the lobes so its contribution above 1415 MHz is negligible. In Table 4.1 we list both the frequency, ν, in MHz, and the equivalent energy, $h\nu$, in MeV. We also show the flux density, S_ν, in Jy and convert this to a flux, ϕ, in erg cm^{-2} s^{-1}. For all measurements below 1 MeV the flux is calculated as $\phi = \nu S_\nu$, and for the γ-ray data we take into account the large logarithmically-spaced energy bin sizes (E), by using $\phi = (h\nu)^2 \mathrm{d}N/\mathrm{d}E$, where N is the photon count in cm^{-2} s^{-1}. Notes on the published data points are given in this section.

Low-frequency data: 4.7−843 MHz

Many of the observations of Fornax A below 1 GHz come from the very early days of radio astronomy, when the first radio interferometers were being built and used to discover discrete radio sources in the sky for the first time. Many of these observations had poor angular resolution by today's standards and large flux-scale uncertainties. However, they are sufficient to constrain SED models of Fornax A over the large energy ranges that are being considered in this paper. The flux-density measurements of Fornax A, their estimated uncertainties, and references for each measurement are given in Table 4.1. Not all references explicitly state the estimated uncertainties in their measurements, so we have used the estimate of a 20% error in the overall flux-density scale in the Shain (1958) measurements as

Table 4.1 Fornax A SED Data.

ν (MHz)	$h\nu$ (MeV)	S_ν (Jy)	ϕ (erg s^{-1} cm^{-2})	Uncertainty	Reference
4.7*	1.94E-14	13500	6.34E-13	20%	Ellis & Hamilton (1966)
18.3	7.57E-14	3500	6.40E-13	20%	Shain & Higgins (1954)
19.7	8.15E-14	4300	8.47E-13	20%	Shain (1958)
29.9	1.24E-13	2120	6.34E-13	10%	Finlay & Jones (1973)
85.7	3.54E-13	950	8.14E-13	20%	Mills et al. (1960)
100*	4.14E-13	200,240	2.40E-13	20%	Stanley & Slee (1950); Bolton et al. (1954)
154	6.37E-13	750.4	1.16E-12	19%	This work
189*	7.82E-13	519	9.81E-13	5%	Bernardi et al. (2013)
400*	1.65E-12	140	5.60E-13	10%	McGee et al. (1955)
408	1.69E-12	259	1.06E-12	10%	Robertson (1973); Cameron (1971)
600	2.48E-12	310	1.86E-12	25%	Piddington & Trent (1956)
843	3.49E-12	169	1.42E-12	9%	Jones & McAdam (1992)
1415	5.85E-12	125	1.77E-12	8%	Ekers et al. (1983)
1510	6.24E-12	117	1.77E-12	10%	Fomalont et al. (1989)
2700	1.11E-11	98.0	2.65E-12	10%	Shimmins (1971)
5000	2.07E-11	54.7	2.74E-12	15%	Gardner & Whiteoak (1971)
23000	9.51E-11	9.21	2.12E-12	2%	This work
33000	1.36E-10	4.84	1.60E-12	4%	This work
41000	1.70E-10	2.43	9.96E-13	6%	This work
61000	2.52E-10	1.49	9.09E-13	22%	This work
70000	2.89E-10	2.637	1.85E-12	10%	This work
100000	4.14E-10	0.660	6.60E-13	21%	This work
2.4E+11	1.00E-03	2.06E-7	4.98E-13	20%	Tashiro et al. (2009); Isobe et al. (2006)
6.8E+16	2.83E+02	1.4E-12	9.68E-13	51%	This work
1.4E+17	5.66E+02	6.7E-13	9.19E-13	36%	This work
2.7E+17	1.13E+03	3.9E-13	1.08E-12	26%	This work
5.5E+17	2.26E+03	1.6E-13	8.73E-13	29%	This work
1.3E+18	5.54E+03	3.0E-14	4.01E-13	46%	This work

*These data have not been included in the SED fitting in Section 4.2 for reasons detailed in the text.

a guide when estimating errors in flux densities reported in this early era of radio astronomy. We consider that the flux-density measurements at 100 MHz (Stanley & Slee 1950; Bolton et al. 1954) and the measurement at 400 MHz (McGee et al. 1955) are unreliable, due to probable systematic errors in the overall flux-scale calibration, and we do not include them in our SED fitting in Section 4.2.

GHz-frequency data: 1.4−5 GHz

We use the flux-density measurements of the lobes and core of Fornax A from Ekers et al. (1983) at 1415 MHz. The observations use data from the Fleurs Synthesis Telescope, combined with 1.4 GHz data from the Parkes radio telescope to fill in the central part of the uv plane.

We measure the flux densities of the lobes and the unresolved core of Fornax A at 1.5 GHz using the 14-arcsec resolution image of Fomalont et al. (1989). Details of the observations used by Fomalont et al. (1989) are not given in their paper, however, the reasonably good agreement between the flux densities we measure in the Fomalont et al. (1989) image at 1510 MHz and those reported by Ekers et al. (1983) indicates that, despite its high angular resolution, the 1.5 GHz image is not missing significant emission on the angular scales of the lobes and therefore our flux-density measurements are reliable.

We obtained flux-density measurements for the west and east lobes of Fornax A from the Parkes 2700 MHz survey (Shimmins 1971).

We measured the flux density at 5 GHz for both of Fornax A's lobes from the Parkes image of Gardner & Whiteoak (1971). A software planimeter[4] was used to compute the area enclosed by each contour and the flux density was calculated from this area and the brightness temperature indicated by the contour. A background contribution of 0.78 K across the source was subtracted from the integrated flux density. We measured flux densities of 31.5 ± 4.7 Jy and 23.2 ± 3.4 Jy for the west and east lobes respectively, giving a total source flux density of 54.7 ± 8.2 Jy, which is consistent with the value of 49 Jy reported by Kühr et al (1981), who do not report separate values for each of the lobes or provide an image.

X-ray data

We use the X-ray flux densities reported by Tashiro et al. (2009) and Isobe et al. (2006) for the west and east lobes, respectively, at 1 keV. Here we assume that the reported flux densities represent the lobe emission with negligible contribution from thermal emission. We expect this to be a valid assumption since Tashiro et al. (2009) model and remove the thermal emission, and while Isobe et al. (2006) do not account for thermal emission, their data is very well fit by a power-law model at > 3 keV, where the thermal emission should be negligible, given their best-fit temperature of less than 1 keV.

---

[4] http://www.csudh.edu/math/sraianu/

4.5. Spectral Energy Distribution Analysis

4.5.1. Spectral index between 154 MHz and 1.5 GHz

Since we have images at 154 MHz and 1.5 GHz with reasonable angular resolution, we investigate the spectral index between these two frequencies in detail. Fig. 4.5 shows Fornax A at 154 MHz (gray scale and red contours) overlaid with the VLA 1.5 GHz image of Fomalont et al. (1989), which has been smoothed to the MWA resolution of approximately 3 arcmin. The morphologies at both frequencies match closely for the lobes, however the compact core is much more prominent at 154 MHz than at 1510 MHz.

We expect from the previous IC modelling of Tashiro et al. (2009) and Isobe et al. (2006) that there is little curvature in the spectrum between these two frequencies and the relatively large fractional frequency coverage allows us to accurately measure the spectral index. The spatial distribution of the spectral index across the source is of interest as it provides clues about the evolutionary history and the physical properties of the radio galaxy. At the 3-arcmin angular resolution of Fig. 4.5, the close match between the MWA and VLA contours indicates that there is little spatial variation in the spectral index across the lobes. At this resolution, however, we are unable to resolve the filamentary structure of the lobes shown by Fomalont et al. (1989). We investigate the spatial variation of the spectral index at the MWA resolution further, using spectral tomography and temperature−temperature (T-T) plots (Turtle et al. 1962), in Sections 4.1.1 and 4.1.2, respectively.

Spectral tomography

We use the technique of spectral tomography to investigate the spatial variation of the spectral index over the source. This technique is useful for identifying regions of different spectral indices in complex structures, such as the lobes of radio galaxies, where there may be distinct structures that overlap in our line-of-sight that are difficult to identify using traditional spectral-index maps (see e.g. Katz-Stone & Rudnick 1997; Gizani & Leahy 2003;

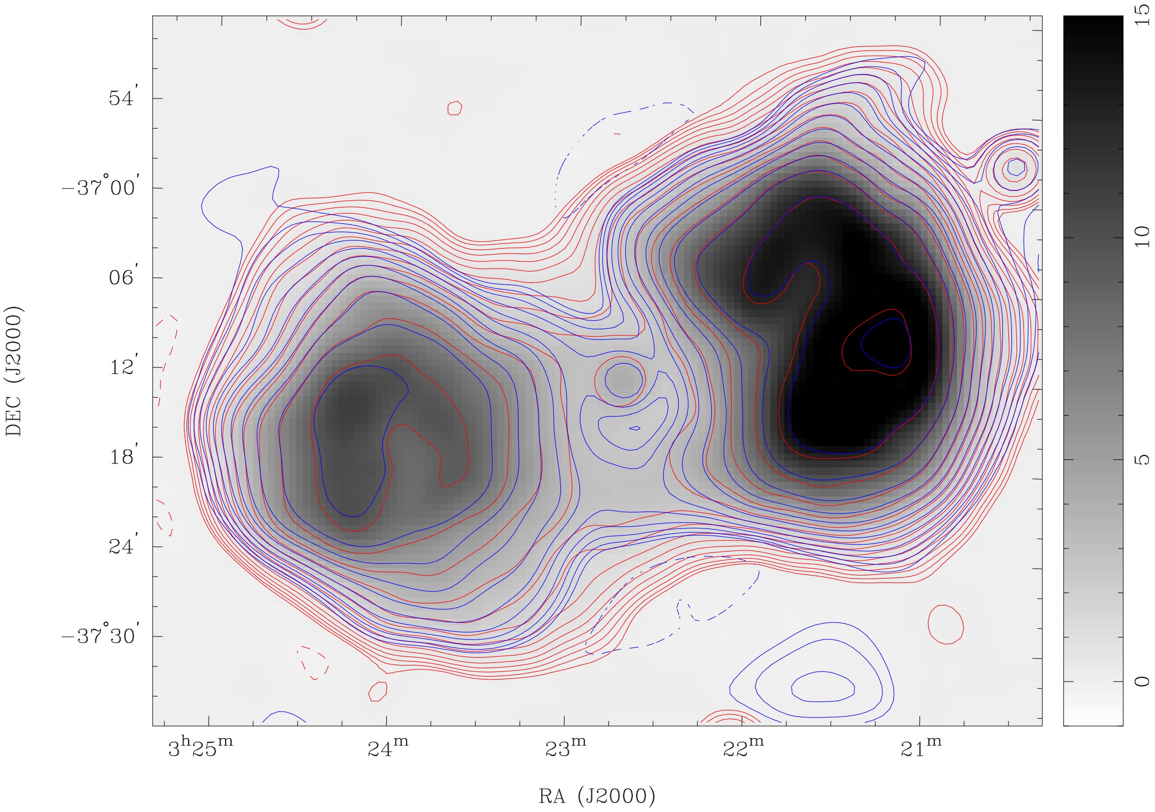

Figure 4.5 Fornax A at 154 MHz (gray scale and red contours) overlaid with the VLA 1.5 GHz (Fomalont et al. 1989) contours, after smoothing to the MWA resolution, in blue. Positive contours are solid and increment in a geometric progression of $\sqrt{2}$, starting at 0.1 Jy/beam for the 154 MHz image and 0.05 Jy/beam for the 1.5 GHz image. The broken red contour is at -0.1 Jy/beam and the broken blue contour is at -0.05 Jy/beam.

Gaensler & Wallace 2003; McKinley et al. 2013b). We constructed a tomography cube using our 154 MHz image and the 1.5 GHz VLA image (Fomalont et al. 1989), following the procedure described by McKinley et al. (2013b). Fig. 4.6 shows six slices from the spectral tomography cube, with trial spectral indices, α_t, as indicated in the top-left corner of each panel. The top three panels of Fig. 4.6 show the lobes as completely over-subtracted in the top-left panel and completely under-subtracted in the top-right panel. We therefore estimate that the spectral index of both lobes lies between −0.72 and −0.82 (i.e. $\alpha_r = -0.77 \pm 0.05_{stat}$, where the quoted error is the statistical error only, since the systematic errors are not relevant for comparing relative spectral indices across the source). The core region, labelled with an arrow in the bottom-centre and bottom-left panels of Fig. 4.6, has a significantly steeper spectrum than the lobes, which we estimate at $\alpha_{core} = -0.95 \pm 0.05_{stat}$.

We find no strong evidence for overlapping structures with different spectral indices in the lobes. The low-level ripple structure present in the lobes in the top panels of Fig. 4.6 is thought to be due to minor deconvolution errors associated with using delta functions to represent diffuse structure. This could possibly be overcome by using alternative techniques

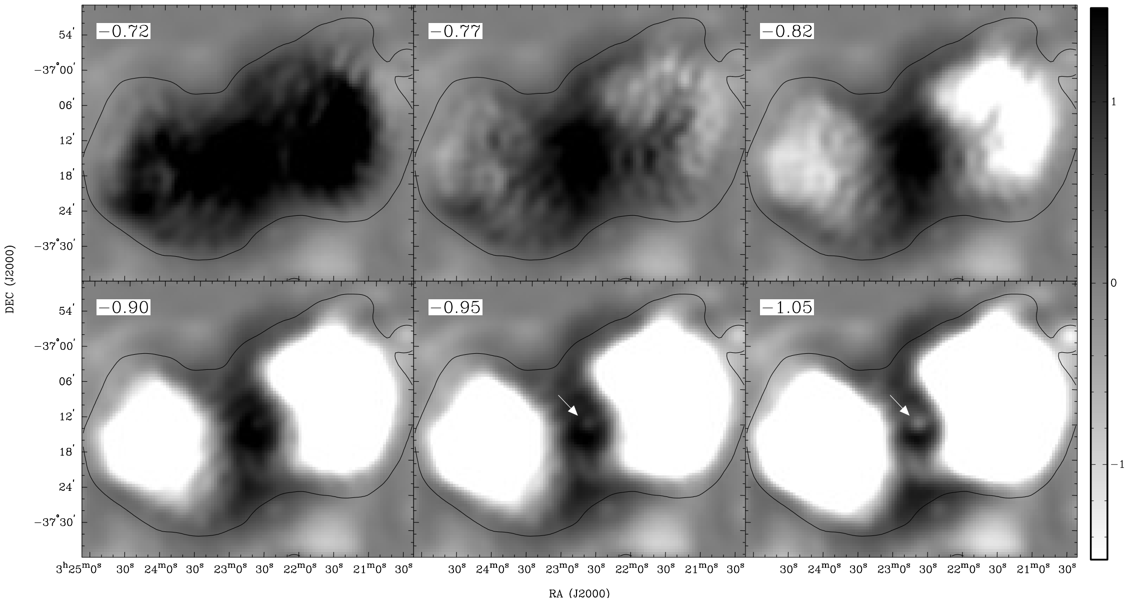

Figure 4.6 Slices from the spectral tomography cube, with trial spectral indices indicated in the top left corner of each panel panel. The white arrow shows the position of the compact core which has a steeper spectrum than the lobes. The gray scale is linear and from -1.5 to 1.5 Jy/beam.

such as multi-scale clean or maximum entropy method deconvolution, however we leave experimentation with these algorithms for future work, since the errors do not impact on the main scientific results of this paper. We use the rms in a region covering approximately one quarter of each lobe to estimate these deconvolution errors and use these errors in the T-T plot analysis in Section 4.1.2.

T-T Plots

T-T plots for the east and west lobes of Fornax A are shown in Fig. 4.7. Here we have plotted the flux densities at each pixel in the 154 MHz and 1510 MHz images against each other and computed a line of best fit to the data points. We compute the spatially-averaged spectral index, α, for each lobe and the χ^2 per degree of freedom (χ^2_{red}) of the fits, following the same procedure as McKinley et al. (2013b). We find $\alpha_{east} = -0.77 \pm 0.01(\mathrm{stat})^{+0.09_{\mathrm{sys}}}_{-0.08_{\mathrm{sys}}}$, and $\alpha_{west} = -0.76 \pm 0.01(\mathrm{stat})^{+0.09_{\mathrm{sys}}}_{-0.08_{\mathrm{sys}}}$. Here we have quoted the statistical errors, due to the scatter of the individual data points, and the systematic errors, due to the uncertainty in the flux-density scale, separately to show that the two lobes have the same spectral index to within an error of $\Delta\alpha_r = 0.01$ (since systematic errors affect both lobes equally). This is consistent with the spectral tomography results of Section 4.1.1. The greater-than-unity χ^2_{red} values of 4.2 and 3.1 for the east and west lobes, respectively, are probably due to the same deconvolution errors that give rise to the ripple structures present in the top panels of Fig.

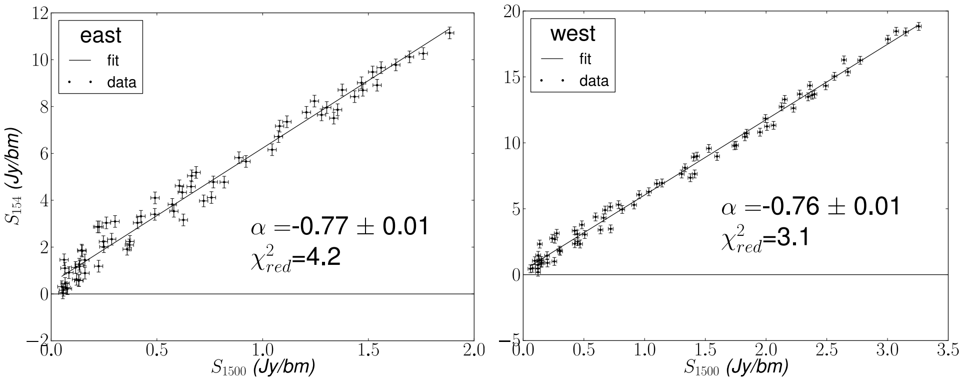

Figure 4.7 T-T plots for east (left panel) and west (right panel) lobes of Fornax A.

4.6.

4.5.2. SED Fitting

The *Fermi*-LAT observations have insufficient angular resolution to resolve the two Fornax A lobes, however, we have shown in our analysis of the radio spectrum that the spectral behaviour of both lobes is very similar; the low-frequency spectral indices for the west and east lobes between 154 and 1510 MHz are α_{154}^{1510}(west) = −0.76 ± 0.01(stat) and α_{154}^{1510}(east) = −0.77 ± 0.01(stat), respectively. Additionally, the spectral index at microwave frequencies between 70 and 100 GHz (the part of the synchrotron spectrum expected to correspond to any IC γ-ray emission) is also the same for both lobes within the (relatively large) errors of our *Planck* measurements (α_{70}^{100}(west) = −4.0 ± 0.6 and α_{70}^{100}(east) = −3.8 ± 0.6). As such, we proceed with the IC modelling using the flux densities of the whole source listed in Table 4.1.

As noted in Section 3.5.1, we have excluded the points at 100 and 400 MHz in the SED fitting, due to probable systematic errors in these measurements. We have also excluded the point at 4.7 MHz as we found that the data below 5 GHz is fit well by a single power-law spectrum, but the 4.7 MHz point sits well above the expected flux density from this power-law model, which is difficult to physically explain and is more likely to be due to incorrect calibration of the overall flux-density scale, or other problems that are inherent in such very low-frequency observations.

To investigate the origin of the high energy emission in the Fornax A lobes, we compare three models (I, II, III) for the broadband SED. In all three models we include both the CMB and the EBL (using the model of Franceschini et al. 2008) as the seed photon sources for the IC scattering component. The best-fit model parameters are calculated by numerical minimization with PYMINUIT. The derived model parameters and the χ^2 per degree of freedom for each fit are shown in Table 4.2.

Model I is a purely leptonic scenario, where we assume that both the X-rays and γ-rays are due to IC scattering of the seed photons by the synchrotron-emitting population of electrons, which have a distribution described by $N_e(E) = K(E/1\text{GeV})^p e^{-(E/E_{ce})}$, where K is a normalisation constant, E is energy, p is the electron energy index and E_{ce} is the high cutoff energy. The modelling results are shown in Fig. 4.8. In this scenario, the IC scattering of the EBL accounts for the γ-ray emission well, but the IC scattering of the CMB results in an X-ray flux that is an order of magnitude more than the observed value at 1 keV.

In Model II, we attempt to modify the electron energy distribution in order to fit the X-ray data point. As for Model I, we assume a purely leptonic scenario, but we introduce a low-energy cutoff in the electron energy distribution, such that $N_e(E) = 0$ for $E < 1\text{GeV}$. While it is possible that a low-energy cutoff exists, this is not motivated by any actual observational evidence. The modelling results are shown in Fig. 4.9. In this case the model fits the X-ray and γ-ray data points, but the X-ray spectral index at 1 keV is approximately zero, which is much harder than the observed values of $0.62^{+0.24}_{-0.15}$ (Isobe et al. 2006) and 0.81 ± 0.22 (Tashiro et al. 2009) for the east and west lobes, respectively.

Model III assumes that the radio and X-ray flux from the radio lobes result from synchrotron and IC scattering, respectively, while p-p collisions with pion decay account for the γ-rays. The electron energy distribution is as for Model I and the proton energy distribution is also described by a simple power law, $N_p(E) = C(E/1\text{GeV})^r e^{-(E/E_{cp})}$, where C is a normalisation constant, E is energy, r is the proton energy index and E_{cp} is the high cutoff energy. As shown in Fig. 4.10, Model III fits all the data points and predicts the observed X-ray spectrum. However, when we calculate the total energy budget of protons, assuming a thermal proton density in the lobes of $3 \times 10^{-4}\ \text{cm}^{-3}$ (Seta et al. 2013), we obtain a value of 4.6×10^{60} erg, which is two orders of magnitude larger than the thermal emission of the lobes (Seta et al. 2013). This conclusion may be avoided if the emission is localised to relatively denser substructures within the lobes; we explore this scenario briefly in Section 5.

The χ^2 per degree of freedom values, as listed in Table 4.2, are all much greater than unity. The large values are due mainly to the radio and microwave data having small estimated errors, despite their relatively large scatter above and below the smooth models. The χ^2 per degree of freedom of Model I is almost twice that of the other two models, and Model II is ruled out based on the incorrect X-ray spectrum. Hence, the model that best fits the data is

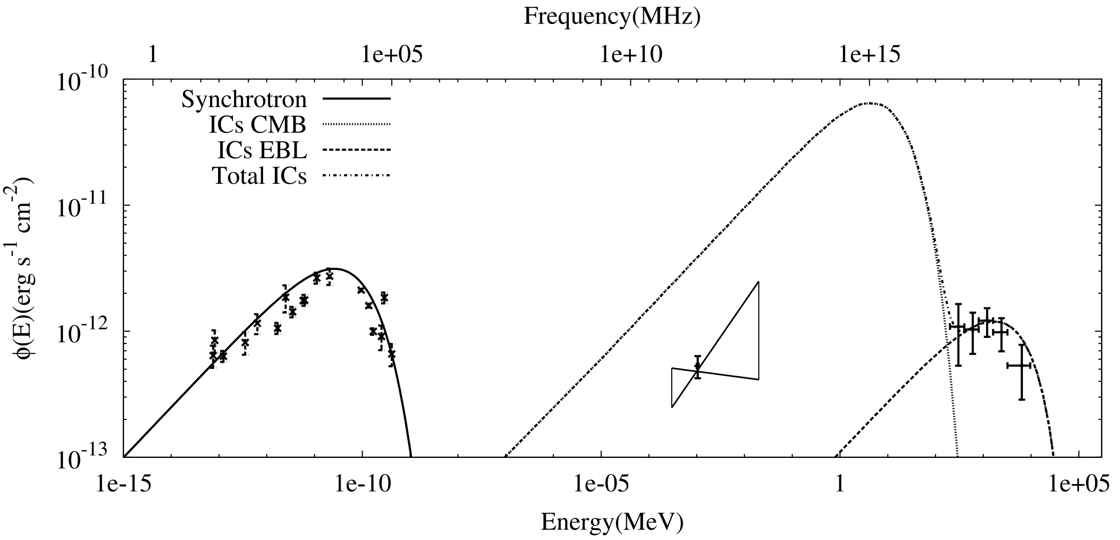

Figure 4.8 The broadband SED of Fornax A for Model I, where both the X-rays and γ-rays are produced by IC scattering by the synchrotron-emitting electrons. The IC scattering contribution from the EBL and the CMB photon fields are both shown in the figure. The model parameters are described in Table 4.2.

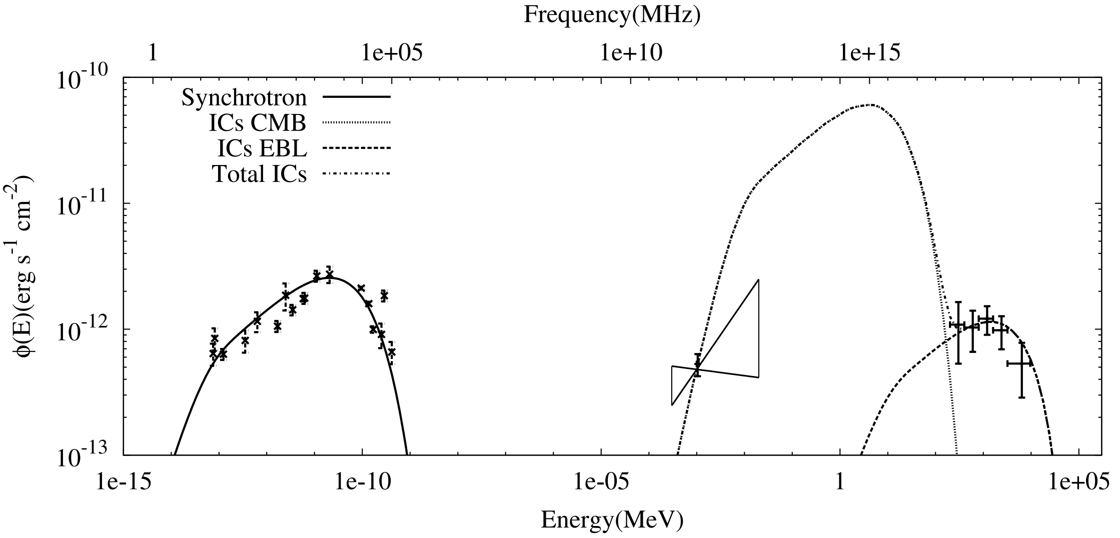

Figure 4.9 The broadband SED of Fornax A for Model II, where both the X-rays and γ-rays are produced by IC scattering by the synchrotron-emitting electrons, which are described by an electron energy distribution with a low-energy cut-off. The model parameters are described in Table 4.2.

Model III.

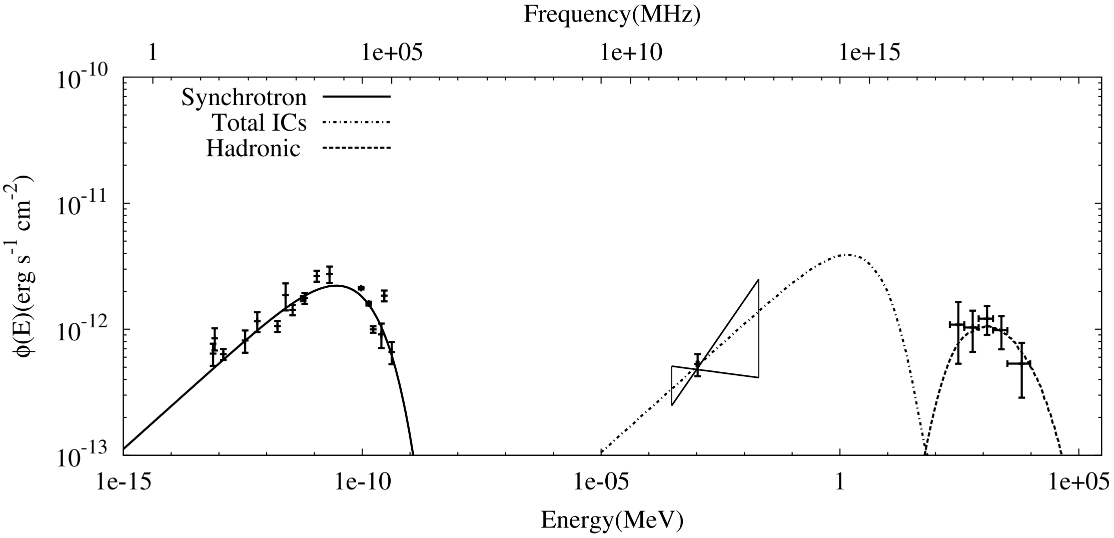

Figure 4.10 The broadband SED of Fornax A for Model III, where the X-ray emission is the result of IC scattering by the synchrotron-emitting electrons and the γ-rays are produce by p-p collisions with pion decay. The model parameters are described in Table 4.2.

Table 4.2 Summary of Fornax A SED best-fit model parameters

Model components	Model I	Model II	Model III
Magnetic field strength (μG)	0.7 ± 0.1	0.7 ± 0.1	2.6 ± 0.3
Electron energy index	−2.2 ± 0.1	−2.3 ± 0.1	−2.3 ± 0.1
Electron high energy cutoff (GeV)	50 ± 4	50 ± 4	45 ± 5
Electron low energy cutoff (GeV)	N/A	1 (fixed)	N/A
Electron normalization ($\times10^{-9}$)	0.4 ± 0.1	0.5 ± 0.1	0.05 ± 0.01
Proton energy index	N/A	N/A	−2.0 ± 0.3
Proton high energy cutoff (GeV)	N/A	N/A	120 ± 30
χ^2/d.o.f.	234/20	131/20	126/17

4.6. Discussion

Our analysis of the low-frequency radio spectrum of the Fornax A lobes confirms that the assumption implicit in the work of Kaneda et al. (1995), Isobe et al. (2006) and Tashiro et al. (2009), that both lobes' spectra can be described by the same power-law, is a valid one. Since systematic errors such as the error in the flux-scale affect both lobes equally, our T-T plots show that the average spectral index of both radio lobes is the same to within an error of $\Delta\alpha_r = 0.01$. We also see little variation in the spectral index across the lobes at the MWA angular resolution of 3 arcmin.

Taking into account systematic errors, our results of $\alpha_{\mathrm{east}} = -0.77 \pm 0.01(\mathrm{stat})^{+0.09_{\mathrm{sys}}}_{-0.08_{\mathrm{sys}}}$, and

$\alpha_{\rm west} = -0.76 \pm 0.01({\rm stat})^{+0.09_{\rm sys}}_{-0.08_{\rm sys}}$ are consistent with the radio spectral index of $\alpha_r = -0.68$ used by Isobe et al. (2006) and Tashiro et al. (2009) to model the X-ray IC emission. Our flux-density measurements and spectral indices are also consistent with the MWA 32-tile results of Bernardi et al. (2013) at 189 MHz.

When we attempt to model the radio, microwave, X-ray and γ-ray data, under the assumption that the same population of synchrotron-emitting electrons is producing the X-ray and γ-ray emission via IC scattering of CMB and EBL photons, we are unable to find an acceptable fit. Our Model I over-predicts the observed X-ray flux by an order of magnitude and our Model II produces an X-ray spectrum that is much harder than the observed values. We therefore reject the hypothesis that both the X-ray and γ-ray emission in the Fornax A lobes are purely the result of IC scattering.

The SED data points are fit well by our Model III, in which the γ-ray emission is produced by p-p collisions with pion decay. However, the total energy budget of the protons in this model is two orders of magnitude larger than the thermal energy suggested by Seta et al. (2013), which is physically unrealistic. The excess energy problem may be overcome, however, if the p-p collisions are taking place primarily in the filamentary structures of the lobes identified at 1.4 GHz by Fomalont et al. (1989). This idea has been proposed as an explanation for the γ-ray emission observed in the so-called *Fermi* bubbles of our own Galaxy by Crocker & Aharonian (2011) and Crocker et al. (2013). Adiabatic compression of the target gas and magnetic fields into filaments, as suggested by Crocker et al. (2013), could produce the observed γ-rays with a total proton energy that is similar to, or less than, the observed thermal energy reported by Seta et al. (2013), if the filling factor is small. In this scenario, the concentrated magnetic fields in the filaments compensate for the small filling factor in order to produce the observed synchrotron emission. In reality, a combination of IC scattering and p-p collisions both inside and outside of the lobe filaments is probably responsible for the total high-energy emission in Fornax A. Incorporating this into a fully time-dependent, self-consistent model of the lobes is, however, left for future work.

Fornax A was identified by Georganopoulos et al. (2008) as an ideal target for *measuring* the EBL, under the assumption that the γ-ray emission detected by *Fermi*-LAT was produced by IC scattering. However, since we have the observational constraints on the EBL from Franceschini et al. (2008), and we have identified that processes other than IC scattering may be responsible for the γ-rays, we have not pursued this measurement.

The position of the γ-ray source that we associate with Fornax A is consistent with the position of the host galaxy NGC 1316, so we cannot rule out the possibility that the γ-ray emission is originating in the host galaxy rather than the lobes. However, we consider this unlikely as the core is much weaker than the lobes at both radio (Ekers et al. 1983; Fomalont et al. 1989, this work) and X-ray (Iyomoto et al. 1998) wavelengths. Iyomoto et al. (1998) interpret the weaker core as evidence that the AGN is currently in a state of declined activity. Our spectral-tomography results indicate that the core region has a steeper spectral index than the lobes, with a value of $-0.95 \pm 0.05_{stat}$, compared to the lobes with a spectral index of $-0.77 \pm 0.05_{stat}$. This could indicate an older spectral age for the core, due to the period of declined activity, but could also be related to different emission processes and optical depths in the core and in the lobes. A lack of AGN activity does not necessarily preclude a γ-ray detection, as γ-ray emission has been confirmed from a number of 'normal' galaxies including the Large and Small Magellanic Clouds, M31 and a number of known starburst galaxies (Nolan et al. 2012; Abdo et al. 2010b). However, since NGC 1316 is neither extremely close-by nor undergoing intense star formation, we consider it unlikely that the host galaxy is producing the detected γ-rays.

4.7. Conclusion

We have presented new low-frequency observations of Fornax A at 154 MHz from the MWA and used these data, along with previously published data at 1510 MHz, to conduct a spatially resolved study of the spectral index of the Fornax A radio lobes. We have also presented microwave flux densities obtained from *Planck* and *WMAP* data and γ-ray flux densities from *Fermi*-LAT data and used these, in combination with previously published flux-density measurements at radio and X-ray energies, to model the spectral energy density of Fornax A. Our results best support a scenario where the X-ray photons are produced by inverse-Compton scattering of the cosmic microwave background and extragalactic background light by the radio-synchrotron emitting electrons in the lobes, while the γ-rays are the result of proton-proton collisions localised in the lobe filaments.

CHAPTER 5

Conclusion

The work that has culminated in this PhD ‘thesis by publication’ has helped to lay the foundations for future scientific work with the Murchison Widefield Array (MWA) and shown that the instrument is capable of producing world-class science. I have presented three papers that make use of MWA test observations to analyse the low-frequency properties of well-known objects; the Moon, Centaurus A and Fornax A. The spectral properties of the two radio galaxies have been examined by comparing the low-frequency images with higher frequency images. In the case of Fornax A, the spectral energy distribution from low-frequency radio to γ-rays was modelled, to investigate the physical processes responsible for the high-energy emission.

Observations of the Moon with the MWA 32-tile prototype were used to assess the suitability of the Moon as a reference source for detection of the redshifted 21-cm signal from the epoch of reionization (EoR). The Moon’s spectrum was found to be corrupted by reflected emission from Earth, particularly in the FM radio band between 87.5 and 110 MHz, presenting an additional challenge for any experiment aiming to use the Moon to detect the EoR signal. The flux density of the Moon was also used to estimate the Earth’s radio leakage in the FM radio band. It was found that this signal from Earth would be difficult to detect by any extraterrestrial civilisation, even using far superior technology to our own.

MWA 32-tile observations of Centaurus A revealed the morphology of the radio lobes at low frequencies and provided tentative evidence for the existence of a southern counterpart to the well-known northern middle lobe. The spectrum of the Centaurus A lobes between 118 MHz and 1.4 GHz was analysed using spectral tomography and temperature-temperature plots.

A complex spatial distribution of spectral index was found, supporting a theory of multiple outbursts from the active galactic nucleus.

Finally, observations of Fornax A with the complete 128-tile MWA were used to confirm that both of the radio lobes have the same spectral index between 154 MHz and 1.5 GHz. The MWA data were then used in conjunction with new flux-density measurements made from *Planck*, *WMAP* and *Fermi*-LAT data, and archival flux-density measurements, to model the spectral energy distribution of the lobes. It was found that the observed high-energy emission is unlikely to be the result of inverse-Compton scattering alone. The observed γ-rays are more likely to be the result of proton-proton collisions, confined primarily to the denser filamentary structures in the lobes.

The scientific work of this PhD is only a prelude to the exciting new science that is just around the corner for the MWA, which is now in full scientific operation. Observing programs for EoR detection, time-domain science and solar studies are now either well underway or complete, and data reduction and analysis are in full swing. Survey science is also proving to be a major strength for the MWA, with its widefield capabilities and sensitivity to diffuse emission making it an ideal instrument for Galactic and extragalactic science.

An example of the visually-stunning images that are now being routinely produced by the MWA team is shown in Fig. 5.1. The image is a 60-snapshot mosaic of the Galactic plane at 150 MHz, made during science commissioning. The entire declination strip along DEC −55 deg was observed over the course of just one night, using a drift-scan mode of operation. The Galactic and extragalactic all-sky MWA (GLEAM) survey will image the entire southern sky in this fashion, at five centre frequencies covering the range between 70 and 230 MHz. This will provide a valuable low-frequency legacy data set, and allow detailed studies of many more fascinating astronomical objects, such as those that have been the subject of this PhD.

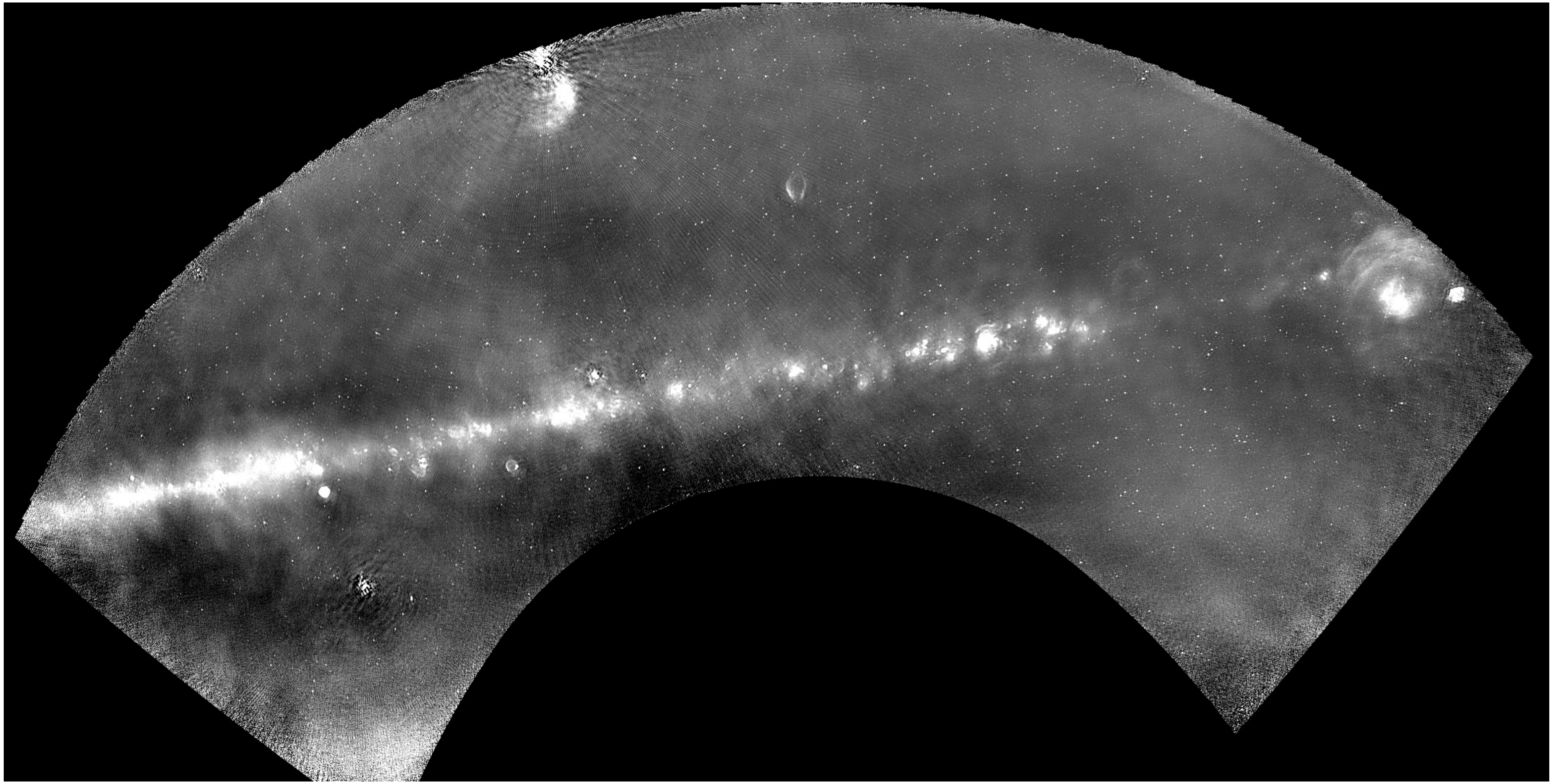

Figure 5.1 A mosaic of 60 snapshot images at 150 MHz, taken over the course of one night with the MWA during science commissioning. The telescope was operated in drift-scan mode, with a fixed pointing at -55 declination along the meridian. The bright object at the top of the image is Centaurus A and the thick band of emission running through the centre of the image is the Galactic plane.

Bibliography

Abdo, A. A., Ackermann, M., Ajello, M., et al., 2010a, Sci, 328, 725

Abdo, A. A., Ackermann, M., Ajello, M., et al., 2010b, ApJS, 188, 405

Atwood, W. B., Abdo, A. A., Ackermann, M., et al., 2009, ApJ, 697, 1071

Australian Communications and Media Authority (ACMA), 2009, Australian Radiofrequency Spectrum Plan 2009 (Melbourne: ACMA), http://www.acma.gov.au

Alvarez, H., Aparici, J., May, J., Olmos, F., 1997, A&AS, 124, 315

Alvarez, H., Aparici, J., May, J., Reich, P., 2000, A&A, 355, 863

Atwood, W. B., Abdo, A. A., Ackermann, M., et al., 2009, ApJ, 697, 1071

Baars, J. W. M., Genzel, R., Pauliny-Toth, I. I. K., et al., 1977, A&A, 61, 99

Baldwin, J. E., 1961, MNRAS, 122, 513

Begelman, M. C., Blandford, R. D., Rees, M. J., 1984, Reviews of Modern Physics, 56, 255

Bennett, C. L., Bay, M., Halpern, M., et al., 2003, ApJ, 583, 1

Bennett, C. L., Halpern, M., Hinshaw, G., et al., 2003, ApJS, 148, 1

Bennett, C. L., Larson, D., Weiland, J. L., et al., 2013, ApJS, 208, 20

Bernardi, G., de Bruyn, A. G., Brentjens, M. A., et al., 2009, A&A, 500, 965

Bernardi, G., Greenhill, L. J., Mitchell, D. A., et al., 2013, ApJ, 771, 105

Boggs, P. T., Rogers, J. E., 1990, Contemporary Mathematics, 112, 186

Bolton, J. G., 1948, Nature, 162, 141

Bolton, J. G., Stanley, G. J., Slee, O. B., 1954, Australian Journal of Physics, 7 110

Bowman, J. D., Cairns, I., Kaplan, D. L., et al, 2013, PASA, 30, 31

Bowman, J. D., Rogers, A. E. E., 2010, Natur, 468, 796

Burns, J. O., 1986, Canadian Journal of Physics, 64, 373

Burns, J. O., Feigelson, E. D., Schreier, E. J., 1983, ApJ, 273, 128

Cameron, M. J., 1971, MNRAS, 152, 439

Clark, B., 1980, A&A, 89, 377

Clarke, D. A., Burns, J. O., Norman, M. L., 1992, ApJ, 395, 444

Clarke, D. A., Burns, J. O., 1991, ApJ, 369, 308

Combi, J. A., Romero, G. E., 1997, A&AS, 121, 11

Cooper, B. F. C.; Price, R. M.; Cole, D. J., 1965, Australian Journal of Physics, 18, 589

Cornwell, T. J., Golap, K. & Bhatnagar, S., 2008, IEEE Journal of Selected Topics in Signal Processing, 2, 647

Crocker, R. M. & Aharonian, F., 2011, PhRvL, 106, 1102

Crocker, R. M., Bicknell, G. V., Carretti, E., et al. 2013, arXiv1312.0692C

DeLaney, T., Koralesky, B., Rudnick, L., Dickel, J. R., 2002, ApJ, 580, 914

de Oliveira-Costa, A., Tegmark, M., & Gaensler, B. M., et al., 2008, MNRAS, 388, 247

Dewdney, P. E., Hall, P. J., Schilizzi, R. T., Lazio, T. J. L. W., 2009, IEEEP, 97, 1482

DeWitt, J. H., Jr., & Stodola, E., K., 1949, PIRE, 37, 229

Ekers, R. D., Goss, W. M., Wellington, K. J., et al., 1983, A&A, 127, 361

Ellis, G. R. A., Hamilton, P. A, 1966, ApJ, 143, 227

Evans, J. V., 1969, ARA&A, 7, 201

Fanaroff, B. L., Riley, J. M., 1974, MNRAS, 167, 31

Feain, I. J., Cornwell, T. J., Ekers, R. D., et al., 2011, ApJ, 740, 17

Feigelson, E. D., Laurent-Muehleisen, S. A., Kollgaard, R. I., Fomalont, E. B., 1995, ApJ, 449, 149

Finlay, E. A., Jones, B. B., 1973, Australian Journal of Physics, 26, 389

Fomalont, E. B., Ebneter, K. A., van Breugel, W. J. M., Ekers, R. D., 1989, ApJ, 346, 17

Franceschini, A., Rodighiero, G. & Vaccari, M., 2008, A&A, 487, 837

Furlanetto, S. R., Oh, S. P., & Briggs, F. H., 2006, PhR, 433, 4-6

Gaensler, B. M., Wallace, B. J., 2003, ApJ, 594, 326

Gardner, F. F. & Whiteoak, J. B., 1971, Australian Journal of Physics, 24, 899

Georganopoulos, M., Sambruna, R. M., Kazanas, D., et al., 2008, ApJ, 686, 5

Gizani, N. A. B., Leahy, J. P., 2003, MNRAS, 342, 399

Giacintucci, S., Venturi, T., Murgia, M., et al., 2007, A&A, 476, 99

Gopal-Krishna, Saripalli, L., 1984, A&A, 141, 61

Gopal-Krishna, Wiita, P. J., 2010, NewA, 15, 96

Greenhill, L. J., & Bernardi, G., 2012, arXiv1201.1700G

Hagfors, T., Green, J. L., & Guillén, A., 1969, AJ, 74, 10

Hamilton, P. A. & Haynes, R. F., 1968, Australian Journal of Physics, 21, 895

Hardcastle, M. J., Cheung, C. C., Feain, I. J., Stawarz, Ł., 2009, MNRAS, 393, 1041

Harris, G. L. H., Rejkuba M., Harris W. E., 2010, PASA, 27, 457

Haslam, C. G., Salter C. J., Stoffel H., Wilson W. E., 1982, A&AS, 47, 1

Haynes, R. F., Cannon, R. D., Ekers, R. D., 1983, PASA, 5, 241

Heiles, C. & Drake F. D., 1963, Icar, 2, 281

Hinshaw, G., Weiland, J. L., Hill, R. S., et al, 2009, ApJS, 180, 225

International Telecommunication Union (ITU), 2001, Transmission Standards for FM Sound Broadcasting at VHF, Recommendation BS.450-3 (Geneva: ITU), http://www.itu.int

Hurley-Walker, N., et al., 2014, submitted

Isobe, N., Makishima, K., Tashiro, M., et al., 2006, ApJ, 645, 256

Israel, F. P., 1998, A&ARv, 8, 237

Iyomoto, N., Makishima, K., Tashiro, M., et al. 1998, ApJ, 503, 31

Jacobs, D. C., Bowman, J., Aguirre, J. E., 2013a, ApJ, 769, 5

Jacobs, D. C., Parsons, A. R., Aguirre, J. E., et al., 2013b, ApJ, 776, 108

Jamrozy, M., Konar, C., Saikia, D. J., Machalski, J., 2009, in ASP Conf. Ser. 36, The Low-Frequency Radio Universe, ed. D. J. Saikia, D. A. Green, Y. Gupta, & T. Venturi (San Francisco, CA: ASP), 137

Jones, Paul A., McAdam, W. B., 1992, ApJS, 80, 137

Junkes, N., Haynes, R. F., Harnett, J. I., Jauncey, D. L., 1993, A&A, 269, 29

Kaneda, H., Tashiro, M., Ikebe, Y., et al., 1995, ApJ. 453, 13

Kassim, N. E., Joseph, T., Lazio, W., et al., 2007, ApJS, 172, 686

Katz, A., & Franco, M., 2011, IMMag, 12, 62

Katz-Stone, D. M., Rudnick, L., 1997, ApJ, 488, 146

Komatsu, E., Smith, K. M., Dunkley, J., et al., 2011, ApJS, 192, 18

Kühr, H., Witzel, A., Pauliny-Toth, I. I. K., & Nauber, U., 1981, A&AS, 45, 367

Landecker, T. L. & Wielebinski, R., 1970, AuJPA, 16, 1

Lantos, P. & Avignon, Y., 1975, A&A, 41, 137

Large, M. I., Mills, B. Y., Little, A. G., et al.,1981, MNRAS, 194, 693

Laurent-Muehleisen, S. A., Feigelson, E. D., Kollgaard, R. I., Fomalont, E. B., 1994, in Schlegel, E. M., Petre, R., eds, American Inst. Phys. Conf. Proc. 313, The Soft X-ray Cosmos, New York, p. 418

Leahy, J. P., Pooley, G. G., Riley, J. M., 1986, MNRAS, 222, 753

Loeb, A. & Zaldarriaga, M., 2007, J. Cosmol. Astropart. Phys., JCAP01(2007)020

Lonsdale, C. J., Cappallo, R. J., Morales, M. F., et al., 2009, IEEEP, 97, 8

López-Caniego, M. & Vielva, P., 2012, MNRAS, 421, 2139

Ma, C., Arias, E. F., Eubanks, T. M., et al., 1998, AJ, 116, 516

Madore, B. F., Freedman, W. L., Silbermann, N., et al., 1999, ApJ, 515, 29

Malin, D. F., Quinn, P. J., Graham, J. A., 1983, ApJ, 272, 5

Mauch, T., Murphy, T., Buttery, H. J., et al., 2003, MNRAS, 342, 1117

McGee, R. X., Slee, O. B., Stanley, G. J., 1955, Australian Journal of Physics, 8, 347

McKinley, B., Briggs, F., Kaplan, D. L., et al., 2013, AJ, 145, 23

McKinley, B., Briggs, F., Gaensler, B. M., et al., 2013b, MNRAS, 436, 1286

McNamara, B. R. & Nulsen, P. E. J., 2007, ARA&A, 45, 117

Mills, B. Y., 1954, Observatory, 74, 248

Mills, B. Y., Slee, O. B., Hill, E. R., 1960, Australian Journal of Physics, 13 676

Morales, M. F., & Wyithe, J. S. B., 2010, ARA&A, 48, 127

Morganti, R., Killeen, N. E. B., Ekers, R. D., Oosterloo, T. A., MNRAS, 307, 750

Nolan, P. L., Abdo, A. A., Ackermann, M., et al., 2012, ApJS, 199, 31

Norman, M. L., Burns, J. O., Sulkanen, M. E., 1988, Nature, 335, 146

Oberoi, D., Matthews, L. D., & Cairns, I. H., 2011, ApJ, 728, 270

Offringa, A. R., de Bruyn, A. G., Biehl, M., et al., 2010, MNRAS, 405, 155

Offringa, A. R., van de Gronde, J. J., Roerdink, J. B. T. M., et al., 2012, A&A, 539, 95

Offringa, A. R., et al., 2014, MNRAS submitted

Ord, S. M., Mitchell, D. A., Wayth, R. B., et al., 2010, PASP, 122, 1353

Osmer, P. S., 1978, ApJ, 226, 79

O'Sullivan, S. P., Feain, I. J., McClure-Griffiths, N. M., et al., 2013, ApJ, 764, 162

Parsons, A. R., Backer, D. C., Foster, G. S., et al., 2010, AJ, 139, 1468

Perley, R. A., Roser, H-J., Meisenheimer, K., 1997, A&A, 328, 12

Perola, G. C., 1981, Fund. Cosm. Phys., 7, 59

Piddington, J. H., Trent, G. H., 1956, Australian Journal of Physics, 9, 74

Planck Collaboration, 2013, A&A submitted, arXiv:1303.5062

Pritchard, J. R., & Loeb, A. 2012, RPPh, 75, 086901

Rampadarath, H., Morgan, J. S., Tingay, S. J., & Trott, C. M., 2012, AJ, 144, 38

Reynolds, J. E. 1994, ATNF Technical Memo Series, 39.3/040

Robertson, J. G., 1973, Australian Journal of Physics, 26, 403

Rogers, A. E. E., & Bowman, J., D., 2008, AJ, 136, 641

Saxton, C. J., Sutherland, R. S., Bicknell, G. V., 2001, ApJ, 563, 103

Schilizzi, R. T., McAdam, W. B., 1975, Royal Astronomical Society Memoirs, 79, 1

Schiminovich, D., van Gorkom, J. H., van der Hulst, J. M., et al., 1994, ApJL, 423, 101

Schoenmakers, A. P., de Bruyn, A. G., Röttgering, H. J. A., et al., 2000, MNRAS, 315, 371

Schreier, E. J., Burns, J. O., Feigelson, E. D., 1981, ApJ, 251, 523

Schwab, F. R., 1984, AJ, 89, 1076

Seta, H., Tashiro, M. S. & Inoue, S., 2013, PASJ, 65, 106

Shain, C. A., 1958, Australian Journal of Physics, 11, 517

Shain, C. A., 1959, IAUS, 9, 328

Shain, C. A. & Higgins, C. S., 1954, Australian Journal of Physics, 7, 130

Shaver, P. A., Windhorst, R. A., Madau, P., & de Bruyn, A. G., 1999, A&A, 345, 380

Shaya, E. J., Dowling, D. M., Currie, D. G., et al., 1996, AJ, 111, 2212

Sheridan, K. V., 1958, Australian Journal of Physics, 11, 400

Shimmins, A. J., 1971, Australian Journal of Physics Supplement, 21, 1

Slee, O. B., 1977, Australian Journal of Physics Astrophysical Supplement, 43, 1

Slee, O. B., 1995, Australian Journal of Physics, 48, 143

Stanley, G. J., Slee, O. B., 1950, Australian Journal of Scientific Research A, 3, 234

Stefan, I. I., Carilli, C. L., Green, D. A., et al., 2013, MNRAS, 432, 1285

Stickel, M., van der Hulst, J. M., van Gorkom, et al., 2004, A&A, 415, 95

Subrahmanyan, R., Saripalli, L., Hunstead, R. W., 1996, MNRAS, 279, 257

Sullivan, W. T., Brown, S., & Wetherill, C., 1978, Sci, 199, 377

Sullivan, W. T., & Knowles, S. H., 1985, in IAU Symp. 112, The Search for Extraterrestrial Life: Recent Developments (Dordrecht: Reidel), 327

Tarter, J. C., 2004, NewAR, 48, 1543

Tashiro, M. S., Isobe, N., Seta, H., et al., 2009, PASJ, 61, 327

Thompson, A. R, Moran, J. M., & Swenson, G. W., Jr., 2001, Interferometry and Synthesis in Radio Astronomy (2nd ed.; New York: Wiley)

Tauber, J. A., Mandolesi, N., Puget, J.-L., et al., 2010, A&A, 520, 1

Tingay, S. J., Goeke, R., Bowman, J. D., et al., 2013, PASA, 30, 7

Turtle, A. J., Pugh, J. F., Kenderdine, S., Pauliny-Toth, I. I. K., 1962, MNRAS, 124, 297

van Haarlem, M. P., Wise, M. W., Gunst, A. W., et al., 2013, A&A, 556, 2

Williams, C. L., Hewitt, J. N., Levine, A. M., et al., 2012, ApJ, 755, 47

Wykes, S., Croston, J. H., Hardcastle, M. J., et al., 2013, A&A, 558, 19

Yang, R. Z., Sahakyan, N., de Ona Wilhelmi, E., et al., 2012, A&A, 542, 19